CHALMERS
UNIVERSITY OF TECHNOLOGY

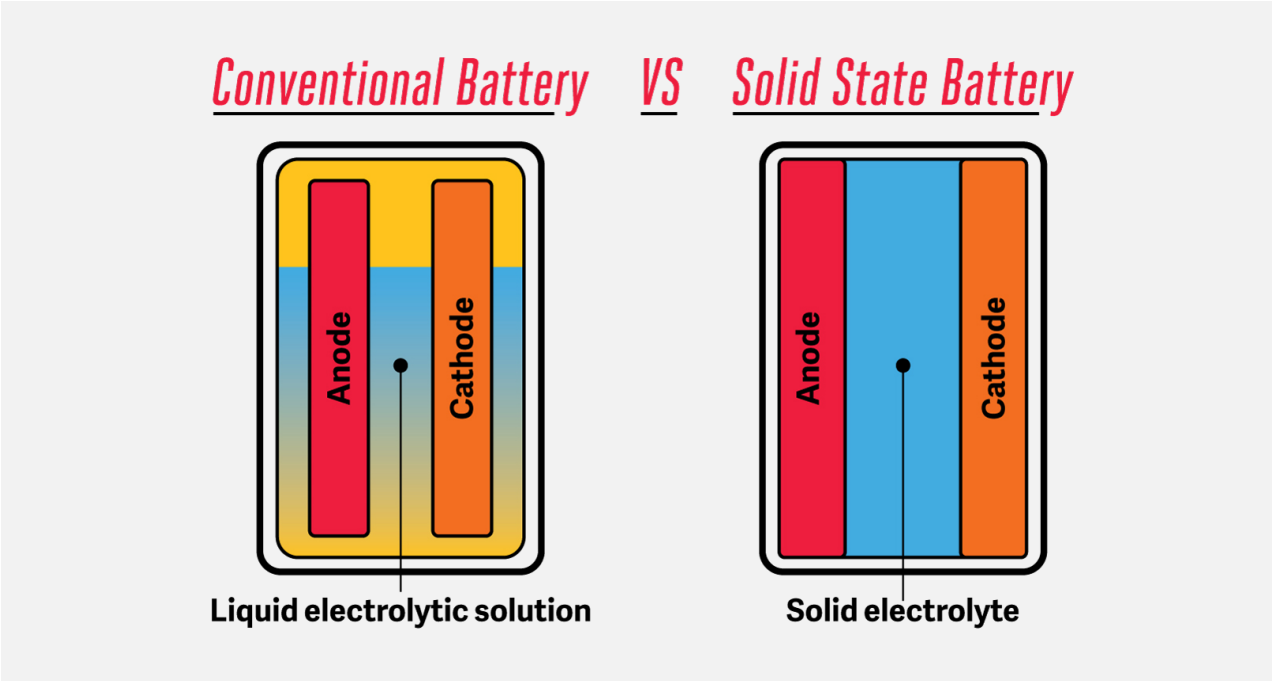

Prospective life-cycle assessment of an argyrodite type solid-state battery

Master's thesis in Industrial Ecology

SOFIE HJORTSBERG
ZACKARIAS HEYDORN

DEPARTMENT OF TECHNOLOGY MANAGEMENT AND ECONOMICS
DIVISION OF ENVIRONMENTAL SYSTEM ANALYSIS

CHALMERS UNIVERSITY OF TECHNOLOGY
Gothenburg, Sweden 2022
www.chalmers.se
Report No. E2022:061

REPORT NO. E2022:061

Prospective life-cycle assessment of an argyrodite type solid-state battery

SOFIE HJORTSBERG
ZACKARIAS HEYDORN

Department of Technology Management and Economics
Division of Environmental System Analysis
CHALMERS UNIVERSITY OF TECHNOLOGY
Gothenburg, Sweden 2022

Prospective life-cycle assessment of
an argyrodite type solid-state battery
SOFIE HJORTSBERG
ZACKARIAS HEYDORN

Report no. E2022:061
Department of Technology Management and Economics
Chalmers University of Technology
SE-412 96 Göteborg
Sweden
Telephone + 46 (0)31-772 1000

Cover: A visualization of the principal difference between a conventional liquid electrolyte battery and a solid-state battery. Illustration by William Joel, courtesy of The Verge and Vox Media.

Gothenburg, Sweden 2022

Prospective life-cycle assessment of
an argyrodite type solid-state battery

SOFIE HJORTSBERG
ZACKARIAS HEYDORN

Department of Technology Management and Economics
Chalmers University of Technology

Abstract

Rechargeable battery technologies are used in a variety of applications, and recently the use in electric vehicles and grid storage have received a lot of attention. This is largely because an electrified car fleet and improved grid-storage capacity (to offset the variable nature of renewable electricity production) are envisioned to reduce greenhouse gas emission. Today's dominant battery technology, the lithium-ion battery (LIB), is associated with safety issues, such as aggressive fires caused by thermal runaway. Furthermore, it is also associated with sustainability issues, such as leakage of toxic substances, energy intensive production and its content of critical and/or geochemically scarce materials, e.g. lithium, nickel, and cobalt.

Solid-state batteries (SSBs) are a novel battery technology utilizing solid instead of liquid electrolytes, which is the dominant design today. SSB cells are expected to become a future competitor to LIB cells due to potential for increased energy densities, higher safety and cyclability. In this work, the SSB literature was first reviewed to find a SSB cell with promising performance that has not been previously studied from an environmental life-cycle perspective. The battery cell chosen was an anode-free argyrodite-type SSB, which uses a silver-carbon nanoparticle layer to promote an even lithium plating when charged.

To identify environmental hotspots and benchmark the life-cycle environmental impacts of this battery cell at a point in time when it has reached scaled up production, a prospective life cycle assessment (LCA) with a cradle-to-gate scope was performed. The functional unit was defined as 1 kWh of theoretical storage capacity produced and the prospective LCA focused on climate change and mineral resource depletion impacts.

The prospective LCA concluded that the studied battery would perform comparably to LIBs when it comes to climate change, but that was dependent on the type of electricity source, heating, and cooling production assumed for the background system. An identified hotspot was the production of carbon nanofibers. Furthermore, the study showed that the short-term mineral scarcity performed similar in comparison with LIBs. The battery did, however, perform considerably worse regarding long-term mineral resource scarcity due to its silver content. This indicates that the battery might be unfit for large scale manufacturing unless the silver used in the separator layer can be reliably recycled or substituted. This was tested in a sensitivity analysis, where it was shown that replacing the silver with magnesium would reduce the long-term mineral resource depletion impact with 69%, the short-term mineral resource depletion impact with 29% and the climate change impact with 14%.

Keywords: Solid state battery, prospective life cycle assessment, solid electrolyte, argyrodite, climate change, mineral resource depletion

Sammanfatting

Laddningsbara batterier används redan idag i ett flertal olika applikationer, och inom den närmaste framtiden förväntas efterfrågan öka kraftigt. Detta beror till stor del på att ellagring (för att kompensera för ökad andel förnybar elproduktion med varierande produktion) och en elektrifiering av fordonsflottan ses som viktiga steg för att för att reducera utsläppen av växthusgaser. Den dominanta teknologin för laddningsbara batterier är i dagsläget litiumjonbatterier. Dessa batterier är associerade med säkerhetsproblem, såsom risk för svårsläckta bränder orsakade av den flytande elektrolyten. Litiumjonbatterier är dessutom associerade med vissa hållbarhetsproblem då de innehåller flertalet sällsynta och kritiska metaller, såsom litium, nickel och kobolt.

En sorts batterier som förväntas utmana litiumjonbatterierna är så kallade fastfasbatterier. Dessa batterier är en ny typ av laddningsbara batterier som innehåller en fast elektrolyt i stället för en flytande elektrolytvätska. Dessa batterier ses som en lovande utmanare då de har potential att nå hög energidensitet, kan laddas många gånger och undviker problemen med de svårsläckta bränderna. I denna rapport undersöktes först litteraturen om fastfasbatterier för att identifiera ett batteri som visat lovande prestanda på labb-nivå, men som ännu inte blivit studerat ur ett livscykelperspektiv. Med hjälp av en expertgrupp valdes ett fastfasbatteri som innehöll en elektrolyt av argyrodit-typ. Batteriet har en anod-fri design och innehåller ett lager med nanopartiklar av silver och kol för att möjliggöra en jämn uppbyggnad av litiummetall under laddning.

För att identifiera problemområden och jämföra miljöpåverkan från produktionen av detta batteri vid en tidpunkt då det nått storskalig produktion genomfördes sedan en prospektiv livscykelanalys med en systemgräns från vagga till port. Den funktionella enheten definierades till 1 kWh producerad lagringskapacitet, och påverkanskategorier i fokus var klimatförändringar och mineralresursknapphet.

Resultatet av den prospektiva livscykelanalysen var att det studerade batteriet verkar prestera likvärdigt med litiumjonbatterier gällande klimatförändringar. Ett stort bidrag till den påverkanskategorin som identifierades var produktionen av kolnanofibrer, framför allt om energi från fossila bränslen användes. Gällande mineralresursknapphet presterade fastfasbatteriet likvärdigt med litiumjonbatterierna på kort sikt, men avsevärt sämre på lång sikt på grund av användningen av silver. Detta indikerar att argyrodit-batteriet kan ses som olämpligt för uppskalad produktion om inte silvret kan substitueras. En sådan substitution testades i en känslighetsanalys som visade att om silver substituerades med magnesium så kunde påverkan för klimatförändringar reduceras med 14%, kortsiktig mineralresursknapphet med 29% och långsiktig mineralresursknapphet med hela 69%.

Nyckelord: Fastfasbatteri, argyrodit, fast elektrolyt, mineralresursknapphet, prospektiv livscykelanalys.

Table of Contents

Acknowledgements

This master thesis of 30 ECTS was conducted as the final step of the M.Sc. program in Industrial Ecology at Chalmers University of Technology. It was carried out at the department of Technology Management and Economics, division of Environmental Systems Analysis.

Firstly, we would like to extend our undying gratitude to our examiner Rickard Arvidsson and our supervisor Sanna Wickerts, both at the division of Environmental Systems analysis at Chalmers. Thank you for providing swift, relevant and continuous methodological support throughout our work and providing moral support at the times when that was greatly needed.

Secondly, we would like to thank Maciej Wysocki, Mats Zackrisson and Stacy Trey at the Research Institutes of Sweden (RISE) for your time and inputs regarding promising solid-state chemistries and battery cell manufacturing technologies.

Finally, we would like to thank Shizhao Xiong at the department of Physics at Chalmers for verifying our chosen battery cell to be a relevant object of study and also for sharing sources and general expertise regarding anode-free solid state battery designs.

Sofie Hjortsberg and Zackarias Heydorn
June 2022

Abbreviations

Abbreviation	Definition
AgNP	Silver nanoparticles
CNF	Carbon nanofibres
CPE	Composite polymer electrolyte
CSE	Composite solid electrolyte
CSI	Crustal scarcity indicator
CSP	Crustal scarcity potential
EOL	End of life
EUCAR	European Council for Automotive R&D
IA	Impact assessment
IEA	International energy agency
ISE	Inorganic solid electrolyte
ISO	International Organization for Standardization
IPCC	Intergovernmental Panel on Climate Change
LCA	Life cycle assessment
LIB	Lithium-ion battery
LE	Liquid electrolyte
PEO	Polyethylene oxide
RQ	Research question
SE	Solid electrolyte
SEI	Solid electrolyte interface
SPE	Solid polymer electrolyte
SSB	Solid state battery

Concepts

Concept	Definition
Battery cell	Basic electrochemical unit that provides a source of electrical energy by direct conversion of chemical energy. It consists of an assembly of electrodes, separators, electrolyte, container, and terminals.
Catholyte	Combination of active cathode material and electrolyte.
Coulombic efficiency	Efficiency with which charge (electrons) is transferred in a system facilitating an electrochemical reaction (Wang et al., 2021)
Electrochemical stability window	Range of potentials over which the Electrolyte phase is considered stable (Benabed et al., 2021)
Energy density	Amount of energy stored per unit of volume
Ionic conductivity	Movement of charge in response to the motion of the electrical charge of an ion (Owen, 1989)
Lithium-ion transference number	Ratio of lithium-ion mobility to the total ionic mobility (Shigenobu et al., 2020)
Specific energy	Amount of energy stored per unit of mass

1. Introduction

In this section, the role of rechargeable batteries in the modern society is presented. Subsequently, the technology of solid-state battery (SSB) cells is introduced, and four different solid electrolyte families are discussed. After that comes an introduction to the prospective life cycle assessment (LCA) method as well as an overview of previously conducted LCAs of SSB cells. Lastly, the aim of the study is presented together with specific research questions that need to be answered to fulfil the aim.

1.1 Background

Energy is one of the most critical resources that enables contemporary society to function the way it does. The current supply of energy is mainly provided by burning fossil fuels, a practice proven to lead to destabilization of the planetary climate system. However, reducing the use of these are slow as society still seems unable to avoid using and subsidizing them (IPCC, 2022). From a technological point of view, one of the few feasible paths to reducing the global fossil fuel dependency seems to be to rapidly replace current energy infrastructures with structures supporting renewable electricity production, such as wind turbines and photovoltaics (Ma et al., 2021). To balance up for an increasing share of such variable electricity production technologies, the electricity infrastructure needs to be complemented with increased capacity for grid storage. One of the well-established ways of increasing grid storage capacity is by use of rechargeable batteries (Loveless, 2022).

Another sector that uses a major share of all rechargeable batteries manufactured today and is expected to grow considerably in the near future is the electric vehicle (EV) market (Sun, 2020; IEA, 2021). The fact that a non-trivial amount of fossil fuels is currently used to fuel cars, trucks and planes have increased in focus in many parts of the world due to the signs of climate change. This has incentivized many automotive manufacturers to initiate electrification programs (IEA, 2021).

There is also a third important area of application that also requires a considerable number of rechargeable batteries: consumer electronics (CE). The estimated global growth in battery demand by these three key sectors until 2030 is shown in Figure 1.1.

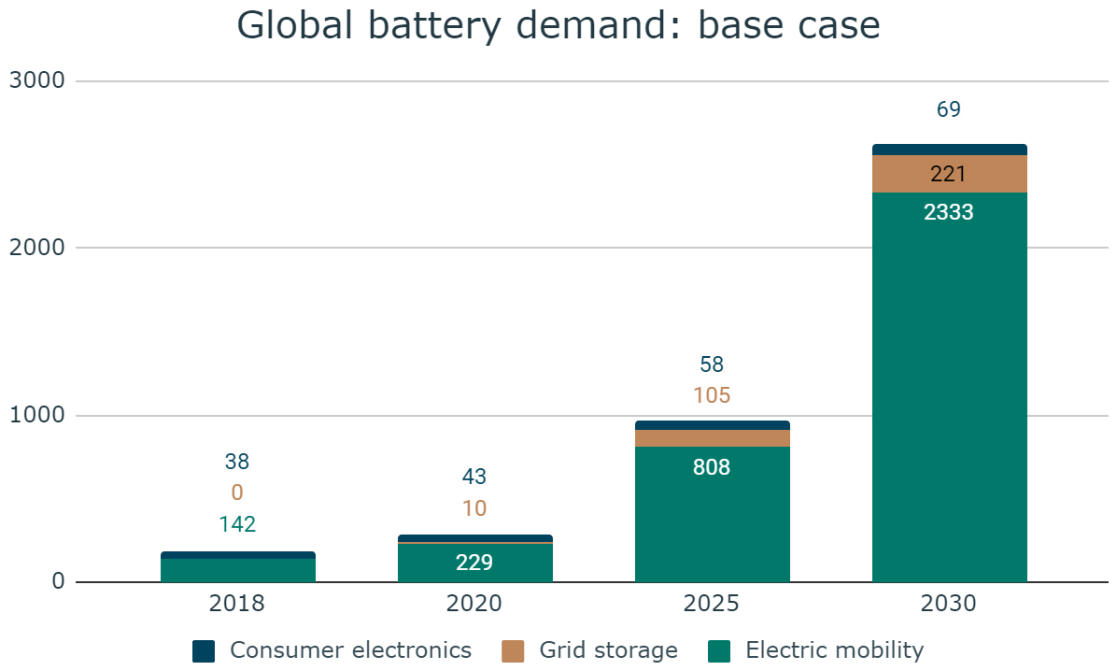

Figure 1.1: *Estimated growth in the battery demand by sector from the EU 2030+ battery roadmap. Adapted from Edström et al. (2020).*

While there are no exact boundaries for what constitutes a "high performance" battery cell, the general view is that a battery cell intended for EV applications needs to have high energy density, specific energy, fast charging, and long cycle life. Those requirements should be fulfilled while also maintaining a low risk of exploding (EUCAR, 2019). Realizing the important part batteries will play in the future, the European Union (EU) has set up performance goals for batteries cells for EV applications in 2030. These goals state that an EV battery cell in 2030 should have a specific energy of at least 450 Wh/kg and an energy density of at least 1000 Wh/L (EUCAR, 2019).

Currently, the dominating rechargeable battery cell technology is the lithium-ion battery (LIB) (Boaretto et al., 2021). LIB cells have been widely diffused due to advantages such as high energy density and manufacturability. They do, however, also come with drawbacks related to safety (Boaretto et al., 2021) and sustainability challenges, such as their usage of rare and critical materials (Pasta et al., 2020). The specific energy of an LIB cell is expected to have a theoretical maximum of 350–400 Wh/kg (Fan et al., 2018), which is not enough to meet the future requirements of more advanced and demanding emerging technologies (Fan et al., 2018). Hence, a next generation of secondary batteries is required to fulfill these demands. There are many types of competing emerging technologies attempting to replace LIB cells as the dominant technology. One such technology is the SSB cell, which is viewed as one of the most promising alternatives for the next generation of batteries (Ma et al., 2018; Pasta et al., 2020). SSB cells are further discussed below.

1.2 Solid state batteries

A SSB cell uses a solid electrolyte (SE) instead of a liquid electrolyte (LE), which currently is the dominating design for LIB cells and similar types of batteries (Boaretto et al., 2021). There are several benefits of moving away from LEs. A solid electrolyte has a much higher mechanical strength than a liquid electrolyte (Boaretto et al., 2021). This means that they have the potential to better withstand external and internal forces during usage. Higher mechanical strength can lead to increased lifespan of the battery cell, since one of the factors that renders liquid electrolyte battery cells unusable is the growth of dendrites (see Figure 1.2A) from the anode (Varzi et al., 2020). In addition, dendrites formed with narrow roots may detach when cycling is prolonged, resulting in "dead" lithium (see Figure 1.2B) (Foroozan et al., 2020). In an LIB cell, dendrites may grow so large that they penetrate the separator material in the cell, leading to a short circuit and potentially a catastrophic failure called "thermal runaway". During thermal runaway, the battery cell ignites and can be difficult to extinguish (Varzi et al., 2020).

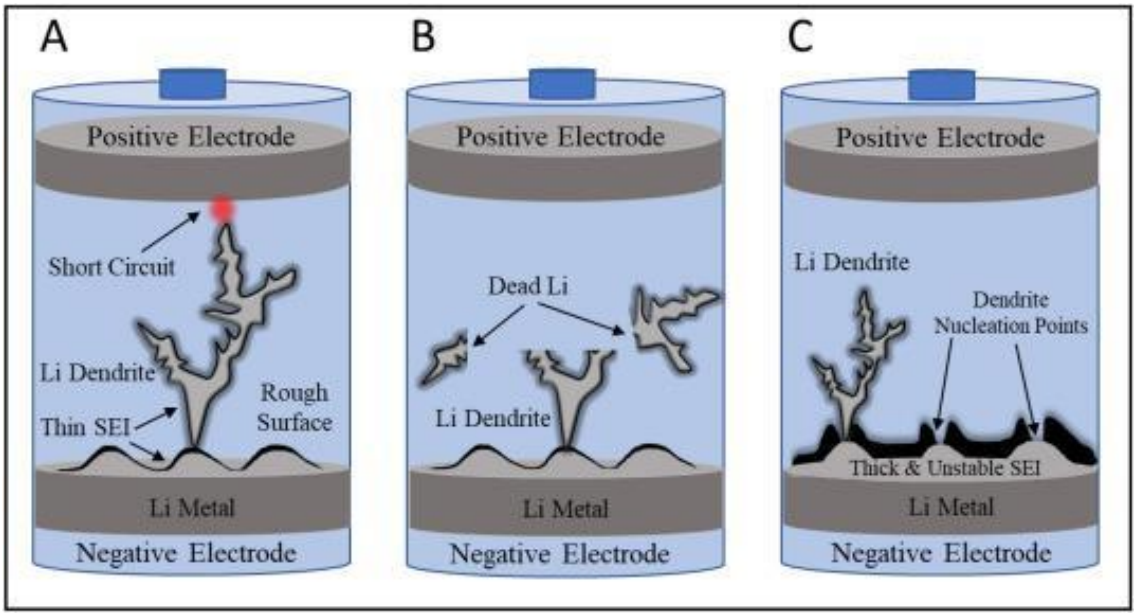

Figure 1.2: *Dendrite growth from lithium metal anode. Obtained from Foroozan et al. (2020) under license nr: 5324110301633.*

A: Dendrite growth from lithium penetrating the separator material leading to contact with the cathode material, leading to short circuit of the battery.
B: Formation of electrochemically inactive, or dead, Li formed by Li dendrites with narrow roots during prolonged cycling.
C: Development of thick and mechanically unstable solid electrolyte interface (SEI).

As mentioned, LIB cells also have difficulties reaching a specific energy high enough to meet the high-performance requirements of emerging technologies. One solution to increase both the specific energy and energy density of the battery cells is by using lithium metal as an anode, which has the potential to increase the energy density by 50% and specific energy with 35% if compared to the commonly used graphite anode (Kim et al., 2021). The issue with combining lithium metal anode with LEs is that they experience low, columbic efficiency which leads to rapidly declining performance (Yu et al., 2021a). Due to repeated lithium deposition and dissolution throughout the usage of the battery cell, the anode experiences changes in the volume, which the SEI is not mechanically stable enough to accommodate. This has the potential to initiate local dendrite formation and consumption of excess lithium and electrolyte (Foroozan et al., 2020). Continued consumption of LE and lithium leads to increasing thickness of the SEI layer (Figure 1.2C), which causes the cell capacity to decrease. (Varzi et al., 2020). Many solid electrolytes have the major benefit of being compatible with the use with lithium metal anodes (Boaretto et al., 2021). SSB cells using lithium metal anodes are claimed to have the potential to reach specific energies as high as 500 Wh/kg (Ma et al., 2021).

When it comes to recycling and recovery of valuable materials from spent batteries, the SSB cell has a couple of potential advantages compared to LIB cells. One such advantage is that SEs do not have the same problems with flammability as LIB cells (Foroozan et al., 2020), which could greatly reduce safety challenges during disassembly. Another benefit is that SSB cells are often designed in a stackable format, meaning that before disassembly, they can be discharged at the pack level (Tan et al., 2020). Furthermore, in a study by Tan et al. (2020), SSBs show promise for being possible to recycle with new simple methods, consuming low amounts of energy.

However, even though SSB cells show great promise and hold several theoretical advantages over LIB cells, the technology is still in an early stage of development (Ma et al., 2021). There still remain many challenges that material scientists, entrepreneurs and engineers need to overcome before the technology is ready for large-scale implementation. A group of prominent battery experts and researchers recently had a conference where they defined and categorized knowledge gaps that still need to be addressed before full commercialization of SSB cells (Albertus et al., 2021). They divided the remaining gaps into the categories: material science, processing science and design engineering (Albertus et al., 2021). Some examples of these gaps are presented below.

The materials in an SSB cell need to be electrochemically stable during the operation and be compatible with all other materials in the battery. Furthermore, they need to be able to maintain a stable interface between the layers

of the battery cell in order to maintain performance (Albertus et al., 2021). The issue of poor interfacial contact is one of the main challenges remaining for SSB cells (Ma et al., 2021) and can lead to low coulombic efficiency, poor power performance and unstable cycling performance (Sun., 2020).

Another challenge connected to SE materials is that cycling of the battery cell leads to volume expansion of the materials, which causes mechanical stress (Pasta et al., 2020). If the SE used is too stiff or brittle, this expansion can result in delamination or cracking at the interface contacts (Pasta et al., 2020). Many SE materials are also unstable in contact with moisture and face electrochemical stability issues when they come in contact with lithium metal (Varzi et al., 2020).

One way that processing techniques can increase interfacial contact is through the process of sintering. This is commonly used in SSB cell manufacturing to densify electrolyte materials and to improve the interfacial contact between components (Albertus et al., 2021; Boaretto et al., 2021). Sintering is conducted by pressing the batteries at high temperatures and long duration times to achieve the desired performance (Pasta et al., 2020). Sintering is, however, unsuitable for large scale-manufacturing due to high energy requirements (Schnell et al., 2018). Hence, other densification processes need to be developed before SSB cells can compete with LIB cells (Pasta et al., 2020).

Many innovations in the SSB field include new and advanced materials that are not compatible with LIB cell manufacturing infrastructure (Albertus et al., 2021). This has resulted in a tension between developing a SSB cell that could be rapidly scaled up using current infrastructure, and what some argue are the "true innovations", which would require much larger investments and time to develop (Albertus et al., 2021). The scalability of different laboratory processes is one of the big discussion topics within the SSB field (Varzi et al., 2020).

How big of a problem each of these challenges are depends greatly on which specific SE material that is considered for the SSB cell. Currently, there are many alternative SE materials investigated, and many promising designs are being considered (Herle et al., 2020). The different SEs can be categorized in different ways, but a common way found in, e.g., Boaretto et al. (2021) is to divide the electrolyte materials into the families: sulfides, oxides, polymers, and composite SEs. Each family includes many different materials, but they share some characteristics and hence have their own benefits and disadvantages. Below, the four families of SEs are discussed in more detail.

1.2.1 Sulfides

One reason for why sulfide-based SEs are considered promising is their higher ionic conductivity than any other SE family (Varzi et al., 2020). Many sulfides have shown ionic conductivity results comparable, or even higher than the currently dominating LIB technology, which uses LE technology (Zhang et al., 2019; Varzi et al., 2020). Sulfide SEs are also generally softer than other SEs, which can allow for improved contact between the electrolyte and electrode materials (Varzi et al., 2020). This improves the electronic and ionic transport at the interfaces, reducing the chances of capacity fading and battery cell failure (Boaretto et al., 2021). Due to their softness, they are also expected to better withstand changes in volume of the electrode during the battery cycling (Pasta et al, 2020). Some sulfide SEs can be densified at low temperatures, drastically reducing the energy intensity of the sintering (Pasta et al., 2020; Varzi et al., 2020). Also, recycling possibilities appear to be especially beneficial for sulfide-type SE, since dissolution of those electrolytes could be done using cheap and safe solvents, compared to oxide-type SEs (Tan et al., 2020).

A major limitation of electrolytes in the sulfide family is that they generally are very hygroscopic, meaning that they are sensitive to moisture (Varzi et al., 2020). If they come into contact with humid air they tend to produce toxic hydrogen sulfide gas (Li et al., 2021). Due to their highly reactive character, most of the manufacturing must be performed in dry-air conditions (Pasta et al., 2020; Schnell et al., 2018). Many sulfides are also unstable in contact with metallic lithium and some high voltage cathode materials, which might lead to reduced performance (Varzi et al., 2020). To solve these interface reactivity problems, many sulfide-based SSB cells require an interface layer and/or protective coating to act as a buffer layer and thus prevent reactions (Varzi et al., 2020).

Within the sulfide SE family, there is a large variety of chemistries developed, including glassy sulfides (e.g. Li_2S–SiS_2, Li_2S–P_2S_5, Li_2S-GeS_2), crystalline sulfides (e.g. $Li_{4-x}Ge_{1-x}P_xS_4$ and $Li_{4-x}Sn_{1-x}As_xS_4$,), thio-LISICON (e.g. $Li_{10}GeP_2S_{12}$ (LGPS)) and argyrodite (Li_6PS_5X (X = Cl, Br)) (Boaretto et al., 2021). Among these, LGPS have been highlighted as promising due to its soft mechanical properties (Boaretto et al., 2021) and high ionic conductivity (Varzi et al., 2020). A drawback with that material is, however, the use of the expensive and critical metal germanium, which has not yet been possible to substitute (Boaretto et al., 2021). Argyrodite-type SEs have

also shown comparable results for ionic conductivity at room temperature and have also attracted interest (Boaretto et al., 2021; Yu et al., 2021).

1.2.2 Oxides

Oxide-type SEs usually have high electrochemical stability, are compatible with lithium-metal anodes and are less sensitive to degradation at high voltages than the sulfides (Varzi et al., 2020). They are also more stable in air, although still unstable in contact with water or carbon dioxide (Varzi et al., 2020). This makes the oxide-type SEs easier than the sulfide-type to manufacture on a large scale, since not as many process steps need to be performed in a dry room (Pasta et a., 2020).

Disadvantages include that oxide SEs tend to be rigid, which means there is a risk for the SE to crack during cycling. They also require high temperature sintering to reach desired density and ionic conductivity (Pasta et al., 2020). This also leads to interfacial resistance, and their brittleness may make the performance of the battery cell unreliable (Ma et al., 2021).

The variation of battery cell chemistries within the oxide SE family is wide, and the advantages and disadvantages vary accordingly (Fan et al., 2018). Oxide-type SE include: LISICON (Li14Zn(GeO4)4), NASICON ($Li_{1+X}Al_XTi_{2-X}(PO_4)_3$ (LATP)) and $Li_{1+X}Al_XGe_{2-X}(PO_4)_3$ (LAGP)), perovskites ($Li_xLa_xTiO_3$ (LLTO)), garnet ($Li_7La_3Zr_2O_{12}$ (LLZO)) and LiPON (Li_3PO_4) (Boaretto et al., 2021).

Some of the most promising oxide SEs come from the NASICON family, which have been researched due to their high stability against moisture, high ionic conductivity, and wide electrochemical stability window (Fan et al., 2018; Boaretto et al., 2021). However, like many other oxide SEs, the issues with cracking have not yet been solved, which leads to poor interface stability (Boaretto et al., 2021). Another widely studied oxide SE is the garnet family, which also shows promise due to the high ionic conductivity and good stability against lithium-metal anode (Xia et al., 2019). Both these promising chemistries include several scarce and/or critical minerals, such as lanthanum, germanium and titanium, making sustainable large-scale manufacturing potentially challenging.

1.2.3 Polymers

SEs from the polymer family usually combine a polymer host and an alkali metal salt in a solid matrix (An et al., 2022). The polymer SEs have many advantages compared to the other families. They are flexible, light weight, highly processable and can sustain good contact with electrodes during use (Boaretto et al., 2021). Furthermore, they have good thermal stability, low flammability and are highly resistant against cracking (An et al., 2022).

Polymers is also the family of SEs that have been studied for the longest time and thus are the one that has come farthest in terms of commercial application (Boaretto et al., 2021). An example of this is the first commercial EV using a SSB cell, the so-called "blue car", which was introduced on French streets in 2011 (Garcia et al., 2019). The SSB cells in that car used a polyethylene oxide (PEO) SE, proving the viability of SSB cells for EV applications (Garcia et al., 2019).

On the other hand, SEs from the polymer family generally suffer from low ionic conductivities, a narrow electrochemical stability window and low lithium-ion transference in comparison with the other families (An et al., 2022; Meng et al., 2022). In summary, polymer-based SEs have a good possibility to be manufactured at large scales in the short term, but will likely not be enough to manifest many of the major benefits of SSB cells. Many researchers are trying to "get the best of both worlds" by incorporating polymer-based SEs in composite materials to increase ductility and support good interface contact between electrodes and electrolytes (An et al., 2022).

1.2.4 Composite

Composite SEs usually consist of a softer polymer-based SE in combination with a stiffer SE. They can be designed either as a laminated "sandwich" or as different types of mixes between polymers such as PEO and different inorganic particles (Boaretto et al., 2021). The incorporated particles aim to increase the ionic conductivity and mechanical properties of the composite. They are usually SEs from the sulfide or oxide family, but can also be different types of nanofillers, metal-organic frameworks and cellulose (Tang et al., 2021).

Composite SEs are an attempt to complement the benefits and negate the drawbacks of single materials (Meng et al., 2022). As can be seen in Figure 1.3, the composites succeed in this by offering a balanced performance in many of the categories relevant for SE materials. But being balanced in most aspects comes at the cost of not

being the best at anything. Laminated types of composite SEs also face extra interfacial challenges, since there are more layers that need to maintain good contact (Varzi et al., 2020). Many composites are also still facing challenges regarding thermal stability, manufacturing cost and compatibility with the lithium metal.

Figure 1.3: *Radar diagram of solid electrolyte families. Obtained from Boaretto et al. (2021).*

In the previous sections, some of the material and manufacturing gaps described also by Albertus et al. (2021) have been discussed. In the subsequent section, a promising development regarding the design engineering gaps for SSB cells is discussed.

1.2.5 The anode-free design

One design strategy that has recently attracted academic interest is the anode-free SSB cell (Huang et al., 2022). As the name implies, these types of batteries contain a cathode or a catholyte, two current collectors, a solid-state electrolyte and usually some sort of separator layer, but no anode. An anode layer instead forms inside the battery cell when charged for the first time. During the first initial charging, lithium ions from the cathode forms a lithium plating layer between the current collector on the anode side and the separator layer or the solid electrolyte (Heubner et al., 2021).

There are two primary benefits aimed to be achieved by designing a battery cell without an anode. First, removing one of the components in the cell could help reducing the complexity in the SSB production, which could lead to reduced environmental impacts and manufacturing costs (Heubner et al., 2021). A common practice for SSB cells with a lithium metal anode is to include excessive amounts of lithium, increasing both the environmental and production costs, also contributing with decreased energy density (Heubner at al. 2021). An anode-free design is designed without this excess of lithium and could potentially be easier to recycle due to the reduced material complexity (Heubner et al., 2021; Varzi et al., 2020).

The second major benefit of the anode-free design is that in a battery cell without an anode, the catholyte can take up a larger share of the volume and mass of the battery. This is considered close to an ideal battery structure as it in theory would lead to increased volumetric and gravimetric energy densities (Albertus et al., 2021; Heubner et al., 2021). Heubner et al. (2021) estimates that the maximal specific energy and energy density of a

SSB cell using a lithium-metal anode would be around 390 Wh/kg and 1200 Wh/L respectively, whereas an anode-free design using similar cathode materials could reach up to 400 Wh/kg and 1500 Wh/L, due to a higher share of the battery consisting of active materials (Albertus et al., 2021; Heubner et al., 2021).

Lithium anodes are, however, used in batteries for a reason. An anode-free design in combination with a SE could have a potential problem with decaying capacity due to lithium being consumed during operation. As previously mentioned, an anode free battery cell would usually not contain any excess lithium This means that potential losses of lithium during cycling result in a decaying capacity. To keep a desired energy density and long cycling life, a coulombic efficiency of the battery cell close to 100% is required (Heubner et al., 2021).

1.3 Prospective LCA

To evaluate the total life cycle environmental impacts of technologies, life cycle assessment (LCA) is a method that has been applied to a range of technologies, including batteries (Peters et al., 2017). The LCA methodology is usually used to evaluate environmental impacts for product or services that currently are mature (Buyle et al., 2019). However, recently there has been an increased interest from academia and industry to find ways to use the methodology for future-oriented purposes, such as assessments of emerging technologies (Buyle et al., 2019). Emerging technologies are often expected to contribute greatly to sustainable development, and it is therefore important to evaluate whether they will lead to that desired outcome (Thonemann et al., 2020). The earlier an emerging technology is studied, the larger the uncertainties will be, but it will also be easier to influence the design of the technology. This is known as "the Collingridge dilemma" (Collingridge,1982).

There are several variants of future oriented LCA methodologies. This includes exploratory, anticipatory, ex-ante and prospective LCA (Guinée et al., 2018). While some practitioners make distinctions between the different types, there still seem to be no clear consensus of the definitions and terminology. Some argue that efforts to differentiate between them are unnecessary, since the commonalities between the variants are bigger than the differences (Cucurachi et al., 2018). Furthermore, the method still needs to be adapted to the specific questions that the study aims to answer (Guinée et al., 2018). For this study, the term prospective LCA was used, defined by Arvidsson et al. (2017) as: "An LCA is prospective when the (emerging) technology studied is in an early phase of development (e.g., small-scale production), but the technology is modeled at a future, more-developed phase (e.g., large-scale production)." As indicated by the definition, prospective LCA often attempts to evaluate impacts of emerging technologies at a future point of time when the technology is manufactured at large-scale.

Due to its hypothetical nature, prospective LCA studies often lack primary empirical data, leading to uncertain results. Limited knowledge is an inevitable part of prospective studies, and the challenges that follow can be difficult to overcome. According to a review by Thonemann et al. (2020), some challenges common for prospective LCA studies are comparability, data, and uncertainties.

As shown in Figure 1.4, challenges with data are not limited to the availability. Often, it becomes necessary to scale data in order to assess potential future impacts. The scaling can be done using different methods, such as diffusion of innovation principles (Sharp and Miller, 2016), power law relationships (Caduff et al. 2011), predictive forecasts from institutions or scenario ranges corresponding to best and worst cases (Arvidsson et al., 2017). There are also a few frameworks available for scaling up LCA data of production processes (Piccinno et al., 2016; Fazeni et al., 2014). These are meant to guide the choices when attempting to scale data from lab-scale to industrial scale.

Despite the challenges of assessing emerging technologies, there have been a few attempts to conduct LCA of SSB cells. The next subsection gives a brief overview of all identified published LCA studies of such studies.

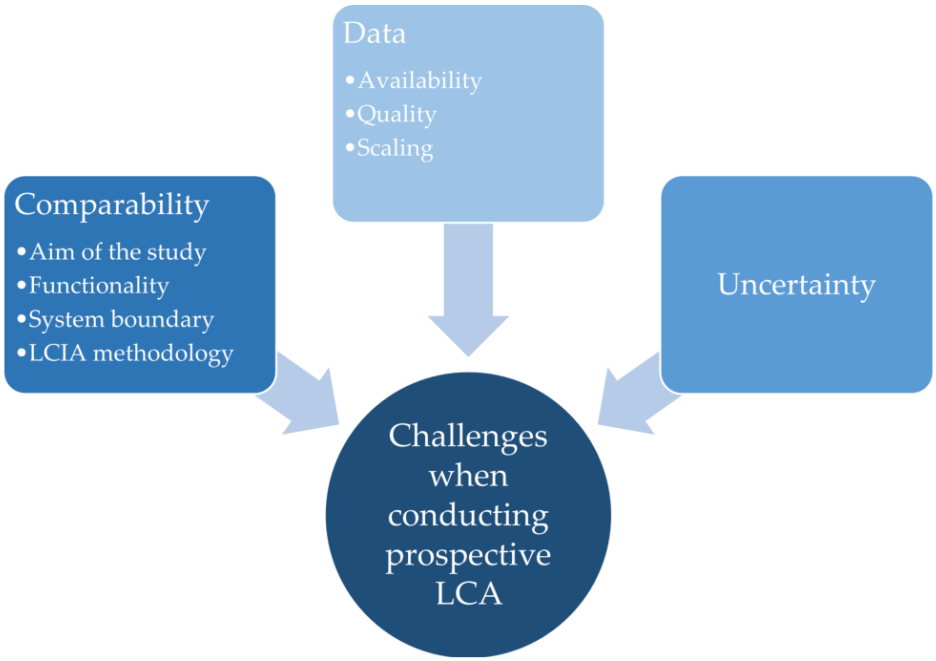

Figure 1.4: *Challenges when conducting prospective LCA. Obtained from Thonemann et al. (2020)*

1.4 Previously published LCA studies of SSB cells

As of the publication date of this study, there are only a few studies that attempt to investigate life cycle environmental impacts of SSB cell production from cradle to gate. The ones identified cover a variety of chemistries and are presented in Table 1.1.

Table 1.1: *Previously published life-cycle studies of SSB cells.*

Study	Anode	Cathode	Electrolyte	Electrolyte Family
Lastoskie and Dai (2015)	Li/C	Several	LiPON	Oxide
Troy et al. (2016)	Li metal	LCO	LLZO	Oxide
Keshavarzmohammadian et al. (2018)	Li metal	Pyrite (FeS_2)	Li_2S-P_2S_5	Sulfide
Smith et al. (2021)	Li metal	LFP/LiTFSI	LLZTO	Oxide
Zhang et al. (2022)	Li metal	NMC	LATP	Oxide

A commonality that could be distinguished among the studied chemistries was that all of them used a lithium metal anode, which goes in line with that being one of the main benefits of the SSB technology (Boaretto et al., 2021). Furthermore, only the study by Keshavarzmohammadian et al. (2018) considered a SE belonging to the sulfide family, while the rest of the studies all considered different types of oxide-type SEs.

Further details on those of the LCA studies of SSB cells used to compare the results of the present study can be found in Section 3.9.

1.5 Aim and research questions

The aim of this study was to survey the field of SSB cell s to identify dominant designs, promising materials and common obstacles for industrialized production. Furthermore, the aim was to select an SSB cell that were deemed likely to reach large-scale production but had not been studied from a life cycle perspective. Lastly, the potential future environmental impacts of producing the chosen battery cell were to be assessed by prospective LCA.

To fulfil the aim, the following research question were answered:

RQ1: Is there a battery cell existing today using a promising SSB chemistry likely to become produced at large scale and that has not been previously studied from a life cycle perspective?

RQ2: What would be the cradle-to-gate environmental impacts for that SSB cell at a point in time where it has reached large-scale production, and how would those impacts compare to other battery technologies?

RQ3: Would there be any likely environmental or resource hotspots associated with large-scale production of the chosen SSB cell?

2. Method

Certain methods were selected to fulfill the aim of the study. Section 2.1 describes the pre-study method used to answer RQ1. Subsequently, Section 2.2 describes the prospective LCA method used for answering RQ2 and RQ3.

2.1 Pre-study

To answer RQ1, a literature search was performed with the aim of identifying promising material choices and dominating SSB cell designs, as well as remaining obstacles before commercialization. The literature search focused on review articles from established journals summarizing promising battery chemistries and manufacturing obstacles. In parallel with the literature study, meetings were held with a group containing LCA and battery manufacturing experts from the research institute RISE to develop the criteria listed below. The SSB cell chosen for this study should preferably:

I. Be proven to work in a lab setting.
II. Be reasonably suited for large scale production.
III. Have specifications making it realistic for use in future EV applications.
IV. Contain a solid electrolyte with few critical and/or rare elements.

RQ1 also specifies that the battery cell should not have been studied from a life cycle perspective. To verify that, a review of all published LCA studies of SSB cells was conducted, as presented in Section 1.4. Subsequently, three SSB cells were chosen that fulfilled most of the criteria on the list. The three options were then presented to the same expert group previously consulted. Based on the feedback from that presentation, one of the battery systems was chosen and further verified to be a reasonable choice through e-mail discussions with battery researchers at Chalmers University of Technology.

2.2 Prospective LCA

To answer RQ2 and RQ3, prospective LCA was chosen as the method to assess the environmental impact of the selected SSB cell. The LCA methodology is standardized by the International Organization for Standardization (ISO), with the latest guidelines found in 14040:2006 (ISO, 2006). According to the ISO standard, LCA includes four procedural steps: goal and scope definition, inventory analysis, impact assessment and interpretation, shown in Figure 2.1. The steps in an LCA are not strictly sequential; in particular the interpretation runs in parallel with the other steps. The ISO standard, however, does not provide detailed guidelines for each of the procedural steps. Therefore, many choices in each step vary from study to study, depending on the goal and intended audience. Importantly, for this study, the current ISO standard does not specify how to perform a prospective LCA. Instead, guidance and recommendations regarding methodological choices can be found in scientific articles (Arvidsson et al., 2017; Buyle et al., 2019; Thonemann et al., 2020).

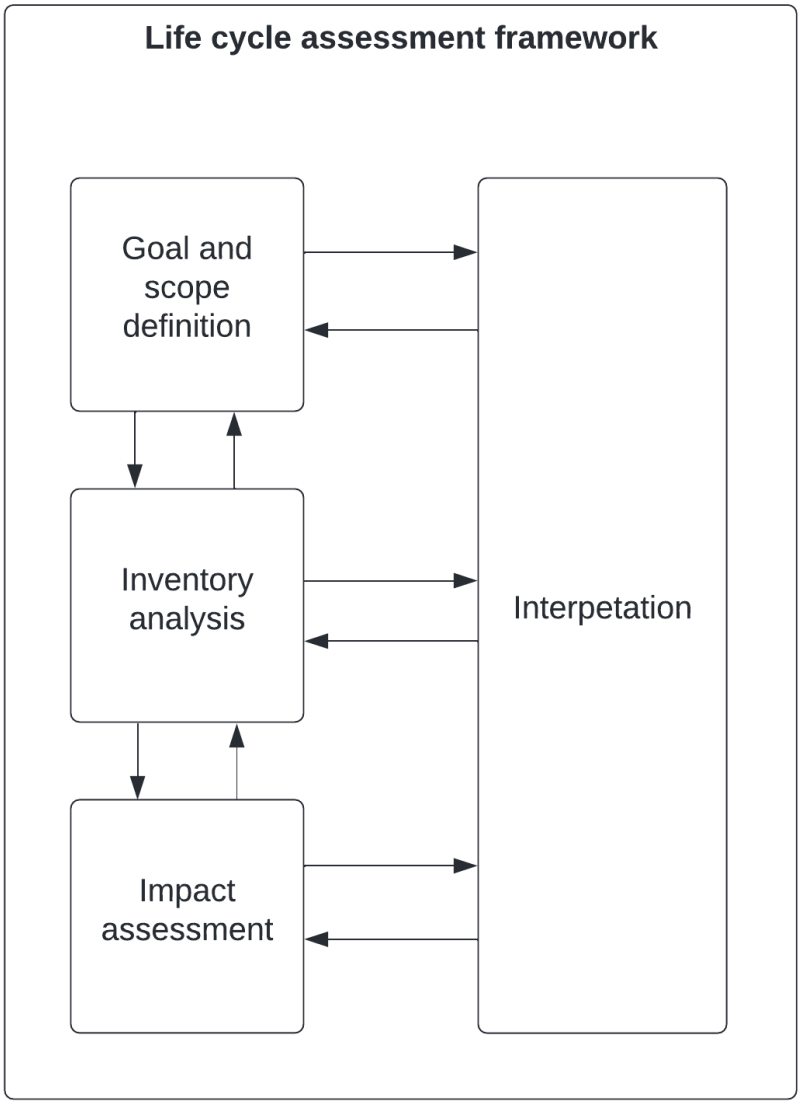

Figure 2.1: *The steps of an LCA. Adapted from the International Organization for Standardization (2006).*

2.2.1 Goal and scope definition

The goal and scope definition is a crucial step in LCA, which sets the frame of the study and states the modeling choices. The goal and scope include stating the purpose, intended application, target audience, describing the system under study, selecting the environmental impact categories to assess, stating the data quality requirements, and defining a functional unit (Baumann and Tillman, 2004). The scope of an LCA typically includes assessing a selection of relevant impacts from cradle to grave, meaning from raw material extraction to end of life (EOL), but other system boundaries are also possible, for example cradle-to-gate and gate-to-gate (Baumann and Tillman, 2004).

2.2.2 Life cycle inventory

The life cycle inventory (LCI) includes setting up a flowchart to visualize the system under study. Then, data is to be collected, calculated, and analyzed for all processes in the studied system (Baumann and Tillmann, 2004). According to Arvidsson et al. (2017), foreground data are typically obtained from scientific articles, patents, expert interviews, unpublished experimental data, and process modeling in prospective LCA. Background data, on the other hand, are usually obtained from databases. In a prospective LCA, the obtained data might also need to be scaled up to assess the potential future impacts, unless status quo is a reasonable assumption.

2.2.3 Life cycle impact assessment

The life cycle impact assessment (LCIA) step, the data collected in the LCI is translated into potential environmental impacts according to different impact categories. This step helps communicating the results and makes them comprehensible and easier to compare with other LCA studies (Baumann and Tillman, 2004). When it comes to LCIA, there are both mandatory and optional elements according to the ISO standard 14040:2006.. The mandatory steps include selection of impact categories, category indicators and characterization methods, and the optional steps include normalization, grouping and weighting.

There are several existing LCIA methods (Hauschild and Huijbregts, 2015), all using different impact categories and characterization factors, presenting the results either by midpoint or endpoint. Midpoint categories are focused on single impacts categories, while endpoint categorization aggregates those results to a higher level when presenting the results (RIVM, 2011).

2.2.4 Interpretation

In the interpretation phase of an LCA, the results are related to the goal and scope of the study to be able to draw conclusions and recommendations. The interpretation sometimes includes conducting different types of result analyses, such as a contribution analysis. Interpretation also includes testing the robustness of the results, where the methodological choices and data collected can be evaluated more specifically. A common method for testing uncertainty is to conduct a sensitivity analysis (Baumann and Tillman, 2004). Sensitivity analysis includes changing input parameters to identify which parameters are most sensitive to changes (Baumann and Tillman., 2004).

It is not only important to be aware of and estimate uncertainties, but they should also be communicated in a clear and transparent way. This is not stated in the ISO standard, but Thonemann et al. (2020) recommends using five criteria originally proposed by Gavankar et al. (2015) as guidelines when uncertainties are communicated. The criteria are: 1) acknowledgement of uncertainty, 2) provide context of the issues the uncertainty is affecting, 3) constructing scenarios for scaling of the future, 4) using a common language to describe subjective probabilities when data is lacking, and 5) access to information about the uncertainties.

3. Goal and scope definition

This section defines the goal and scope of the LCA. This includes the target audience, system boundaries, the choice of impact categories, uncertainty analysis, comparison, and software choices. Furthermore, a description and motivation behind the choice of battery cell is provided.

3.1 Goal and target audience

The goal of the LCA was to investigate the cradle-to-gate life-cycle environmental impacts for the chosen SSB cell at a time when it has reached large-scale manufacturing.

The results of the study were intended to contribute to an ongoing research project conducted at Chalmers University of Technology, called "Life cycle assessment of future battery chemistries – high storage capacity without scarce resources?" The main target audience of the study is researchers and engineers involved in development of SSB cells and their production. This study can further assist in guiding the direction of research within the field of SSB cells by identifying environmental hotspots and comparing the results with competing battery technologies.

3.2 Choice of battery cell

The battery cell chosen as the object of study for this LCA was an anode-free battery design using a sulfide-based argyrodite-type SE (Li_6PS_5Cl) and a silver-carbon (Ag-C) separator layer, first developed by Lee et al. (2020) who work for the company Samsung. An overview of the chosen battery cell composition can be seen in Figure 3.1. Hereafter in this study, the chosen battery is referred to as the "argyrodite battery".

The argyrodite battery cell could be used with different cathode materials, but the prototype studied had an energy dense NMC 811 catholyte. This battery system is considered interesting for this study as it was mentioned as especially promising in several reviews due to the impressive performance results obtained at the lab-scale (Varzi et al., 2020; Nanda et al., 2021; Yang et al., 2021; Bonnick and Muldoon, 2022), but had not yet been studied from a life cycle perspective (Table 1.1). Furthermore, according to Heubner et al., (2021), the argyrodite battery cell is the only SSB cell so far that has reached a coulombic efficiency close to 99.9%, meaning that it could compete with established battery systems when it comes to cycling stability. The argyrodite battery also fulfilled criterion I-IV as they are listed in Section 2.1 reasonably well, which is discussed briefly below.

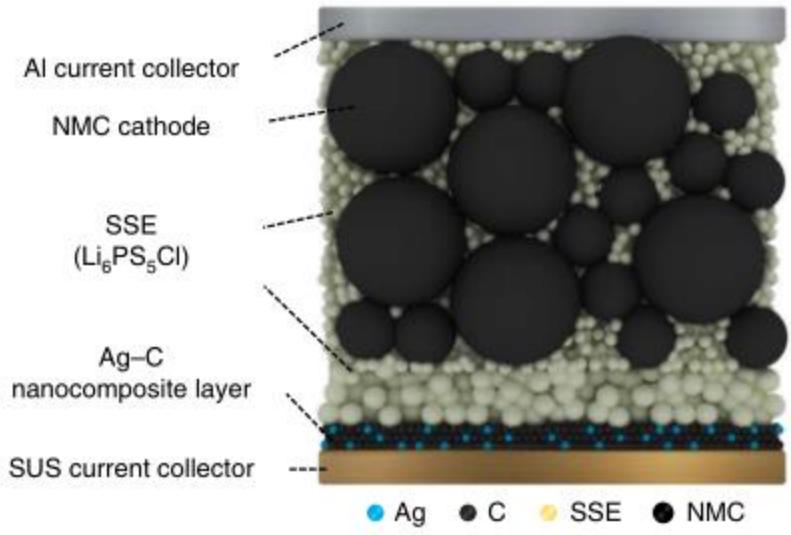

Figure 3.1: *Overview of the argyrodite battery. Obtained from Lee et al. (2020) under license nr: 5323020188681.*

Criterion I stated that the battery cell needed to be proven to work in a lab setting. The argyrodite battery cell from Lee et al. (2020) showed impressive cyclability when run with added heat and slight pressure, which is typical in lab-scale experiments (Boaretto et al., 2021). The battery also showed promising results regarding the energy density when run in a stacked configuration without extra pressure or heat (Lee et al., 2020).

Criterion II stated that the battery cell should "be reasonably well suited for large scale production". To evaluate that, some common obstacles for large scale production were examined. According to Boaretto et al. (2021), one such challenge is to find an electrolyte that has multiple important characteristics and at the same time are easy to manufacture. It is difficult to obtain an electrolyte with desirable performance without energy intensive and high temperature processing. Many SEs also require dry room conditions for most of the processes as they are unstable in moisture. One promising sulfide SE is the argyrodite, which has the benefit of being softer than many other SEs (Yu et al., 2021). This reduces the need for energy intensive production steps, such as high temperature sintering (Boaretto et al., 2021).

Criterion III required that the battery cell should be realistic for use in future EV applications. Two key factors for batteries aimed for EV applications are: (i) the ability to work with high effects (Oh et al., 2022) and (ii) a high specific energy, which translates to range in the EV use phase (Zackrisson, 2021). As previously mentioned, sulfide-type SEs provide the highest ionic conductivities and lithium-ion transference numbers of the SE families, which is connected to the cyclability at high effects (Li et al., 2021). As for the specific energy, the anode-free design used in the argyrodite battery cell shows great promise for high specific energies (Heubner et al., 2021). The design of the argyrodite battery cell also looks very similar to the "ideal SSB cell design" as presented by Albertus et al. (2021). The energy capacity for the argyrodite battery cell in a dual stacked configuration (which is the configuration studied) was reported to be 2.4 Wh in the supplemental information of Lee et al. (2020). While the exact weight of the stacked pouch cell was not given in the study by Lee et al. (2020), the geometrical calculations made in this study (details in Appendix B) puts the weight at 6.282 grams, leading to a specific energy of 383 Wh/kg. While this does not reach the specified target for EV-batteries of 450 Wh/kg set by EUCAR (2019), the specific energy for a battery cell adapted for EV application is expected to be much higher since it would consist of many layers of stacked components in the same pouch. Increasing the stack numbers can improve the energy density (Lee et al., 2020), making the argyrodite more viable for EV applications.

Criterion IV stated that the battery cell should use a SE that contained few critical and/or rare elements. Many of the SEs showing promise, such as LGPS and LLZO, usually contain rare or critical elements, including germanium, lanthanum, and tantalum(CRM alliance., n.d). The argyrodite-type sulfide used in the chosen battery cell is one of the few that are showing great promise (Li et al., 2021) without containing a mixture of scarce elements, as those previously mentioned. One could make an argument for lithium being a potentially problematic element. However, since lithium is included in most comparable SEs (Varsi et al., 2020), choosing an argyrodite-based battery cell still was deemed to be one of the best choices. One reason for concern from a material rarity perspective for the argyrodite battery cell is the use of silver in the separator layer, being among the rarer metals in the earth's crust.

3.3 System function and functional unit

As the function of a battery cell is to store energy, the functional unit in this study was set to 1 kWh of theoretical storage capacity produced. Using 1 kWh as a functional unit in LCA studies of batteries has been recommended by Porzio and Scown (2021). It also enables comparability to other LCA studies of batteries (Arshad et al., 2022) and could, if necessary, be recalculated to express the results using another functional unit.

3.4 System boundaries

To fulfill the goal of the LCA, reasonable system boundaries need to be set (Baumann and Tillman 2004). In the following sections, an initial flowchart of the studied system is presented and boundaries for geography, time and technological system are defined.

3.4.1 System under study

The system boundaries of this study were set to include the cradle-to-gate environmental impacts of the studied argyrodite battery cell as shown in Figure 3.2. The cradle represents extraction of substances from the environment, and the gate represents the product leaving the production facility. Authors like Zackrisson (2021) recommend that batteries intended for EV applications should always include a use phase. However, including the use and end-of-life phases is difficult for prospective LCAs, as details of these life-cycle stages are often lacking

at the early development stage (Thonemann et al., 2020). This was the case for the studied argyrodite battery cell, as both the exact applications and recycling pathways are unknown. Furthermore, the cradle-to-gate scope is used in many previously made LCA studies of SSB cells (Lastoskie and Dai, 2015; Troy et al., 2016; Keshavarzmohammadian et al., 2018; Smith et al., 202; Zhang et al., 2022), leading to increased comparability with those studies.

All processes within the foreground system were assumed to take place in a factory equal in size and production capacity to the scaled-up LIB cell factory modeled by Chordia et al. (2021). Specifically, this means that the factory was assumed to cover 150 000 m^2, operate 7900 hours/year and produce batteries with a total capacity of 16 GWh annually. The factory was assumed to only produce the argyrodite battery cell.

The processes included in the intermediate and the background system were assumed to take place outside of the battery factory. The production of precursor materials was modeled in a simplified manner without allocation, and all their impacts are considered part of the battery cell manufacturing. This can also be referred to as the "main product bears all burden" approach (Sandin et al., 2015).

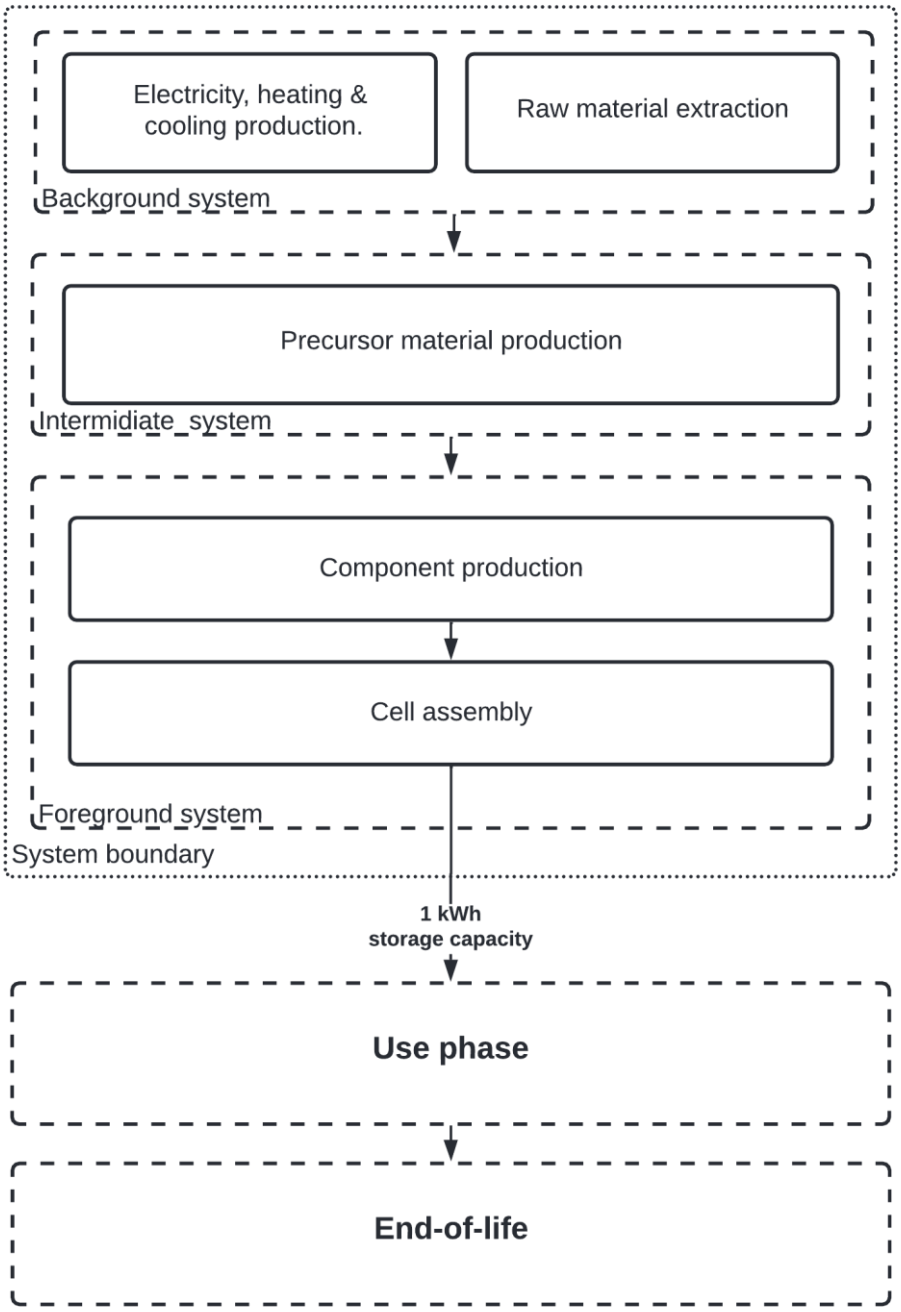

Figure 3.2: *Initial flowchart showing the life cycle stages within and without the system boundary.*

3.4.2 Geographical system boundary

As there are many potential locations for a future battery factory, its location was undefined in this study. The sourcing of raw materials was assumed to be done globally. As the location is unspecified, it influences the energy mix used for manufacturing and the distance of transporting raw materials. In this study, transportation of raw materials within the background system were included, based on the average data and default values from the database Ecoinvent v3.8, where most of the transportation data has already been included (Spielmann et al., 2007). The preferred data provider was global datasets, but if not available in Ecoinvent v3.8, Europe or Rest of World datasets were used in that priority.

3.4.3 Temporal system boundary

The purpose of the study was to assess the environmental impacts of the argyrodite battery cell at a point in time where the manufacturing has reached large scale. No exact year for this is defined, since it is difficult to foresee the exact time scale due to the rapid research and development in the battery field (Ma et al., 2021). Even though the exact time was undefined, the future scope of the study means that the data collected need to be scaled up and positioned at a future point in time to adhere to the aim of the study. The scaling of the background data was mainly be based on a framework by Piccinno et al. (2016), and the foreground on the gigafactory model by Chordia et al., (2021). Scaling is further discussed in Section 3.6

3.4.4 Technological boundary

In this study, the foreground system included the assembly of the argyrodite battery cell, as well as production of the electrolyte, NMC 811 cathode and Ag-C separator layer. The foreground system also consisted of the final pouch cell assembly. The energy and raw materials were, however, supplied from the background system, and the supply of auxiliary materials from an intermediate system. As the study was prospective, finding relevant and accessible data was difficult, both for the foreground and background processes. The LCI data for the argyrodite battery cell was only available at lab-scale and finding fully disclosed information were not possible for all process steps. This means that the assessment had to rely on data from similar manufacturing methods, process calculations, expert judgements, other LCA studies, the scientific literature and LCI databases.

Excluded from the study were transports within the foreground system, as they were assumed to be negligible, consisting of short distances within the manufacturing site.

3.5 Scenarios

The modeling of the production at the hypothetical factory was based on scenario ranges, creating one optimistic scenario and one pessimistic scenario. The parameters used to build the scenarios were the manufacturing methods of silver nanoparticles (AgNPs) and carbon nanofibers (CNF), solvent recirculation rates, and differently carbon-intensive energy supply. The scenario modeling choices are summarized in Table 3.1.

Regarding the energy used in the processes, the optimistic scenario was built with a Swedish energy mix, consisting mainly of low-carbon sources (renewables and nuclear power) (IEA, 2022), and the pessimistic with a South Korean energy mix. South Korea was chosen for the pessimistic scenario as many battery cell manufacturers are currently located in South Korea (Chordia et al., 2021), and the South Korean energy mix consists mainly of fossil fuels (Lutsey et al., 2018), creating a more carbon-intensive scenario.

Solvent recirculation was not used at the lab-scale production but was mentioned by Piccinno et al. (2016) as a possibility for scaled up manufacturing. In this study, a 95% solvent recirculation was included in the optimistic scenario, while in the pessimistic scenario, a 50% solvent recirculation was included.

According to a comparative LCA of AgNPs by Temizel-Sekeryan and Hicks (2020), AgNPs have a variety of production methods. In this study, two of the manufacturing methods from that study were chosen. The methods chosen were reactive magnetron sputtering (RMS) and arch plasma (AP) due to their capacity to produce the required size range of the particles and because they were mentioned as suitable for the desired area of application. For the optimistic scenario, the reactive magnetron sputtering was chosen since the results of the study by Temiziel-Sekeryan and Hicks (2020) showed that this method performs better than the AP method from an environmental point of view, which was in turn considered in the pessimistic scenario. These methods are described in Appendix A3.2.

The CNF can also be produced by different manufacturing processes. The manufacturing methods chosen were based on a study by Khanna et al. (2008), who compared energy and environmental impacts between different carbon feedstocks. In this study, the optimistic scenario considered benzene as feedstock, and the pessimistic scenario considered methane. This choice was based on the worst and best life-cycle impact results from Khanna et al. (2008).

Table 3.1: *Summary of the modeled scenarios*

Optimistic	Pessimistic
• Swedish energy mix • AgNPs manufactured with the reactive magnetron sputtering (RMS) method • CNF manufactured from benzene feedstock • Solvent recirculation at 95%	• South Korean energy mix • AgNPs manufactured with the arc plasma (AP) method • CNF manufactured from methane feedstock • Solvent recirculation at 50%

3.6 Scaling

The foreground system modeling considered the lab-scale prototype manufacturing described by Lee et al. (2020) as a starting point. However, to fulfill the aim of the study, which was to assess the impacts of the SSB cell at a future state when it has reached large-scale manufacturing, the model was adjusted in multiple ways to account for the differences that occur between lab scale and large scale.

For the foreground modeling, the overarching scaling strategy was to assume that the manufacturing of the argyrodite battery cell is similar to scaled up LIB cell manufacturing, using a modeling developed by Chordia et al (2021) as baseline. The motivation behind this choice is that Boaretto et al. (2021) mentioned that there is potential for producing SSB cell components using production lines similar to LIB cells. The techniques mentioned are especially viable for sulfide-type SE, such as the argyrodite type battery cell (Boaretto et al., 2021), see Section 3.2. The foreground system was, however, not modeled identically to the scaled-up LIB cell manufacturing, but adjusted based on interviews with experts and the work by Schnell et al. (2018). Adaptations of the modeling include increasing the dry room requirement notably and choosing production methods considered viable for scaled up production of sulfur-based SSB cells.

The foreground system scaling was also based on a framework by Piccinno et al. (2016) for energy requirement calculations. The framework was used for the energy requirement approximations for most of the foreground and intermediate processes (see detailed energy calculations in Appendix C). The recommendation of the framework on solvent recirculation were also followed. Solvent assumptions are described in detail in Section 4.3.

For the scaling of background data in this prospective LCA, worst- and best-case scenarios were used, as predictive scenarios are only relevant when a likely development is known (Arvidsson et al., 2017). Since the geography was undefined in this study, it opened the possibility to use different countries' electricity, heating and cooling production data as the ranges. The best-case scenario was approximated by using slightly modified data on Swedish electricity, heating and cooling production (heavy in hydro and nuclear power) from the Ecoinvent 3.8 database. The worst-case scenario was approximated by using unmodified Ecoinvent data for the South Korean energy mix.

3.7 Impact categories

Regarding the impact categories, midpoint characterization was chosen for this study as it is commonly used (Peter et al., 2017) and as it reduces uncertainty compared to using endpoint LCIA methods (Baumann and Tillman, 2004; Thonemann et al., 2020). Most characterization factors were from the ReCiPe hierarchist midpoint indicator method, but were complemented with two other methods to achieve full coverage of the aim. The choice of ReCiPe as LCIA method was motivated by it being one of the more common methods used in LCAs of battery cells (Peters et al., 2017; Arshad et al., 2022) and was also used in other prospective LCAs of battery cells (Lastoskie and Dai, 2015; Smith et al., 2021; Chordia et al., 2021). The hierarchist version of the ReCiPe method was chosen as it is considered the default perspective and is most often used in scientific models (Huijbregts et al., 2017).

The ReCiPe hierarchist midpoint includes 18 midpoint indicators (RIVM., 2011). According to Gasafi et al. (2003), uncertain data in early design stages makes it difficult to cover all impact categories for emerging technologies. Furthermore, according to Arvidsson et al. (2017), a limited number of categories can be enough to

assess environmental impacts of emerging technologies, since midpoint indicators such as climate change often correlate strongly with other indicators. The chosen impact categories are summarized below in Table 3.2.

From the ReCiPe hierarchist midpoint method, the impact categories climate change, terrestrial acidification, water use, and mineral resource depletion were chosen. Climate change and terrestrial acidification are commonly used impact categories in battery cell LCAs (Peters et al., 2017; Arshad et al., 2022), and are recommended to include when studying for EV batteries from a life-cycle perspective (Zackrisson., 2021). The category of water use was also included, in an attempt to identify water-specific hotspots.

Energy consumption is another commonly included impact category in LCA studies of batteries (Peters et al., 2017). The ReCiPe method lacks impact categories covering energy consumption, so instead the cumulative energy demand (CED) method was included in the study. The CED method differentiates energy harvested from different energy sources (Frischknecht et al., 2015). For this study, energy from all sources were combined to into one value for the total cumulative energy.

For this study and also for battery technologies in general, mineral resource depletion is an important impact category, since batteries typically contain several rare and/or scarce minerals (Zackrisson, 2021; Porzio and Scown, 2021). To cover this impact category well, the indicator surplus ore potential (SOP) from the ReCiPe method was combined with another indicator for assessing the same category, namely a newly developed method by Arvidsson et al. (2020) called the crustal scarcity indicator (CSI).

The SOP indicator assesses the amount of extra ore required when an additional unit of resource is extracted (Vieira et al., 2017). The SOP indicator includes parameters such as ore grade and commodity prices, and hence the results can vary over time. This means that the results become time sensitive, but they give an idea about short-term mineral resource depletion. The SOP indicator is, however, not optimal for assessing long-term mineral resource depletion (Arvidsson et al., 2020a; Porzio and Scown, 2021). Therefore, for this study, the SOP indicator was complemented with the CSI. The CSI uses a characterization factor called crustal scarcity potential (CSP), which are based on crustal concentrations of minerals. This indicator decouples mineral resource depletion from supply and demand dynamics pertaining to extraction rates and prices, making it suitable for assessing long-term mineral scarcity impacts (Arvidsson et al., 2020b).

***Table 3.2**: Chosen impact categories, characterization factors and units.*

Impact category	LCIA method	Characterization factor	Unit
Climate change	ReCiPe midpoint (H)	GWP	kg CO_2 eq
Terrestrial Acidification	ReCiPe midpoint (H)	AP	kg SO_2 eq
Water use	ReCiPe midpoint (H)	WCP	m^3
Resource depletion, Energy	CED	-	MJ
Resource depletion, Mineral	ReCiPe midpoint (H)	SOP	kg Cu eq
Resource depletion, Mineral	CSI	CSP	kg Si eq

Previous LCA studies of SSB cells also included human toxicity and/or ecotoxicity as impact categories (Lastoskie and Dai, 2015; Troy et al., 2016; Keshavarzmohammadian et al., 2018; Smith et al., 2021; Zhang et al., 2022). However, there exists a discussion about whether toxicity is covered well enough by current LCIA methods. Zackrisson (2021) claims that characterization factors for toxicity and data on life cycle emissions of toxic substances currently is lacking. Instead, Zackrisson (2021) suggests complementing LCA studies with a chemical risk assessment to handle toxicity impacts. For this reason, no toxicity impact categories were included in this study.

3.8 Sensitivity analysis

In a prospective LCA, data uncertainty is inevitable as the life cycle phases are uncertain and there is limited availability of data to represent the technology at every step of the product life cycle. In this study, a sensitivity analysis was therefore performed. Two parameters were considered due to presumed large influence and/or

uncertainties in the assumptions. The energy demand for dry rooms has in previously conducted LCAs been pointed out as an environmental hotspot for sulfide-based SSB cell (Schnell et al., 2018; Keshavarzmohammadian et al., 2018). Combined with the uncertainty regarding the dry room assumptions, the dry room requirement was tested in the sensitivity analysis.

One of the key parameters in the chosen argyrodite battery cell is silver, used to achieve the performance of the cell. Silver, belonging to the precious metal group, occurs in relatively low concentrations in the earth's crust, which is why the sustainability of using silver may be questioned. In an article by Yang et al. (2019), a similar battery chemistry as the Ag-C separator layer system was presented, where magnesium was used to form a lithium–manganese alloy anode. Magnesium would be a good substitution from a resource point of view as it is abundant in the lithosphere (Seetharaman et al., 2020). As silver was assumed likely to contribute considerably to the mineral resource depletion, the replacement of silver with magnesium was tested in the sensitivity analysis.

3.9 Comparison

To be able to put the results of this study into context and answer RQ2, three results from the impact assessment step were compared with results from previously conducted LCA studies of other batteries. The impact categories chosen for comparison were climate change and mineral resource depletion. Climate change was chosen since it is a representative overall emission indicator, and the most commonly presented impact category in LCAs of EVs (Nordelöf et al., 2014). It is also mentioned in previous studies that environmental impacts correlate to each other (Arvidsson et al., 2017) and it was therefore concluded enough to compare one impact category related to environmental emissions. Climate change was compared across all the studies presented in Table 3.3. The SOP and CSI indicators were chosen due to mineral resource depletion being a focus of this study, and the two indicators represent mineral scarcity in a short- and long term, respectively. The SOP and CSI indicators were compared with Chordia et al. (2021), as the only battery cell study that could be found using both indicators.

Efforts were made to find comparative studies that were recent, covered multiple battery types and used a cradle-to-gate system boundary. The results are graphically represented and qualitatively discussed in Section 6.1. A summary of the LCAs chosen for comparison is presented in Table 3.3.

As can be seen in Table 3.3, the studies apply different background databases and LCIA methods, both of which have an influence on the results of the study. Lopez et al. (2021) and Iturrondobeitia et al. (2021) are review articles summarizing results from several LCAs. Average values from these reviews were compared to the results of this study. The studies also used different functional units, and in those cases the results were recalculated to the functional unit 1 kWh of theoretical storage capacity produced.

Table 3.3: *Summary of studies for comparison of results.*

Study	Battery type	LCIA method	Background database
This study	Argyrodite SSB	ReCiPe, CED, CSI	Ecoinvent 3.8, patens, literature
Chordia et al. (2021)	LIB	ReCiPe, CSI	Ecoinvent 3.7
Iturrondobeitia et al. (2021)	LIB	Multiple	Several
Lopez et al. (2021)	Li-S battery	CML-baseline	Ecoinvent 3.6
Keshavarzmohammadian et al. (2018)	Pyrite SSB	TRACI	US-EI 2.2
Smith et al. (2020)	LLZO SSB	ReCiPe	Literature & lab data
Troy et al. (2016)	LCO/LLC SSB	ILCD	Ecoinvent 2.2

3.10 Modeling software

The LCA model was constructed in OpenLCA V1.11 developed by GreenDelta. This is an open-source software offering modeling of life cycle systems, connection with databases and the possibility to calculate environmental impacts with a variety of different LCIA methods (openLCA, 2022).

4. Inventory analysis

This section provides a more in-depth overview of the modeled system and summarized inventory result for the argyrodite battery cell. Furthermore, it contains an in-depth discussion about two key assumptions of the model: solvent and dry room usage.

4.1 The system model

The studied system includes a foreground system that encompasses the main production processes assumed to be within the factory, an intermediate system producing auxiliary components and a background system that includes production of electricity, heat and cooling as well as extraction of raw material.

The foreground processes include production of three main battery cell components: a catholyte sheet, a pressed electrolyte sheet and an Ag-C separator layer. The foreground system also includes the final assembly of the pouch cell and processes representing the building and operation of the factory. The modeling of the pouch cell and its components were calculated using the cell geometry as presented by Lee et al. (2020). Detailed inventory results and process descriptions can be found in Appendix A, mass calculations in Appendix B and process energy calculations in Appendix C. An overview of the system within the system boundary is presented in Figure 4.1 In the subsequent sections, a summary of the inventory data and key assumptions regarding solvent use and dry rooms are discussed.

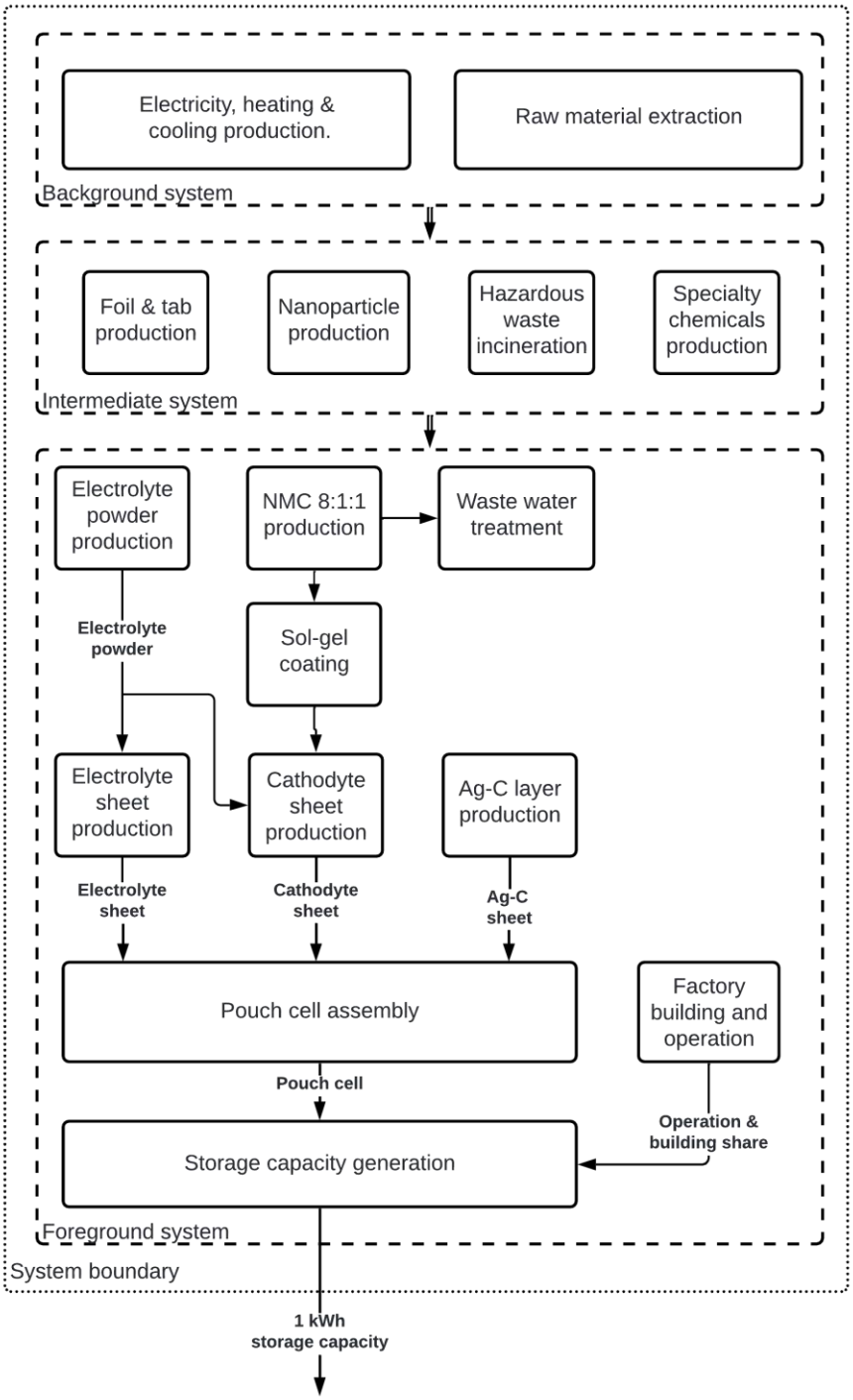

Figure 4.1: *Detailed flowchart of the modelled system.*

4.2 Input materials

Table 4.1 summarizes the bill of materials of the argyrodite battery cell components, both for the production of one pouch cell and the storage capacity of 1 kWh. The weights of the argyrodite battery cell components were largely calculated from geometric information given by Lee et al. (2020) combined with densities from Ullmans encyclopedia of industrial chemistry. Detailed references for each component can be found in Appendix B. According to the geometric calculations, the mass of one pouch cell in a bi-layered configuration was 6.3 g. To achieve a storage capacity of 1 kWh, 415 pouch cells are required as one pouch cell has a capacity of 2.4 Wh

according to the supplementary information from Lee et al. (2020). Detailed inventory modeling results for each process can be found in Appendix A.

The geometrical calculations show that the main component of the argyrodite battery cell is the catholyte sheet, compromising 44% of the total battery cell by weight. The contribution of the electrolyte sheet and Ag-C separator layer to the total weight are comparably small, with 8% and 5%, respectively. The rest of the cell consists of auxiliary components required for the functioning of the battery, such as the laminate bag used as a container to pack the battery, the current collectors, and the tabs.

Table 4.1: *Mass inventory results for one pouch cell and one functional unit (1kWh).*

Component	Mass/pouch cell [g]	Mass/kWh [g]	Share [w%]
Active cathode material	2.26	939	36.0
Catholyte sheet (excl. active cathode material)	0.52	216	8.2
Electrolyte sheet	0.516	214	8.2
Ag-C separator layer	0.336	140	5.4
Laminate bag	1.31	544	20.8
Nickel tab	0.356	148	5.7
Aluminum foil & tab	0.205	169	3.3
Stainless steel foil	0.782	325	12.4
Total	**6.28**	**2611**	**100**

4.3 Solvent assumptions

The exact solvent input was only given for a few of the processes stated in Lee et al. (2020). For those processes, in accordance with the framework by Piccinno et al. (2016), an assumption was that in industrial-scale production, a reduction of 20% could be achieved. For the remaining processes where the solvent amount was unknown, proxy data from solvent use in similar studies were examined. Slurry-creating processes from Ellingsen et al. (2014), Liang et al. (2017), Keshavarzmohammadian et al. (2018) and Zhang et al. (2022) showed that solvents constituted 35-55% of the total weight of the slurries. Based on that, an assumption was made that the slurry processes for the studied model would require solvents equal to the dry weight of the components, which is close to the upper value of the identified range.

According to Piccinno et al. (2016), recirculation of solvents is another possibility at industrial-scale production. Recirculation would reduce the input of solvent, but at the cost of some additional water and energy consumed in the recirculation process. In this study, recirculation of solvents was assumed for all solvent-using processes within the factory. While the gigafactory in Chordia et al. (2021) assumed a 99% solvent recirculation rate, this study explored a recirculation of 95% in the optimistic scenario and 50% in the pessimistic scenario. For the share of solvents not recirculated, incineration was assumed. The energy and water consumed in the recycling process of the solvents were modeled according to the template energy cost for distillation as given by Capello et al. (2005), which is recommended by Piccinno et al. (2016) when no measured data is available.

Furthermore, it was also assumed that in the recirculation process, a small fraction of the solvents would be emitted to air in the form of non-methane volatile organic compound (NMVOC), calculated as emissions to the air. These losses were assumed to be 1% of the solvents, which corresponds to the values used by Chordia et al. (2021). The 1% emitted to the air was, however, neglected in the calculation of quantitative solvent use and recirculation due to its negligible magnitude.

4.4 Dry room

Previous studies of life-cycle impacts of SSB cell manufacturing have identified energy for dry-room operation as an environmental hotspot and driver of costs (Smith et al., 2021; Keshavarzmohammadian et al., 2018). This may be especially concerning for batteries containing a sulfur SE, as they heavily depend on dry rooms for the manufacturing (Schnell et al., 2018), due to their tendency to react with both lithium metal and moisture in the atmosphere (Varzi et al., 2020). For the argyrodite battery cell, Lee et al. (2020) only state which processes were performed in dry rooms (dew point below -50°C), not the energy requirement or share of the total energy that the dry rooms require. Therefore, the modeling of dry rooms was based on a bottom-up approach inspired by the work of Deng et al. (2017). In their study, Deng et al. (2017) modeled an industrial-sized dry room intended for sulfur battery cell manufacturing.

The approach taken in this study were to extract the power requirement per surface area reported in Deng et al. (2017) and then scale it to the studied SSB cell production. Due to the lack of disclosed information in Lee et al. (2020), this was done based on assumptions about how much of the factory area needs to be dry room. In the lab-scale argyrodite battery cell by Lee et al. (2020), the majority of the processes in the manufacturing were performed in a glovebox with argon atmosphere conditions. The only processes performed outside of the glovebox in the prototype battery cell were the isostatic pressing in the pouch cell assembly and the production of the Ag-C separator layer. This is in line with findings from Schnell et al. (2018), who explore differences between the current LIB cell manufacturing and future hypothetical production of sulfide-based SSB cell. Furthermore, an assumption was also made regarding the operation time of the factory. This was done based on the operating time of the gigafactory as modeled by Chordia et al. (2021). Based on those findings, combined with the fact that most of the component production at the lab-scale were conducted in argon atmosphere, an assumption was made that dry rooms would cover 75% of the factory area. Furthermore, it was assumed that these would be running the entire time that the factory is operating. Different degrees of dry room coverage were also tested in the sensitivity analysis in Section 6.3. Details of the dry room energy calculations can be found in Appendix C.5.

5. Impact assessment

This section provides the results of the LCIA of the argyrodite battery cell. In the interest of keeping the impact results succinct and digestible, emphasis is put on the climate change and mineral resource depletion impact categories.

5.1 Climate change

The climate change results for the prospective LCA showed that the optimistic scenario would generate about 57 kg of CO_2 eq/kWh, most of which are related to production of input materials. The pessimistic scenario result showed an almost doubling of the impacts, resulting in 115 kg CO_2 eq/kWh. The results are graphically presented in Figure 5.1.

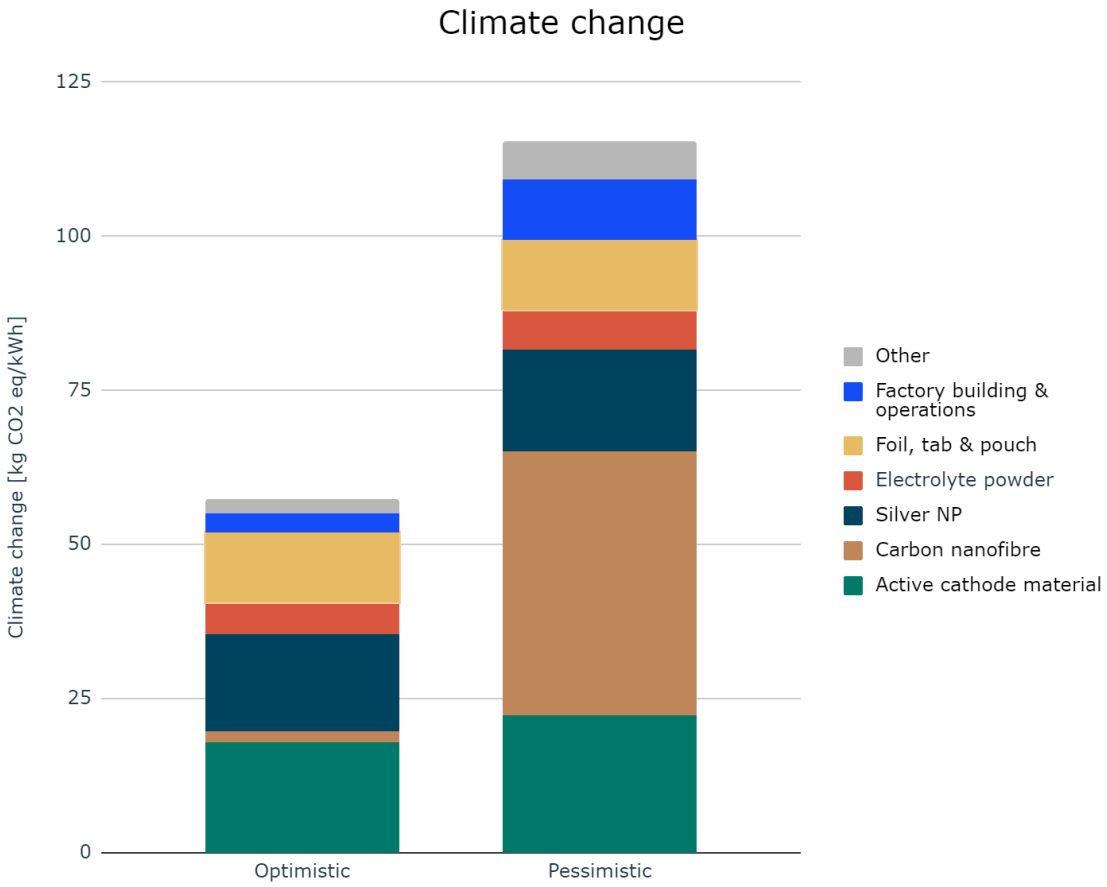

Figure 5.1: *Climate change results for optimistic and pessimistic scenario. The categories refer to the production of each component/input.*

The components in the optimistic scenario that contributed the most to the climate change impact were the active cathode material (31%), the AgNPs (27%) and the foil, tabs, and pouch (20%). In the pessimistic scenario, the most contributing components were the CNFs (37%), the active cathode material (19%) and the AgNPs (14%).

When comparing the two scenarios, there were two components that had noticeable increasing impact. Firstly, there was a dramatic increase in the contribution from CNFs. This increase came from a combination of a fourfold increase of electricity required when using the pessimistic (methane) feedstock and the fossil fuel heavy South Korean energy mix. Secondly, there was a significant but less dramatic increase in impacts from the factory

building and operations, which notably includes the operation of the dry rooms. The increased impacts from that category stemmed exclusively from the change in energy mix, as the amount of energy required for the process remained the same between the scenarios.

5.2 Terrestrial acidification

Terrestrial acidification impacts were 0.67 kg SO_2 eq/kWh in the optimistic scenario and 0.96 kg SO_2 eq/kWh in the pessimistic scenario. The increase in impact between the scenarios can be attributed mainly to increased acidification from the electricity production in the South Korean energy mix. The production pathways of AgNPs and CNFs were also more energy intensive in the pessimistic scenario, which further amplified the difference between the scenarios.

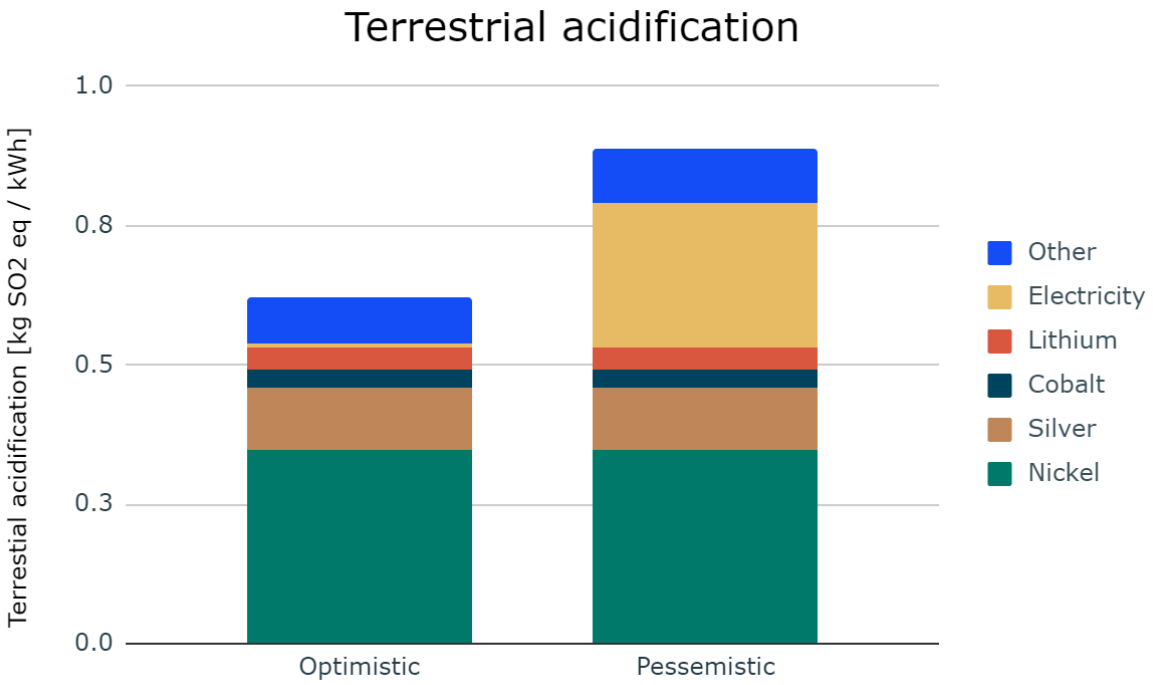

Figure 5.2: *Terrestrial acidification results. The categories refer to the extraction & refinement of each element.*

The impact results showed that the extraction and refinement of nickel and silver were clear hotspots in both scenarios. Around 67% of the nickel in the argyrodite battery cell were used in the active cathode material, and the rest were used for the nickel tabs. In a real use-case, it is likely that the impacts from the tabs would be significantly reduced since a battery cell would only use a single nickel tab for discharging instead of many stacked pouch cells which were the way it was modeled in this study.

Extraction and refinement of silver also seems to be a potential hotspot. The silver contributed with 18% of the impacts for the optimistic scenario and 13% for the pessimistic scenario. The lower share of silver impacts in the pessimistic scenario stemmed from a higher total impact, not a reduction of impact from silver itself.

For the pessimistic scenario, the electricity production contributed to 29% of the acidification impacts, making it a clear hotspot. In the optimistic scenario, the impact contribution from electricity were only 1%. This showed that the acidification impacts are greatly affected by the energy mix.

5.3 Cumulative energy demand

As a complement to the climate change and terrestrial acidification categories, cumulative energy demand was examined. The cumulative energy demand represented the total amount of electricity, heating, and cooling used for the argyrodite battery cell production. The energy demand in the optimistic scenario was about 1680 MJ/kWh and for the pessimistic scenario it was about 2660 MJ/kWh. These numbers are in line with findings

from the review of 19 LCA studies by Peters et al. (2017), which showed an average cumulative energy demand of about 1180 MJ/kWh for LIB cells with different active cathode materials.

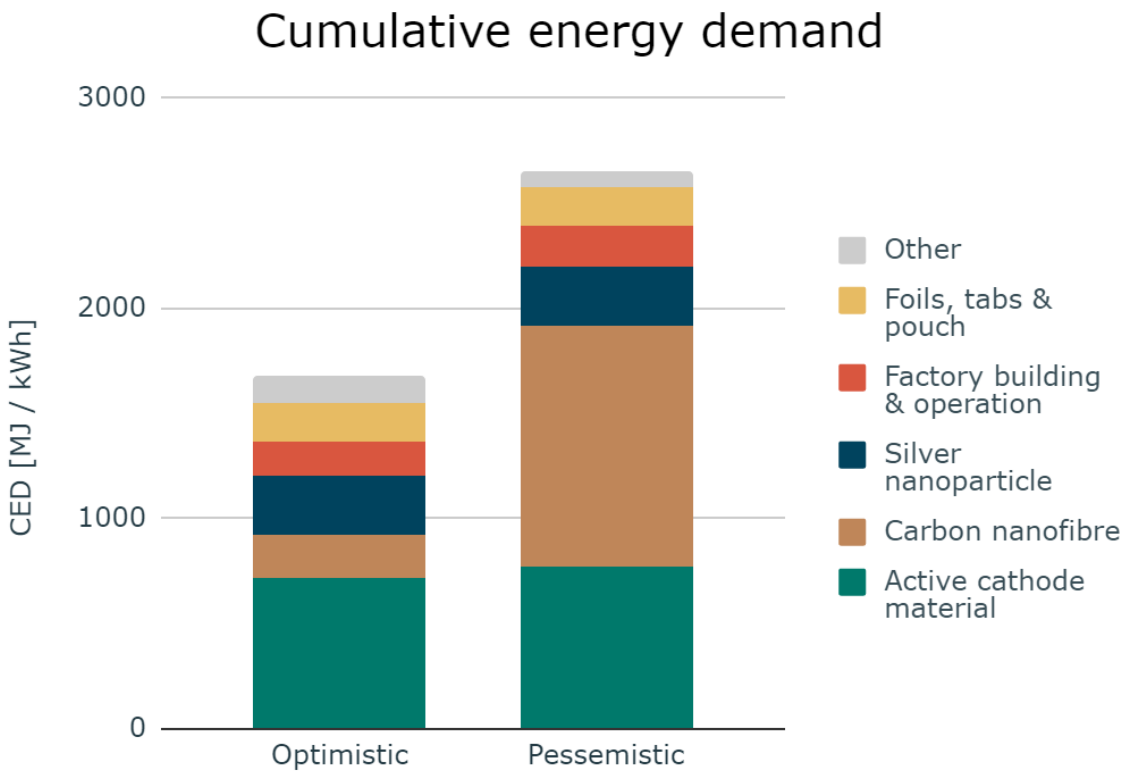

Figure 5.3: *Cumulative energy demand results. The categories refer to the production of each component.*

The component that contributed most to the cumulative energy demand was the active cathode material (42% in the optimistic scenario, 29% in the pessimistic). In the pessimistic scenario, the production of the CNFs also contributed with a large (43%) share of the cumulative energy demand. This was due to the use of the pessimistic (methane) feedstock, which roughly quadrupled the energy required in production.

5.4 Water use

The impact results for water use mainly reflected water used in the background system, as modelling of water consumption for the foreground system processes was not detailed. In the optimistic scenario, the impact result was 3.6 m^3/kWh, and in the pessimistic scenario, it was 4.9 m^3/kWh.

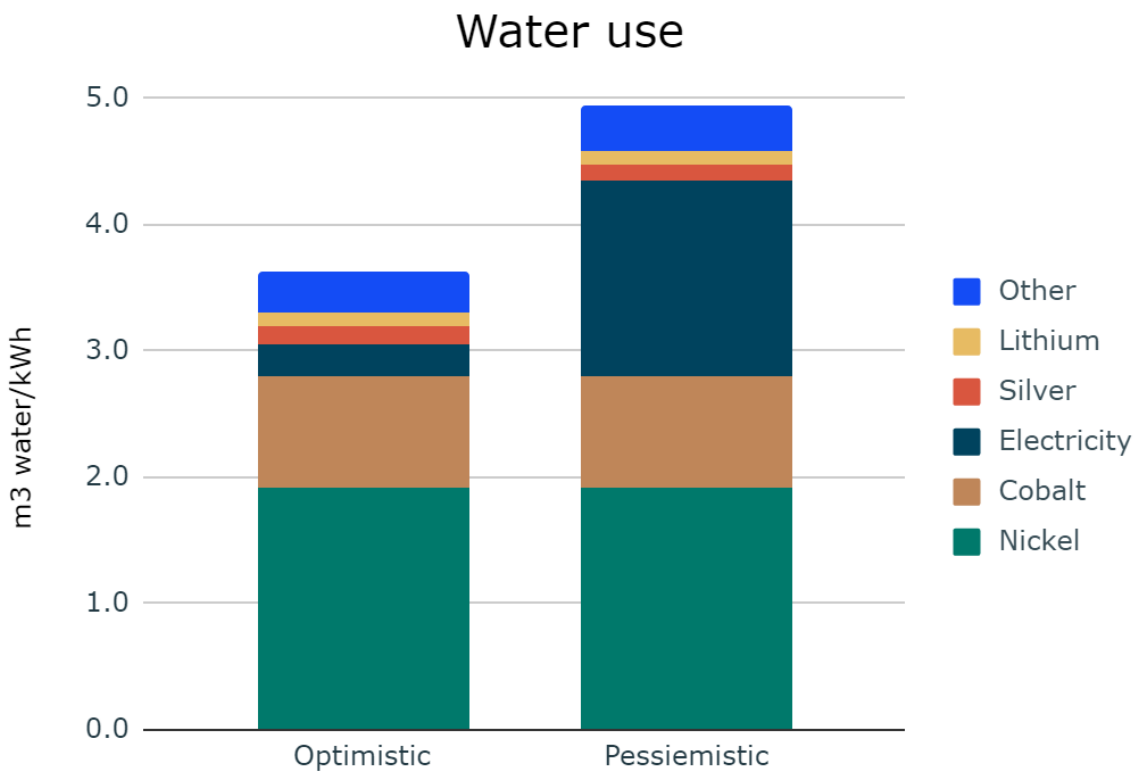

Figure 5.4: *Water usage impact results. The categories refer to the extraction & refinement of each element.*

The main contributor to the water use impact was the extraction and refinement of nickel and cobalt. Nickel production contributed with 53% of the impact in the optimistic scenario and 39% in the pessimistic. Cobalt production contributed with 24% in the optimistic scenario and 18% in the pessimistic. In the pessimistic scenario, electricity production contributed significantly more than in the optimistic scenario; 31% in the pessimistic compared to 7% in the optimistic. The increase in water use impact from electricity accounts for almost all of the difference between the scenarios.

5.5 Mineral resource depletion

The mineral resource depletion impact was evaluated using two indicators: the CSI by Arvidsson et al. (2020a), which assesses global long-term mineral resource depletion impacts, and the SOP from ReCiPe midpoint package to assess short-term mineral resource depletion impact. The difference in results between the optimistic and pessimistic scenarios were less than 5% for both indicators. This indicated that the contribution to the mineral resource depletion impact from the energy mix was small, hence most impacts are instead attributed to material choices for the battery cell. Therefore, only the results for the optimistic scenario were shown in Figure 5.5.

The total result for the CSI indicator for the argyrodite battery cell is about 7300 kg Si eq/kWh and for the SOP indicator about 6.6 kg Cu eq/kWh. As shown in Figure 5.5, there is a notable difference in the contribution of each element depending on the indicator used.

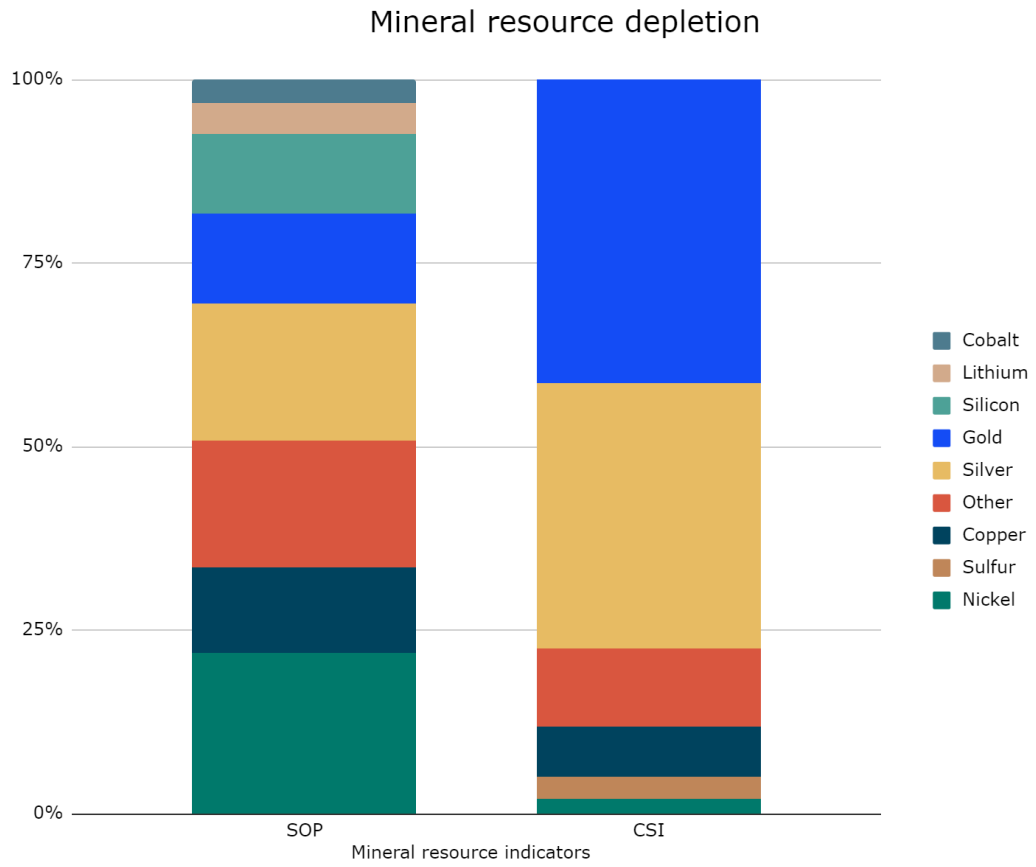

Figure 5.5: *Mineral resource depletion impact results for the optimistic scenario, presented as normalized contributions from elementary flows. SOP=surplus ore potential, CSI=crustal scarcity indicator.*

Unexpectedly, an element that had the largest impact on the CSI, and a notable contributor to the SOP indicator, was gold, an element which was not even included among the battery cell materials. The reason for this was that the Ecoinvent process used for the silver extraction and refining was a multiple-output process, in which both silver and gold were included. The process used an economic allocation, and thus a small amount of gold was allocated to the flow of silver. The impacts from gold and silver combined contributed with a total of about 71% of the CSI and about 31% of the SOP.

There were also a few other high contributing elements, such as nickel, copper and silicon. Nickel contributed about 21% of the impact for the SOP indicator, but only about 2% in the CSI indicator. Copper contributed about 12% of the mineral resource depletion impacts with the SOP indicator and about 7% for the CSI. Silicon notably contributed about 11% of the mineral resource depletion impact for the SOP indicator but negligibly to the CSI, since silicon is among the most common elements in the earth's crust. Some elements lacked impact factors for the SOP indicator, e.g. sulfur, which contributed 3% of the impacts for the CSI.

6. Interpretation

As can be seen in Figure 2.1 in Section 2, the interpretation step is not performed sequentially last, but rather continuously throughout the work. In this section, however, the results of the impact assessment are interpreted with a comparison to other battery cell LCAs, where focus is on the results of climate change and mineral resource depletion. Further, the uncertainties in the results are discussed and lastly the sensitivity analysis is presented.

6.1 Comparison

To put the results of this study into context and answer parts of RQ2, a comparison with similar LCA studies and review articles were made. A summary of the studies included in the comparison are found in Table 3.3 in Section 3.9.

Figure 6.1 shows the climate change impacts of the argyrodite battery cell. When compared with other battery cells, the climate change impact of the battery seems to perform rather well. The impact was similar to those of the LIB assessed in Chordias et al. (2021), and the result for the optimistic scenario in this study was very similar to the average values for LIB cells from Iturrondobeitia et al. (2021). The impact for the pessimistic scenario was similar to the variants of the Li-S battery cell review by Lopez et al. (2021). Compared to the other sulfide battery cells presented by Keshavarzmohammadian et al. (2018) and Smith et al. (2021), the argyrodite battery cell performs better. An important difference between the argyrodite battery cell in this study and the SSB cell studied by Keshavarzmohammadian et al. (2018) and Smith et al. (2021) was that the other studies did not model a large-scale production as in this study. The impact results were therefore difficult to compare as they were presented for different production scales. For the climate change impacts, the energy usage was the largest contributor in both studies, which is often assumed to be reduced at large-scale production.

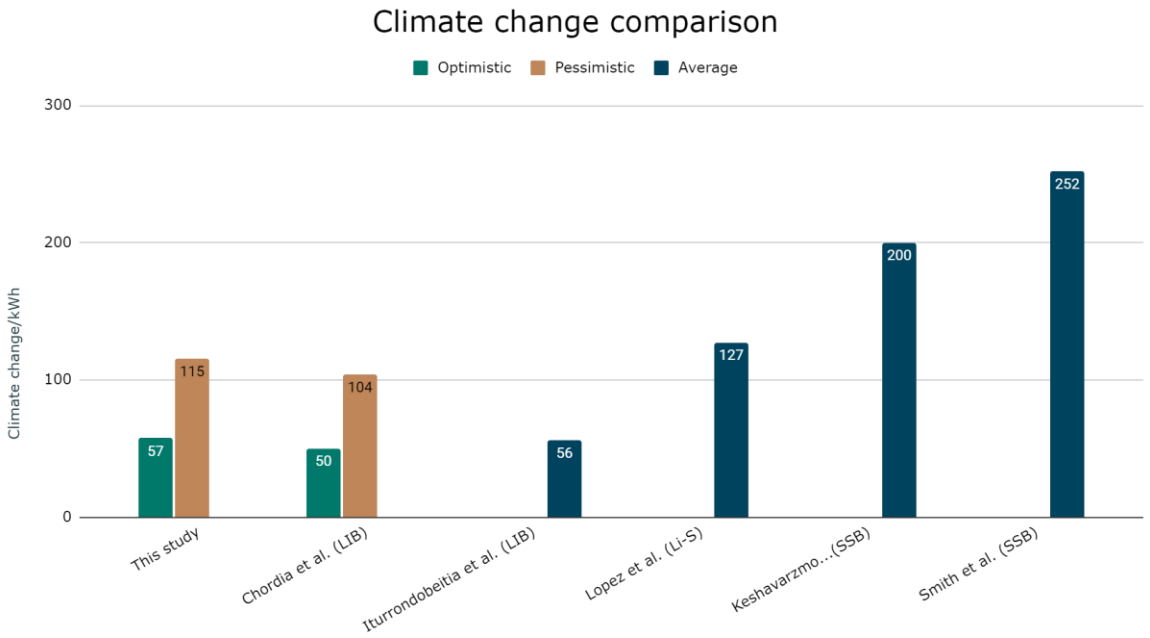

Figure 6.1: *Comparison between the climate change impact results of this study and five other studies.*

One SSB cell study that did model scaled up production was the one by Troy et al. (2016), which is not included in Figure 6.1. This was because even with scaling, their result showed a climate change impact as high as 1045 kg CO_2 eq/kWh, a full order of magnitude higher than the results from this study. While it remains unclear why the results from Troy et al. (2016) were that much higher than those of the other studies, in their model, most of the climate change impact came from their dry room and an energy intensive tape-casting process. Troy et al. (2016) mentioned that their energy requirements of their battery cell production step was highly uncertain. They

especially pointed out that the energy required for the heat treatments were conservatively estimated, and that optimizing these energy intensive processes have great potential to drastically reduce the impacts.

The mineral resource depletion results were compared with the study by Chordia et al. (2021). Further comparisons with other studies were not possible as mineral resource depletion was not assessed in any other studies.

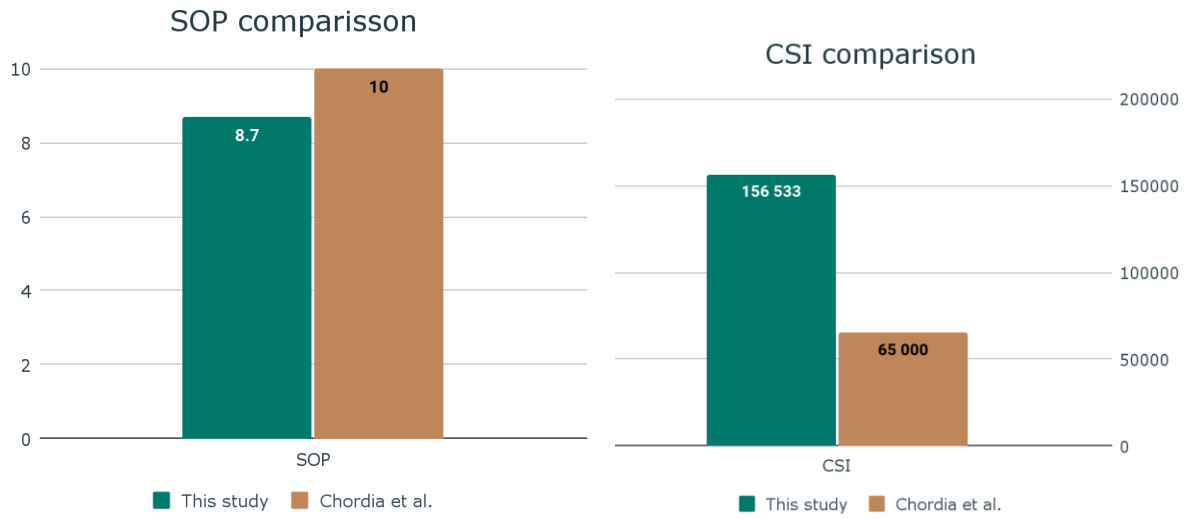

Figure 6.2: *Comparison of the SOP (left, unit: kg Cu eq/kWh) and CSI (right, unit: kg Si eq/kWh) indicators.*

The argyrodite battery cell performed similar to the LIB cell for the SOP indicator, but worse for the CSI indicator, seen in Figure 6.2. This similar result in the SOP category could be explained by the fact that while the batteries use the same active cathode materials (which contribute most of the SOP impacts), the argyrodite battery cell studied in this work has a higher energy density due to the electrolyte and the anode-free design. This difference is, however, partly negated by the use of silver; otherwise, the difference would have been greater.

Chordia et al. (2021) showed that in their study, the CSI results consisted mainly of the active cathode materials and the copper foil. The argyrodite battery cell also contains the same active cathode material, but the largest contribution by far was the use of silver, which explains the difference between the batteries.

6.2 Uncertainties

Due to confidentiality issues, no exact bill-of-materials for the studied prototype battery cell could be obtained. Instead, this information needed to be derived from geometrical information and material densities. Many parts of the manufacturing system design and production also needed to be based on literature data and assumptions. To make the uncertainties explicit in accordance with the framework from Gavankar et al. (2015), some key parameters are be discussed below.

The material requirements for the prototype battery cell were modeled based on geometric calculations, hence the commercialized battery cell may contain different ratios of input materials. The geometric information provided by Lee et al. (2020) were, however, quite detailed and using Ullmans encyclopedia of industrial chemistry as source for material densities was seen as a reliable source. Furthermore, for all processes in the foreground and intermediate system that were modeled based on patents or previous LCAs, a 100% yield was assumed. Also, losses due to cutting of the component sheets in the assembly phase were neglected. This is also a source of uncertainty since production pathways without losses are unrealistic. This means that quantities used, and impacts caused by the materials might be higher than estimated in this study. This might particularly affect the CSI and SOP indicators due to the large influence that a reduced yield of AgNPs would have.

A hotspot for climate change with considerable uncertainties was the CNF production. The LCI data were obtained from Khanna et al. (2008), who model CNF production from different feedstocks, but with an old production method (Yadav et al., 2020). Several developments have happened in the field of nanoparticle

manufacturing since the time of their assumptions, and further developments are likely to happen in the future (Yadav et al. 2020). This means that at the point in time when the studied SSB cell is likely to be industrially produced, CNFs will most likely be produced via more efficient pathways (Yadav et al., 2020). However, conducting forecasts of future production of CNFs was deemed too time consuming to be included in the scope of this study. As an alternative way to partially address this uncertainty, LCI data from the most optimistic and the most pessimistic feedstocks from Khanna et al. (2008) were used in the two considered scenarios.

Since the description of the prototype battery cell manufacturing (Lee et al., 2020) in almost all cases only provided a ratio of solvents used and not the absolute quantities, these were instead assumed based on LCI data from studies modeling similar manufacturing. In this model, much due to assumptions regarding solvent recirculation, the use of solvent has a small influence on the results. However, if the solvent use would be considerably higher than estimated in this study, this could influence the results, in particular climate change.

Another source of uncertainty connected to the scaling comes from the used framework by Piccinno et al. (2016). The framework is one of the first attempts at estimating future impacts using lab-scale data. Furthermore, it was developed primarily for wet-chemical production processes, which means it might not be completely suitable for some of the processes in this study e.g. grinding, heating and solvent recirculation. Since the alternative would be to either not scale certain processes at all or use multiple frameworks (which could add further uncertainty), using the Piccinno et al. (2016) framework was seen as the better option.

A process step described as an environmental hotspot in SSB cell manufacturing is the densification step needed to create a good interfacial stability between components (Boaretto et al., 2021). In this study, this process was modeled to be performed by a warm isostatic press rocess based on proxy data from a study on densification of steel powder from Azevedo et al. (2017). This is likely uncertain and would require further examination.

Another part of a sulfur-based SSB cell manufacturing that has been pointed to as an environmental hotspot by Schnell et al. (2018), Keshavarzmohammadian et al. (2018) and Boaretto et al. (2021) is the dry room. The dry room modeling in this study was based on proxy data from Deng et al. (2017) together with assumptions on how large area the dry rooms needed to cover, how much time they operate per year and the throughput of materials. The exact energy requirement for the dry room would also vary depending on where in the world the factory operated, since colder or warmer climates would affect the energy requirements of dry rooms. To partly address the uncertainties in the dry-room modeling, one of the dry-room factors was tested in the sensitivity analysis in Section 6.3

6.3 Sensitivity analysis

In an effort to test the robustness of the LCA model, two factors were chosen for the sensitivity analysis. As previously mentioned, uncertainties regarding the use of silver and the dry room requirements might have a large impact on the final results of the study and were therefore tested in the sensitivity analysis.

6.3.1 Dry room coverage effects on climate change

In previous studies, dry room usage has been identified as an environmental hot spot for sulfide-based SSB cell manufacturing (Schnell et al., 2018; Keshavarzmohammadian et al., 2018). In this study, the dry room did not seem to be a major issue considering the impact results, but to challenge that notion this sensitivity analysis was performed. Details on the dry room modeling can be found in Section 4.4 and Appendix C5. The sensitivity analysis examines the influence on climate change from varying the share of the factory surface that was covered by dry room between 0 and 100% (75% was used in the original model). The climate change results were compared with the results from the pessimistic scenario since the differences in the impacts from energy usage was expected to vary the most with a fossil fuel-based energy mix.

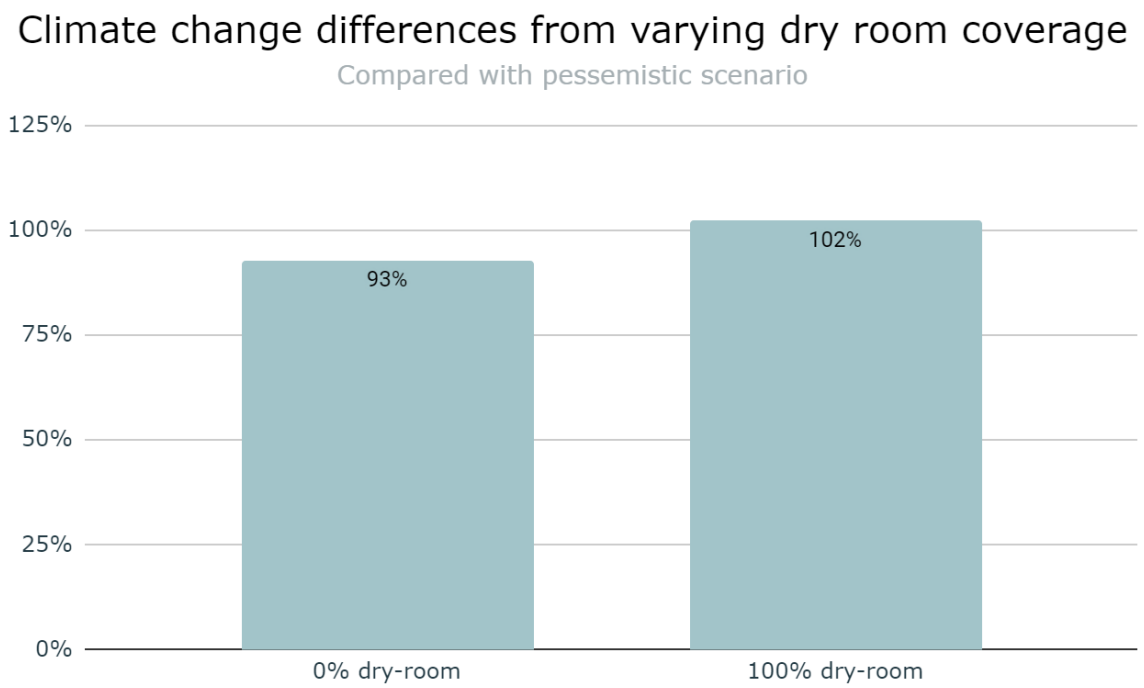

Figure 6.3: *Influenc on climate change impacts from varying the dry-room coverage.*

The analysis showed that removing the dry room all together would reduce the climate change impact with only 7% and covering the whole factory would increase it by only 2%. This result indicates that the model this study was based on is not sensitive to changes in dry room energy.

6.3.2 Substitution of Ag with Mg

The single largest contributor to the mineral resource depletion indicators was the use of silver for the Ag-C separator layer. Silver is not only a rare material, but both the extraction of raw materials as well as the impacts from refinement of the nanoparticles generate high greenhouse gas emissions that contributes considerably to climate change. There is ongoing research about substituting silver in SSBs with other materials. One such substitution that has shown promise is using magnesium instead of silver and the feasibility of this has been proved by Yang et al. (2019). Figure 6.4 shows the effect of this substitution on climate change, the CSI and the SOP. The results are compared with the results from the pessimistic scenario.

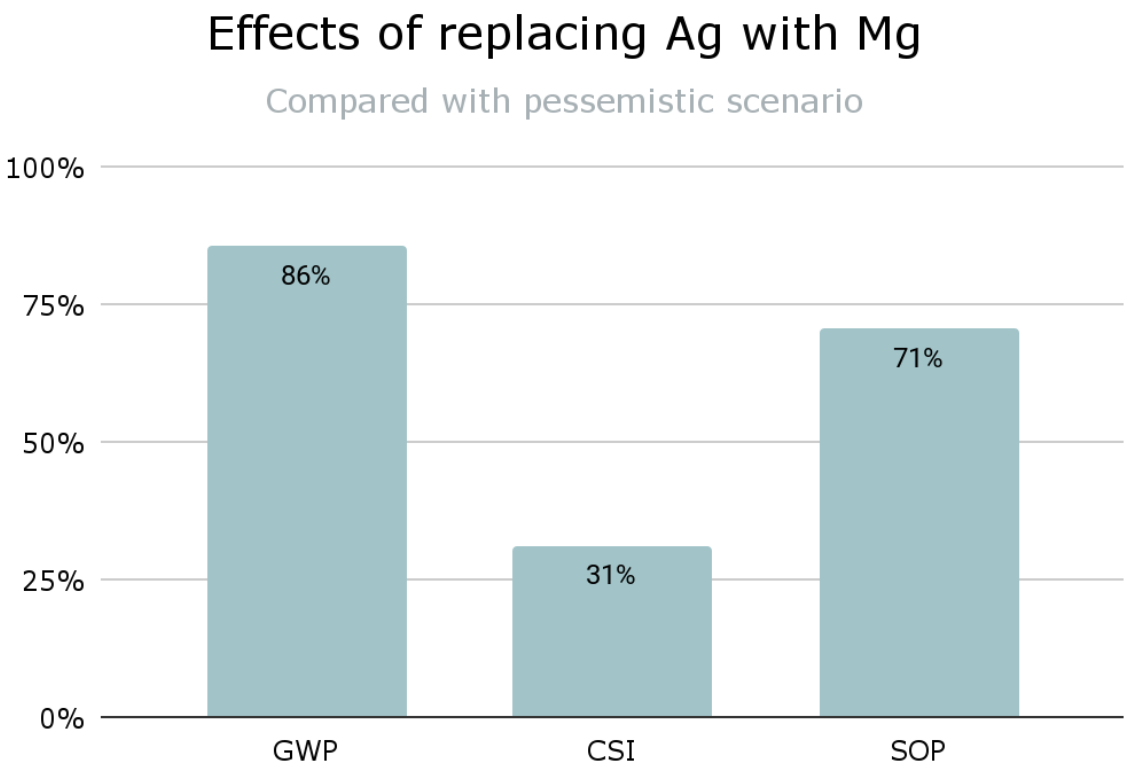

***Figure 6.4**: Effects on climate change and mineral resource depletion impacts when replacing silver (Ag) with magnesium (Mg).*

This result showed that substituting silver would result in a 14% reduction in climate change, 69% reduction for the CSI and a 29% reduction in SOP. This means that if such a substitution is realized, it would drastically improve the long-term resource impact. It also showed that the results of the study are in general highly sensitive to the silver requirement.

7. Conclusions

This study aimed at performing a pre-study to identify a promising SSB cell that had not yet been studied from a life-cycle perspective. Furthermore, the aim was to assess the environmental impacts of manufacturing this battery cell at a point in time where it has reached large-scale production. The methodology used for estimation of the environmental impacts was a cradle-to-gate prospective LCA with the functional unit of 1 kWh of theoretical storage capacity produced.

The pre-study concluded that there are several promising SSB cell designs, but the one chosen was an anode-free argyrodite SSB cell with a Ag-C nanoparticle layer to promote even lithium plating when charged. The battery cell design utilized a high energy density NMC 811 cathode and showed promising lab-scale results for energy density and cyclability. The battery cell was chosen as it was described as an important breakthrough in several SSB cell review articles due to its upscaling potential and high technical performance. Lastly, a brief survey of published LCA studies showed that no argyrodite-type SSB cell had been previously studied from a life-cycle perspective, making the argyrodite battery cell a relevant candidate for the LCA.

The prospective LCA concluded that argyrodite batteries produced at a factory with an annual production capacity of 16 GWh would have a similar climate change impact per kWh as LIB cells produced at the same scale. Furthermore, the argyrodite battery cell performed slightly better than Li-S battery cells and other SSB cells regarding climate change, although methodological differences make comparisons challenging.

The components contributing the most to the GHG emissions were CNFs, AgNPs and the active cathode material. The CNF manufacturing seems to be an extra critical hotspot due to an energy-intensive production route. If the CNF manufacturing uses energy from fossil fuel-heavy sources, the total emissions for the battery cell increases considerably. Hence, the recommendation is to make attempts at using a more energy efficient production route for the CNF and to use low-carbon energy sources.

Regarding terrestrial acidification, the only significant difference between the optimistic and the pessimistic scenario came from the electricity production. A notable acidification hotspot was the nickel mining, which contributed 56% of the acidification in the optimistic scenario and 39% in the pessimistic scenario.

In the mineral resource depletion category, the results varied depending on the indicator used. Assessed with the SOP indicator, the argyrodite battery cell showed a similar impact as an LIB cell produced at the same scale. But when assessed with the CSI indicator, the impacts of the argyrodite were more than twice those of the LIB cell. Silver was the biggest contributor for both indicators, although in the CSI it was completely dominant. The conclusion of this is that unless the silver can be substituted or reliably recycled, this battery cell might be unsuitable for upscaled sustainable production. The sensitivity analysis showed that if the silver could be substituted by magnesium (which is reportedly feasible), the climate change impacts could be reduced by 14%, the SOP with 29% and the CSI with a total of 69%.

The two most important improvements for the argyrodite battery cell would thus be to find more efficient production pathways for CNF and to substitute the silver.

References

Aetna Plastic Corp, n.d.. *DuPont™ Teflon® PTFE Specifications.* [Online] Available at: https://www.aetnaplastics.com/site_media/media/attachments/aetna_product_aetnaproduct/25/PTFE%20Specifications.pdf [Accessed 5 mars 2022]

Albemarle, 2018. *Lithium Methoxide, typ. 10 % solution in Methanol (typ. 2.2 M).* [Data set] Available at: https://www.albemarle.com/products/lithium-methoxide-typ-10-solution-in-methanol-typ-22-m [Accessed 30 may 2022]

Albertus, P., Anandan, V., Ban, C., Balsara, N., Belharouak, I., Buettner-Garrett, J., Chen, Z., Daniel, C., Doeff, M., Dudney, N.J., Dunn, B., Harris, S.J., Herle, S., Herbert, E., Kalnaus, S., Libera, J.A., Lu, D., Martin, S., McCloskey, B.D., McDowell, M.T., Meng, Y.S., Nanda, J., Sakamoto, J., Self, E.C., Tepavcevic, S., Wachsman, E., Wang, C., Westover, A.S., Xiao, J., Yersak, T., 2021. Challenges for and Pathways toward Li-Metal-Based All-Solid-State Batteries. *ACS Energy Lett*ers, 6, 1399–1404. https://doi.org/10.1021/acsenergylett.1c00445

Althaus, H. J., Chudacoff, M., Hischer, R., Jungbluth, N., Osses, M., Primas, A., 2007. *Life cycle inventory of chemicals.* [PDF] Ecoinvent report no. 8, v2.0. EMPA Dübendorf, Swiss centre for life cycle inventories, Dübendorf, CH. Available at: https://db.ecoinvent.org/reports/08_Chemicals.pdf [Accessed 24 Mars 2022]

An, Y., Han, X., Liu, Y., Azhar, A., Na, J., Nanjundan, A.K., Wang, S., Yu, J., Yamauchi, Y., 2022. Progress in Solid Polymer Electrolytes for Lithium-Ion Batteries and Beyond. *Small,* 18, 2103617. https://doi.org/10.1002/smll.202103617

Arshad, F., Lin, J., Manurkar, N., Fan, E., Ahmad, A., Tariq, M.-N., Wu, F., Li, L., 2022. Life Cycle Assessment of Lithium-ion Batteries: A Critical Review. *Resources, Conservation and Recycling,* 106164. https://doi.org/10.1016/j.resconrec.2022.106164

Arvidsson, R., Tillman, A.-M., Sandén, B.A., Janssen, M., Nordelöf, A., Kushnir, D., Molander, S., 2017. *Environmental assessment of emerging technologies: recommendations for prospective LCA. Journal of Industrial Ecology*, 22, 1286–1294. https://doi.org/10.1111/jiec.12690

Arvidsson, R., Söderman, M.L., Sandén, B.A., Nordelöf, A., André, H., Tillman, A.-M., 2020a. A crustal scarcity indicator for long-term global elemental resource assessment in LCA. *International Journal of Life Cycle Assessment,* 25, 1805–1817. https://doi.org/10.1007/s11367-020-01781-1

Arvidsson, R., Chordia, M., Wickerts, S., Nordelöf, A., 2020b. Implementation of the crustal scarcity indicator into life cycle assessment software. *Chalmers university of technology, Department of technology management and economics.* Report No. 2020:05

Azevedo, J.M.C., CabreraSerrenho, A., Allwood, J.M., 2017. Energy and material efficiency of steel powder metallurgy. *Powder Technology,* 328, 329–336. https://doi.org/10.1016/j.powtec.2018.01.009

Baumann, H., Tillman, A. M., 2004. *The hitch hikers guide to LCA: An orientation in life cycle assessment methodology and application.* 1:7 ed. Lund: Studentlitteratur.

Benabed, Y., Rioux, M., Rousselot, S., Hautier, G., Dollé, M., 2021. Assessing the Electrochemical Stability Window of NASICON-Type Solid Electrolytes. *Frontiers in Energy Research*, 9, 682008.

Bettermann, G., Krause, W., Riess, G., Hofmann, T., 2000. *Phosphorus Compounds, Inorganic in: Ullmann's Encyclopedia of Industrial Chemistry*, John Wiley & Sons, Ltd. https://doi.org/10.1002/14356007.a19_527

Boaretto, N., Garbayo, I., Valiyaveettil-SobhanRaj, S., Quintela, A., Li, C., Casas-Cabanas, M., Aguesse, F., 2021. Lithium solid-state batteries: State-of-the-art and challenges for materials, interfaces and processing. *Journal of Power Sources,* 502, 229919. https://doi.org/10.1016/j.jpowsour.2021.229919

Bonnick, P., Muldoon, J., 2022. The quest for the holy grail of solid-state lithium batteries. *Energy & Environmental Science*, 15, 1840-1860 https://doi.org/10.1039/D2EE00842D

Britannica, The Editors of Encyclopedia, 2020. *Silver.* [Online] Available at: https://www.britannica.com/science/silver [Accessed 13 may 2022]

Burchardt, B.R., Merz, P.W., 2006. Chapter 6 - Elastic Bonding and Sealing in Industry, in: Cognard, P. (Ed.), Adhesives and Sealants, *Handbook of Adhesives and Sealants*, Elsevier Science Ltd, pp. 355–xlii. https://doi.org/10.1016/S1874-5695(06)80017-5

Burton, D., Lake, P., Palmer, A., n.d. *Carbon Nanofiber Applications & Properties.* [Online] Available at: https://www.sigmaaldrich.com/SE/en/technical-documents/technical-article/materials-science-and-engineering/batteries-supercapacitors-and-fuel-cells/carbon-nanofibers [Accessed 5 mars 2022]

Buyle, M., Audenaert, A., , P., Boonen, K., Van Passel, S., 2019. The Future of Ex-Ante LCA? Lessons Learned and Practical Recommendations. *Sustainability*, 11, 5456. https://doi.org/10.3390/su11195456

Caduff, M., Huijbregts, M.A., Althaus, H.-J., Hendriks, A.J., 2011. Power-law relationships for estimating mass, fuel consumption and costs of energy conversion equipment. *Environmental Science & Technology,* 45, 751–754.

Capello, C., Hellweg, S., Badertscher, B., Hungerbühler, K., 2005. Life-Cycle Inventory of Waste Solvent Distillation: Statistical Analysis of Empirical Data. *Environmental Science & Technol*ogy, 39, 5885–5892. https://doi.org/10.1021/es048114o

Celik, I., Hosseinian Ahangharnejhad, R., Song, Z., Heben, M., Apul, D., 2020. Emerging Photovoltaic (PV) Materials for a Low Carbon Economy. *Energies,* 13, 4131. https://doi.org/10.3390/en13164131

Chalmers, 2021. *Life cycle assessment of future battery chemistries – high storage capacity without scarce resources?.* [online] Available at: https://www.chalmers.se/en/projects/Pages/Life-cycle-assessment-of-future-battery-chemistries-Q-high.aspx [Accessed 20 january 2022].

Chemeurope, n.d. *Phosphourus pentasulfide.* [Online] Available at: https://www.chemeurope.com/en/encyclopedia/Phosphorus_pentasulfide.html?msclkid=49265cffa91611ec890bf38cac40ceea [Accessed 5 May 2022]

Cheng, Z., Zahiri, B., Ji, X., Chen, C., Chalise, D., Braun, P.V., Cahill, D.G., 2021. Good Solid-State Electrolytes Have Low, Glass-Like Thermal Conductivity. *Small,* 17, 2101693. https://doi.org/10.1002/smll.202101693

Chordia, M., Nordelöf, A., Ellingsen, L.A.-W., 2021. Environmental life cycle implications of upscaling lithium-ion battery production. *International Journal of Life Cycle Assessment*, 26, 2024–2039. https://doi.org/10.1007/s11367-021-01976-0

Chu, L., Sheng, L., Yang, X., Wenkui, Z., Hui, H., Xinyong, T., Yongping, G., WIPO (PCT). 2015. *Preparation method of lithium sulfide powder.* Google patents. WO2016119481A1. Available at: https://patents.google.com/patent/WO2016119481A1/en

Collingridge, D., 1982. *The social control of technology.* Frances Pinter St. Martin's press, London New York.

CRM Alliance, n.d. *Germanium.* [Online] Available at: https://www.crmalliance.eu/germanium [Accessed 5 may 2022]

Cucurachi, S., Giesen, C. van der, Guinée, J., 2018. Ex-ante LCA of Emerging Technologies. *Procedia CIRP*, 69, 463–468. https://doi.org/10.1016/j.procir.2017.11.005

Deng, Y., Li, J., Li, T., Gao, X., Yuan, C., 2017. Life cycle assessment of lithium sulfur battery for electric vehicles. *Journal of Power Sources*, 343, 284–295. https://doi.org/10.1016/j.jpowsour.2017.01.036

Ecoinvent, n.d. *System models*. [Online] Available at: https://ecoinvent.org/the-ecoinvent-database/system-models/ [Accessed 24 may 2022]

Edström, K., Dominko, R., Fichtner, M., Perraud, S., 2020. Battery 2030+ Roadmap. https://doi.org/10.33063/diva2-1452023

Ellingsen, L.A.-W., Majeau-Bettez, G., Singh, B., Srivastava, A.K., Valøen, L.O., Strømman, A.H., 2014. Life Cycle Assessment of a Lithium-Ion Battery Vehicle Pack. *Journal of Industrial Ecology*, 18, 113–124. https://doi.org/10.1111/jiec.12072

Estes, L.L., Schweizer, M., 2011. Fibers, 4. *Polyamide Fibers, in: Ullmann's Encyclopedia of Industrial Chemistry*, John Wiley & Sons, Ltd. https://doi.org/10.1002/14356007.a10_567.pub2

EUCAR (European Council for Automotive R&D), 2019. *Battery requirements for future automotive applications EG BEV&FCEV*. [PDF] Available at: https://eucar.be/wp-content/uploads/2019/08/20190710-EG-BEV-FCEV-Battery-requirements-FINAL.pdf. [Accessed 8 mars 2022]

Fan, L., Wei, S., Li, S., Li, Q., Lu, Y., 2018. Recent Progress of the Solid-State Electrolytes for High-Energy Metal-Based Batteries. *Advanced Energy Materials*, 8, 1702657. https://doi.org/10.1002/aenm.201702657

Fazeni, K., Lindorfer, J., Prammer, H., 2014. Methodological advancements in life cycle process design: a preliminary outlook. *Resources, Conservation and Recycling*, 92, 66–77.

Flexicon, n.d. *Carbon Black*. [Online] Available at: https://www.flexicon.com/Materials-Handled/Carbonblack.html#:~:text=In%20appearance%2C%20carbon%20black%20may%20be%20an%20intensely,1.8-2.1%20g%2Fcm%203%20and%20a%20high%20surface-area-to-volume%20ratio. [Accessed 8 mars 2022]

Foroozan, T., Sharifi-Asl, S., Shahbazian-Yassar, R., 2020. Mechanistic understanding of Li dendrites growth by in- situ/operando imaging techniques. *Journal of Power Sources*, 461, 228135. https://doi.org/10.1016/j.jpowsour.2020.228135

Frischknecht, R., Wyss, F., Büsser Knöpfel, S., Lützkendorf, T., Balouktsi, M., 2015. Cumulative energy demand in LCA: the energy harvested approach. *International Journal of Life Cycle Assessment*, 20, 957–969. https://doi.org/10.1007/s11367-015-0897-4

Gasafi, E., Meyer, L., Schebek, L., 2003. Using Life-Cycle Assessment in Process Design. *Journal of Industrial Ecology*, 7, 75–91. https://doi.org/10.1162/108819803323059415

Gavankar, S., Anderson, S., Keller, A.A., 2015. Critical components of uncertainty communication in life cycle assessments of emerging technologies: nanotechnology as a case study. *Journal of Industrial Ecology*, 19, 468–479. https://doi.org/10.1111/jiec.12183

Gracia, I., Armand, M., Shanmukaraj, D., 2019. Li Metal Polymer Batteries, in: Murugan, R., Weppner, W. (Eds.), Solid Electrolytes for Advanced Applications: Garnets and Competitors. *Springer International Publishing*, Cham, pp. 347–373. https://doi.org/10.1007/978-3-030-31581-8_15

Guinée, J.B., Cucurachi, S., Henriksson, P.J.G., Heijungs, R., 2018. Digesting the alphabet soup of LCA. *International Journal of Life Cycle Assessment*, 23, 1507–1511. https://doi.org/10.1007/s11367-018-1478-0

Hauschild, M. and M. A. J., Huijbregts. 2015. Introducing Life Cycle Impact Assessment. *In Life Cycle Impact Assessment*, edited by M. Hauschild and M. A. J. Huijbregts. Dordrecht: Springer. https://doi.org/10.1007/978-94-017-9744-3_1

Herle, S., Chen, Z., Libera, J., Tepavcevic, S., Anandan, V., Yersak, T., McDowell, M., Martin, S., Doeff, M., Harris, S., Herbert, E., Belharouak, I., Daniel, C., Dudney, N., Kalnaus, S., Nanda, J., Self, E., Westover, A., Lu, D., Xiao, J., Buettner-Garrett, J., Ban, C., Balsara, N., McCloskey, B., Dunn, B., Meng, S., Albertus, P., Wachsman, E., Wang, C., Sakamoto, J., 2020. *Challenges for and Pathways Toward Solid-State Batteries.* Oak Ridge: Oak Ridge National Laboratory. https://doi.org/10.2172/1731043

Heubner, C., Maletti, S., Auer, H., Hüttl, J., Voigt, K., Lohrberg, O., Nikolowski, K., Partsch, M., Michaelis, A., 2021. From Lithium-Metal toward Anode-Free Solid-State Batteries: Current Developments, Issues, and Challenges. *Advanced Functional Materials*, 31, 2106608. https://doi.org/10.1002/adfm.202106608

Hippauf, F., Schumm, B., Doerfler, S., Althues, H., Fujiki, S., Shiratsuchi, T., Tsujimura, T., Aihara, Y., Kaskel, S., 2019. Overcoming binder limitations of sheet-type solid-state cathodes using a solvent-free dry-film approach. *Energy Storage Materials*, 21, 390–398. https://doi.org/10.1016/j.ensm.2019.05.033

Huang, Y., Shao, B., Han, F., 2022. Li alloy anodes for high-rate and high-areal-capacity solid-statebatteries. *Journal of Material Chemistry* A, https://doi.org/10.1039/D2TA02339C

Huijbregts, M.A., Steinmann, Z.J., Elshout, P.M., Stam, G., Verones, F., Vieira, M., Zijp, M., Hollander, A., van Zelm, R., 2017. ReCiPe2016: a harmonised life cycle impact assessment method at midpoint and endpoint level. *International Journal of Life Cycle Assessment*, 22, 138–147. https://doi.org/10.1007/s11367-016-1246-y

IEA, 2021. *Global EV Outlook 2021.* [Online] Available at: https://www.iea.org/reports/global-ev-outlook-2021 [Accessed 24 may 2022]

IEA, 2022. *Sweden.* [Online] Available at: https://www.iea.org/countries/sweden [Accessed 14 june 2022]

INEOS, n.d. *Typical Engineering Properties of Polypropylene.* [Online] Available at: https://www.ineos.com/ [Accesses 10 mars 2022]

International Organization for Standardization, 2006. *ISO 14040:2006 Environmental management - Life cycle assessment - Principles and framework - Requirements with guidance for use.* [Online] ISO. Available at: https://www.iso.org/standard/37456.html [Accessed 20 january 2022].

IPCC, 2022. *Summary for Policymakers. In: Climate Change 2022: Mitigation of Climate Change.* Contribution of Working Group III to the Sixth Assessment Report of the Intergovernmental Panel on Climate Change [P.R. Shukla, J. Skea, R. Slade, A. Al Khourdajie, R. van Diemen, D. McCollum, M. Pathak, S. Some, P. Vyas, R. Fradera, M. Belkacemi, A. Hasija, G. Lisboa, S. Luz, J. Malley, (eds.)]. Cambridge University Press, Cambridge, UK and New York, NY, USA. Available at: https://www.ipcc.ch/report/ar6/wg3/downloads/report/IPCC_AR6_WGIII_SPM.pdf [Accessed 20 april 2022]

Islam, M.A., Jacob, M.V., Antunes, E., 2021. A critical review on silver nanoparticles: From synthesis and applications to its mitigation through low-cost adsorption by biochar. *Journal of Environmental Management*, 281, 111918. https://doi.org/10.1016/j.jenvman.2020.111918

Ito, S., Fujiki, S., Yamada, T., Aihara, Y., Park, Y., Kim, T.Y., Baek, S.-W., Lee, J.-M., Doo, S., Machida, N., 2014. A rocking chair type all-solid-state lithium-ion battery adopting Li2O–ZrO2 coated LiNi0.8Co0.15Al0.05O2 and a sulfide based electrolyte. *Journal of Power Sources*, 248, 943–950. https://doi.org/10.1016/j.jpowsour.2013.10.005

Iturrondobeitia, M., Akizu-Gardoki, O., Minguez, R., Lizundia, E., 2021. Environmental Impact Analysis of Aprotic Li–O2 Batteries Based on Life Cycle Assessment. *ACS Sustainable Chemistry & Engineering*, 9, 7139–7153. https://doi.org/10.1021/acssuschemeng.1c01554

Kamienski, C.W., McDonald, D.P., Stark, M.W., Papcun, J.R., 2004. Lithium and Lithium Compounds, in: Kirk-Othmer Encyclopedia of Chemical Technology. *John Wiley & Sons, Ltd.* https://doi.org/10.1002/0471238961.1209200811011309.a01.pub2

Keshavarzmohammadian, A., Cook, S.M., Milford, J.B., 2018. Cradle-to-gate environmental impacts of sulfur-based solid-state lithium batteries for electric vehicle applications. *Journal of Cleaner Production,* 202, 770–778. https://doi.org/10.1016/j.jclepro.2018.08.168

Khanna, V., Bakshi, B.R., Lee, L.J., 2008. Carbon Nanofiber Production. *Journal of Industrial Ecology,* 12, 394–410. https://doi.org/10.1111/j.1530-9290.2008.00052.x

Kim, K.J., Balaish, M., Wadaguchi, M., Kong, L., Rupp, J.L.M., 2021. Solid - State Li–Metal Batteries: Challenges and Horizons of Oxide and Sulfide Solid Electrolytes and Their Interfaces. *Advanced Energy Materials*, 11, 2002689. https://doi.org/10.1002/aenm.202002689

Lastoskie, C., M., Dai, Q., 2015. Comparative life cycle assessment of laminated and vacuum vapor-deposited thin film solid-state batteries. *Journal of Cleaner Production,* 91, 158–169. https://doi.org/10.1016/j.jclepro.2014.12.003

Lee, Y.-G., Fujiki, S., Jung, C., Suzuki, N., Yashiro, N., Omoda, R., Ko, D.-S., Shiratsuchi, T., Sugimoto, T., Ryu, S., Ku, J.H., Watanabe, T., Park, Y., Aihara, Y., Im, D., Han, I.T., 2020. High-energy long-cycling all-solid-state lithium metal batteries enabled by silver–carbon composite anodes. *Nature Energy,* 5, 299–308. https://doi.org/10.1038/s41560-020-0575-z

Li, C., Zhang, S., Miao, X., Wang, Cong, Wang, Chengxiang, Zhang, Z., Wang, R., Yin, L., 2022. Designing Lithium Argyrodite Solid-State Electrolytes for High-Performance All-Solid-State Lithium Batteries. *Batteries & Supercaps*, 5, e202100288. https://doi.org/10.1002/batt.202100288

Liang, F., Sun, Y., Yuan, Y., Huang, J., Hou, M., Lu, J., 2021. Designing inorganic electrolytes for solid-state Li-ion batteries: A perspective of LGPS and garnet. *Materials Today*, 50, 418–441. https://doi.org/10.1016/j.mattod.2021.03.013

Lopez, S., Akizu-Gardoki, O., Lizundia, E., 2021. Comparative life cycle assessment of high performance lithium-sulfur battery cathodes. *Journal of Cleaner Production*, 282, 124528. https://doi.org/10.1016/j.jclepro.2020.124528

Lorric, 2022. *PVDF material datasheet.* [data set] Available at: https://www.lorric.com/en/WhyLORRIC/Material/material-chemical-resistance-chart-PVDF [Accessed 8 mars 2022]

Loveless, M., 2022. *Energy Storage: The Key to a Reliable, Clean Electricity Supply.* [Online] Energy.gov Available at: https://www.energy.gov/articles/energy-storage-key-reliable-clean-electricity-supply [Accessed 11 february 2022]

Lutsey, N., Grant, M., Wappelhorst, S., Zhou, H., 2018. Power play: How governments are spurring the electric vehicle industry. *White Paper.*

Ma, J., Li, Y., Grundish, N.S., Goodenough, J.B., Chen, Y., Guo, L., Peng, Z., Qi, X., Yang, F., Qie, L., Wang, C.-A., Huang, B., Huang, Z., Chen, L., Su, D., Wang, G., Peng, X., Chen, Z., Yang, J., He, S., Zhang, X., Yu, H., Fu, C., Jiang, M., Deng, W., Sun, C.-F., Pan, Q., Tang, Y., Li, X., Ji, X., Wan, F., Niu, Z., Lian, F., Wang, C., Wallace, G.G., Fan, M., Meng, Q., Xin, S., Guo, Y.-G., Wan, L.-J., 2021. The 2021 battery technology roadmap. *Journal of Physics D: Applied Physics*, 54, 183001. https://doi.org/10.1088/1361-6463/abd353

Ma, J., Chen, B., Wang, L., Cui, G., 2018. Progress and prospect on failure mechanisms of solid-state lithium batteries. *Journal of Power Sources*, 392, 94–115. https://doi.org/10.1016/j.jpowsour.2018.04.055

Meng, N., Zhu, X., Lian, F., 2022. Particles in composite polymer electrolyte for solid-state lithium batteries: A review. *Particuology*, 60, 14–36. https://doi.org/10.1016/j.partic.2021.04.002

Moni, S., 2020. A Framework for Life Cycle Assessment (LCA) of Emerging Technologies at Low Technology Readiness Levels. PhD thesis, Clemson University.

Morganti, M.V., Longo, S., *Tirovic*, M., Blaise, C.-Y., Forostovsky, G., 2019. Multi-scale, electro-thermal model of NMC battery cell. IEEE *Transactions on Vehicular Technology*, 68, 10594–10606. https://doi.org/10.1109/TVT.2019.2943052

MSE Supplies, 2022. *Lithium Nickel Manganese Cobalt Oxide, LiNi0.8Co0.1Mn0.1O2 NMC 811 Cathode Powder 500g.* [Online] Available at: https://www.msesupplies.com/products/nmc-811-cathode-powder-500g-lithium-nickel-manganese-cobalt-oxide-powder?variant=16116292714554 [Accessed 5 mars 2022]

MTI Corporation, 2022. *Aluminum Laminated Film for Pouch Cell Case.* [Online] Available at: https://www.mtixtl.com/AluminumLaminatedFilmforPolymerBatteryCase100mmWx210mmL50pcs.aspx [Accessed 7 mars 2022]

Nanda, S., Gupta, A., Manthiram, A., 2021. Anode-Free Full Cells: A Pathway to High-Energy Density Lithium-Metal Batteries. *Advanced Energy Materials*, 11, 2000804. https://doi.org/10.1002/aenm.202000804

Nehb, W., Vydra, K., 2006. *Sulfur, in: Ullmann's Encyclopedia of Industrial Chemistry*, John Wiley & Sons, Ltd. https://doi.org/10.1002/14356007.a25_507.pub2

Nordelöf, A., Messagie, M., Tillman, A.-M., Ljunggren Söderman, M., Van Mierlo, J., 2014. Environmental impacts of hybrid, plug-in hybrid, and battery electric vehicles—what can we learn from life cycle assessment? *The International Journal of Life Cycle Assessment*,19, 1866–1890. https://doi.org/10.1007/s11367-014-0788-0

Oh, P., Yun, J., Choi, J.H., Saqib, K.S., Embleton, T.J., Park, S., Lee, C., Ali, J., Ko, K., Cho, J., 2022. Development of High Energy A node s for All-Solid-State Lithium Batteries Based on Sulfide Electrolytes. *Angewandte Chemie*, n/a. https://doi.org/10.1002/ange.202201249

OpenLCA, 2022. *openLCA modeling suite.* [Online] Available at: https://www.openlca.org/openlca/ [Accessed 21 february 2022]

Owen, J., 1989. 21 - Ionic Conductivity, in: Allen, G., Bevington, J.C. (Eds.). *Comprehensive Polymer Science and Supplements*, Pergamon, Amsterdam, pp. 669–686. https://doi.org/10.1016/B978-0-08-096701-1.00058-6

Pasta, M., Armstrong, D., Brown, Z.L., Bu, J., Castell, M.R., Chen, P., Cocks, A., Corr, S.A., Cussen, E.J., Darnbrough, E., Deshpande, V., Doerrer, C., Dyer, M.S., El-Shinawi, H., Fleck, N., Grant, P., Gregory, G.L., Grovenor, C., Hardwick, L.J., Irvine, J.T.S., Lee, H.J., Li, G., Liberti, E., McClelland, I., Monroe, C., Nellist, P.D., Shearing, P.R., Shoko, E., Song, W., Jolly, D.S., Thomas, C.I., Turrell, S.J., Vestli, M., Williams, C.K., Zhou, Y., Bruce, P.G., 2020. 2020 roadmap on solid-state batteries. *Journal of Physics: Energy*, 2, 032008. https://doi.org/10.1088/2515-7655/ab95f4

Peters, J.F., Baumann, M., Zimmermann, B., Braun, J., Weil, M., 2017. The environmental impact of Li-Ion batteries and the role of key parameters – A review. *Renewable and Sustainable Energy Reviews*, 67, 491–506. https://doi.org/10.1016/j.rser.2016.08.039

Piccinno, F., Hischier, R., Seeger, S., Som, C., 2016. From laboratory to industrial scale: a scale-up framework for chemical processes in life cycle assessment studies. *Journal of Cleaner Production*, 135, 1085–1097. https://doi.org/10.1016/j.jclepro.2016.06.164

RIVM, 2011. LCIA: the ReCiPe model. [Online] Available at: https://www.rivm.nl/en/life-cycle-assessment-lca/recipe [Accessed 21 february 2022].

Rumble, J., 2021. *CRC Handbook of Chemistry and Physics.* 102nd Edition (Internet Version 2021). CRC Press/Taylor & Francis, Boca Raton, FL

Porzio, J., Scown, C.D., 2021. Life-Cycle Assessment Considerations for Batteries and Battery Materials. *Advanced Energy Materials*, 11, 2100771. https://doi.org/10.1002/aenm.202100771

Sakuda, A., Hayashi, A., Tatsumisago, M., 2013. Sulfide Solid Electrolyte with Favorable Mechanical Property for All-Solid-State Lithium Battery. *Scientific Reports*, 3, 2261. https://doi.org/10.1038/srep02261

Sandin, G., Røyne, F., Berlin, J., Peters, G.M., Svanström, M., 2015. Allocation in LCAs of biorefinery products: implications for results and decision-making. *Journal of Cleaner Production*, 93, 213–221. https://doi.org/10.1016/j.jclepro.2015.01.013

Sato, Y., Takeda, O., 2013. 22 - Hydrogen Storage and Transportation System through Lithium Hydride Using Molten Salt Technology, in: Lantelme, F., Groult, H. (Eds.), *Molten Salts Chemistry*, Elsevier, Oxford, 451–470. https://doi.org/10.1016/B978-0-12-398538-5.00022-6

Schnell, J., Günther, T., Knoche, T., Vieider, C., Köhler, L., Just, A., Keller, M., Passerini, S., Reinhart, G., 2018. All-solid-state lithium-ion and lithium metal batteries – paving the way to large-scale production. *Journal of Power Sources*, 382, 160–175. https://doi.org/10.1016/j.jpowsour.2018.02.062

Seetharaman, S., Tekumalla, S., Gupta, M., 2020. *Magnesium-Based Nanocomposites, Advances and applications*. IOP Publishing. https://doi.org/10.1088/978-0-7503-3535-5

Shao, Y., El-Kady, M.F., Sun, J., Li, Y., Zhang, Q., Zhu, M., Wang, H., Dunn, B., Kaner, R.B., 2018. Design and Mechanisms of Asymmetric Supercapacitors. *Chemical Reviews.*,118, 9233–9280. https://doi.org/10.1021/acs.chemrev.8b00252

Sharp, B.E., Miller, S.A., 2016. Potential for integrating diffusion of innovation principles into life cycle assessment of emerging technologies. *Environmental Science & Technology*, 50, 2771–2781. https://doi.org/10.1021/acs.est.5b03239

Shigenobu, K., Dokko, K., Watanabe, M., Ueno, K., 2020. Solvent effects on Li ion transference number and dynamic ion correlations in glyme- and sulfolane-based molten Li salt solvates. *Physical Chemistry Chemical Physics*, 22, 15214–15221. https://doi.org/10.1039/D0CP02181D

SkySpring Nanomaterials, inc (2022). *Silver Nanoparticles/Nanopowder (Ag, 99.9% 50-60 nm)*. [Online] Available at: https://www.ssnano.com/inc/sdetail/silver_nanoparticles_nanopowder__ag__99_9__50_60_nm_/266 [Accessed 8 mars 2022]

Smith, L., Ibn-Mohammed, T., Astudillo, D., Brown, S., Reaney, I.M., Koh, S.C.L., 2021. The Role of Cycle Life on the Environmental Impact of Li6.4La3Zr1.4Ta0.6O12 based Solid-State Batteries. *Advanced Sustainable Systems*, 5, 2000241. https://doi.org/10.1002/adsu.202000241

Sonnemann, G., Tsang, M., Schuhmacher, M., 2018. *Integrated life-cycle and risk assessment for industrial processes and products*. Boca Raton: CRC Press.

Spielmann, M., Bauer, C., Dones, R., Tuchschmid, m., 2007. *Transport services*. [PDF] Ecoinvent report No. 14. Swiss Centre for Life Cycle Inventories. Dübendorf, 2007. [Accessed 4 april 2022]

Swedish Energy Agency, 2020. *Energiläget 2020*. [PDF] Swedish Energy Agency. Eskilstuna, Sweden. [Accessed 8 april 2022]

Sun, Y.-K., 2020. Promising All-Solid-State Batteries for Future Electric Vehicles. *ACS Energy Letters*, 5, 3221–3223. https://doi.org/10.1021/acsenergylett.0c01977

Tan, D.H.S., Banerjee, A., Chen, Z., Meng, Y.S., 2020. From nanoscale interface characterization to sustainable energy storage using all-solid-state batteries. *Nature Nanotechnology*, 15, 170–180. https://doi.org/10.1038/s41565-020-0657-x

Tang, S., Guo, W., Fu, Y., 2021. Advances in Composite Polymer Electrolytes for Lithium Batteries and Beyond. *Advanced Energy Materials*, 11, 2000802. https://doi.org/10.1002/aenm.202000802

Temizel-Sekeryan, S., Hicks, A.L., 2020. Global environmental impacts of silver nanoparticle production methods supported by life cycle assessment. *Resources, Conservation and Recycling*, 156, 104676. https://doi.org/10.1016/j.resconrec.2019.104676

Troy, S., Schreiber, A., Reppert, T., Gehrke, H.-G., Finsterbusch, M., Uhlenbruck, S., Stenzel, P., 2016. Life Cycle Assessment and resource analysis of all-solid-state batteries. *Applied Energy*, 169, 757–767. https://doi.org/10.1016/j.apenergy.2016.02.064

Thonemann, N., Schulte, A., Maga, D., 2020. How to Conduct Prospective Life Cycle Assessment for Emerging Technologies? A Systematic Review and Methodological Guidance. *Sustainability*, 12, 1192. https://doi.org/10.3390/su12031192

Varzi, A., Thanner, K., Scipioni, R., Di Lecce, D., Hassoun, J., Dörfler, S., Altheus, H., Kaskel, S., Prehal, C., Freunberger, S.A., 2020. Current status and future perspectives of lithium metal batteries. *Journal of Power Sources*, 480, 228803. https://doi.org/10.1016/j.jpowsour.2020.228803

Vieira, M.D.M., Ponsioen, T.C., Goedkoop, M.J., Huijbregts, M.A.J., 2017. Surplus Ore Potential as a Scarcity Indicator for Resource Extraction. *Journal of Industrial Ecology*, 21, 381–390. https://doi.org/10.1111/jiec.12444

Wang, S., Fan, Y., Stroe, D.-I., Fernandez, C., Yu, C., Cao, W., Chen, Z., 2021. Chapter 1 - Lithium-ion battery characteristics and applications, in: Wang, S., Fan, Y., Stroe, D.-I., Fernandez, C., Yu, C., Cao, W., Chen, Z. (Eds.), *Battery System Modeling*. Elsevier, pp. 1–46. https://doi.org/10.1016/B978-0-323-90472-8.00003-2

Xia, S., Wu, X., Zhang, Z., Cui, Y., Liu, W., 2019. Practical Challenges and Future Perspectives of All-Solid-State Lithium-Metal Batteries. *Chem*, 5, 753–785. https://doi.org/10.1016/j.chempr.2018.11.013

Yadav, D., Amini, F., Ehrmann, A., 2020. Recent advances in carbon nanofibers and their applications – A review. *European Polymer Journal*, 138, 109963. https://doi.org/10.1016/j.eurpolymj.2020.109963

Yang, C., Xie, H., Ping, W., Fu, K., Liu, B., Rao, J., Dai, J., Wang, C., Pastel, G., Hu, L., 2019. An Electron/Ion Dual-Conductive Alloy Framework for High-Rate and High-Capacity Solid-State Lithium-Metal Batteries. *Advanced Materials 31*, 1804815. https://doi.org/10.1002/adma.201804815

Yang, X., R. Adair, K., Gao, X., Sun, X., 2021. Recent advances and perspectives on thin electrolytes for high-energy-density solid-state lithium batteries. *Energy & Environmental Science*,14, 643–671. https://doi.org/10.1039/D0EE02714F

Cao, Y., China, 2008. *Production process of lithium alcoholate*. Google patents. CN101412659A. Available at: https://patents.google.com/patent/CN101412659A/en

Yu, Y., Liu, Y., Xie, J., 2021a. Building Better Li Metal Anodes in Liquid Electrolyte: Challenges and Progress. *ACS Applied Materials & Interfaces*, 13, 18–33. https://doi.org/10.1021/acsami.0c17302

Yu, C., Zhao, F., Luo, J., Zhang, L., Sun, X., 2021b. Recent development of lithium argyrodite solid-state electrolytes for solid-state batteries: Synthesis, structure, stability and dynamics. *Nano Energy*, 83, 105858. https://doi.org/10.1016/j.nanoen.2021.105858

Zackrisson, M., 2021. *Life cycle assessment of electric vehicle batteries and new technologies*. PhD thesis, KTH Royal Institute of Technology.

Zhang, J., Ke, X., Gu, Y., Wang, F., Zheng, D., Shen, K., Yuan, C., 2022. Cradle-to-gate life cycle assessment of all-solid-state lithium-ion batteries for sustainable design and manufacturing. *International Journal of Life Cycle Assessment* 27, 227–237. https://doi.org/10.1007/s11367-022-02023-2

Zhang, Q., Cao, D., Ma, Y., Natan, A., Aurora, P., Zhu, H., 2019. Sulfide-Based Solid-State Electrolytes: Synthesis, Stability, and Potential for All-Solid-State Batteries. *Advanced Materials*, 31, 1901131. https://doi.org/10.1002/adma.201901131

Zhu, P., Gastol, D., Marshall, J., Sommerville, R., Goodship, V., Kendrick, E., 2021. A review of current collectors for lithium-ion batteries. *Journal of Power Sources*, 485, 229321. https://doi.org/10.1016/j.jpowsour.2020.229321

Zhou, L., Park, K.-H., Sun, X., Lalère, F., Adermann, T., Hartmann, P., Nazar, L.F., 2018. Solvent-engineered design of argyrodite Li6PS5X (X= Cl, Br, I) solid electrolytes with high ionic conductivity. *ACS Energy Letters*, 4, 265–270. http://dx.doi.org/10.1021/acsenergylett.8b01997

Appendix A

Detailed process descriptions and unit process data

This appendix provides a detailed description of the production process for each of the components and their material inputs, as well as the unit process datasets for the processes required for the pouch cell production. Descriptions of the production steps for the primary components were obtained from the article by Lee et al. (2020). Furter material inputs and their production methods were gathered from published articles and patents. The sources for each production step are represented by the colors in the flowcharts under each process.

A1 Catholyte sheet production

The catholyte sheet consists of a coated NMC 811 active cathode material, the electrolyte powder, CNF, and a polytetrafluoroethylene binder. Firstly, these are mixed in a weight ratio of 85:15:3:1.5 in dehydrated xylene solvent. The second step is a dry-filming process (Lee et al., 2020). The dry-filming process includes placing the mixture on a hot plate, after which it is rolled to achieve the desired thickness (Hippauf et al., 2019). All processes in the preparation of the catholyte sheet were performed in a dry room. The production procedure is presented in Figure A1.1.

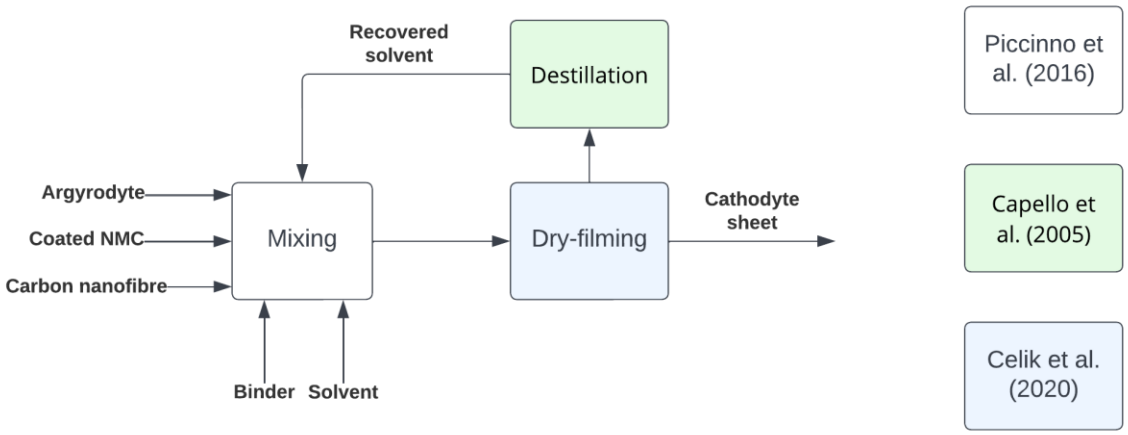

Figure A1.1: *Flowchart showing the catholyte sheet production*

The unit-process data for the catholyte sheet production consisted mostly of modeling each input component and process. Detailed calculations of mass can be found in Appendix B1 and B2, and process energy in Appendix C1. Further details on each component in the catholyte sheet can be found in Appendix A1.1 - A1.3 and A2.1.

The unit process data results for the catholyte sheet production are presented in Table A1.1. The inventory for the LZO coated NMC 811, the argyrodite powder and CNF were based on modeling using data from other published articles and LCAs. The inventory data for polytetrafluoroethylene was not found in the Ecoinvent v3.8. database. Instead, a flow of tetrafluoroethylene is used as a proxy on the basis that those flows have been used interchangeably in Ecoinvent (Althaus et al., 2007). The quantitative input of the xylene solvent was not reported by Lee et al. (2020) and instead based on assumptions presented in Section 4.

Table A1.1: *Unit process data results for the catholyte sheet production.*

Material inputs normalized to unit process			
Component/process	**Quantity**	**Unit**	**Linked upstream process**
LZO-NMC 8:1:1	0.813	g	Sol-gel coating (process A1.2)
Argyrodite powder	0.144	g	Electrolyte powder production (process A2.1)
CNF	0.0287	g	Carbon nanofiber manufacturing (process A1.3)
Polytetrafluoroethylene	0.0144	g	market for tetrafluoroethane | Cutoff, S - GLO
Process inputs normalized to unit process			
Xylene	1	g	market for xylene |Cutoff, S - RER
Water	0.027	g	market group for tap water | Cutoff, S - GLO
Electricity	0.655	Wh	market for electricity, medium voltage | Cutoff, S - SE/SK
Heat	4.28	kJ	Swedish heat production (process A6.3) / market for heat, district or industrial, natural gas | Cutoff, S - RoW
Emissions to air			
NMVOC	0.01	g	Emission to air, unspecified
Outputs			
Composite catholyte	1	g	
Xylene (recovered)	0.95 (0.50*)	g	Recovered resource
Hazardous waste, for incineration	0.05 (0.50*)	g	market for hazardous waste, for incineration | Cutoff, S - RoW

*Pessimistic scenario

A1.1 Active cathode material (NMC 811) production

The NMC oxide powder (active cathode material) is the main component in the catholyte sheet and was modeled using inventory data from Chordia et al. (2021). The production process is represented in Figure A1.2 as modeled by Chordia et al. (2021). The data collected consist of inputs of material, processes, and energy as well as outflows in the form of emissions, wastewater, and losses. The NMC oxide powder mainly consists of nickel (Ni), manganese (Mn), cobalt (Co) (metal sulfate solutions) and lithium (Li) (metal hydroxide). Other inputs are oxygen (O_2) and smaller amounts of other metals (Chordia et al., 2021).

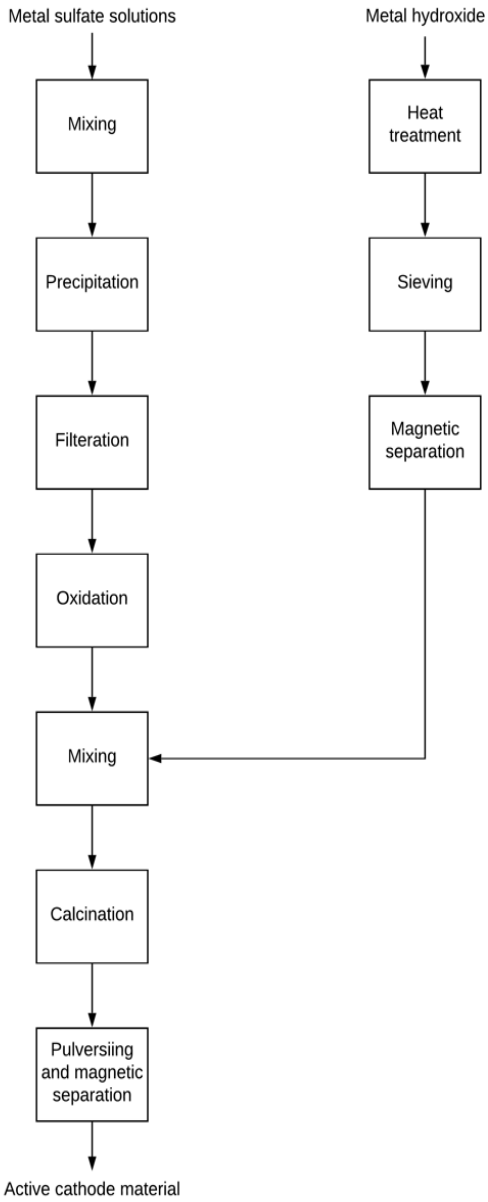

Figure A1.2: *Flowchart showing the active cathode material production. Obtained from Chordia et al. (2021).*

The inputs in Chordia et al. (2021) were calculated using annual consumption data, scaled to represent the production of one gram of the active cathode material, which is NMC 811 powder. The unit process data is presented in Table A1.2. The data source for the input materials was based on available Ecoinvent datasets. The output of wastewater from the process was based on modeling of wastewater in Chordia et al. (2021).

Table A1.2: Unit process data results for NMC 811 powder production

Material inputs normalized to unit process			
Component/process	**Quantity**	**Unit**	**Linked upstream process**
Nickel sulfate	1.54	g	market for nickel sulfate | nickel sulfate | Cutoff, S – GLO
Cobalt sulfate	0.175	g	market for cobalt sulfate | cobalt sulfate | Cutoff, S – RoW
Manganese sulphate	0.175	g	market for manganese sulfate | manganese sulfate | Cutoff, S – GLO
Lithium hydroxide	0.265	g	market for lithium hydroxide | lithium hydroxide | Cutoff, S – GLO
Process inputs normalized to unit process			
Sulphuric acid	0.978	g	market for sulfuric acid | sulfuric acid | Cutoff, S – RER
Ammonia	0.0244	g	market for ammonia, anhydrous, liquid | ammonia, anhydrous, liquid | Cutoff, S – RER
Sodium hydroxide	2.00	g	market for sodium hydroxide, without water, in 50% solution state | sodium hydroxide, without water, in 50% solution state | Cutoff, S – GLO
Deionized water	67.5	g	market for water, deionised | water, deionised | Cutoff, S - Europe without Switzerland
Liquid oxygen	0.244	g	market for oxygen, liquid | oxygen, liquid | Cutoff, S – RER
Electricity	6.21E-03	kWh	market for electricity, medium voltage | Cutoff, S - SE/SK
Heat	9.32E-04	MJ	Swedish heat production (A6.3) / market for heat, district or industrial, natural gas | Cutoff, S - RoW
Cooling	5.95E-03	MJ	cooling energy, from natural gas, at cogen unit with absorption chiller 100kW| Cutoff, S - SE/ROW
Outputs			
NMC 8:1:1 active material	1	g	
Wastewater, for treatment	67.5	g	Wastewater treatment (process A6.1)
Precursor and active material residues, recyclable	1.5	g	Scrap transport (process A6.2)
Metal dust particles	7.63E-06	g	Emission to air, unspecified Particulates, > 2.5 um, and < 10um

A1.2 Sol-gel coating

The first step in the production process of the coated NMC 811 cathode is the preparation of the LZO solution. The coating solution is prepared by mixing lithium methoxide (10% lithium methoxide in a methanol solution) and zirconium(IV) tetrapropoxide in an anhydrous 2-propanol solvent in a 20:1:200 molar ratio (Lee et al., 2020), as shown in Figure A1.3. The prepared LZO solution is then used to coat the NMC 811 powder using a sol-gel method. The method includes the mixing of the LZO coating solution and the NMC 811 cathode for 1 hour, after which the mixture is dried under vacuum in a water bath at 50°C with continuous sonication. During the vacuum drying, the solvents used in the LZO solution are evaporated. After the mixture has been dried, it is filtered and then heated for 1 hour at 300 °C to obtain the final product, which is the LZO-coated NMC 811 cathode.

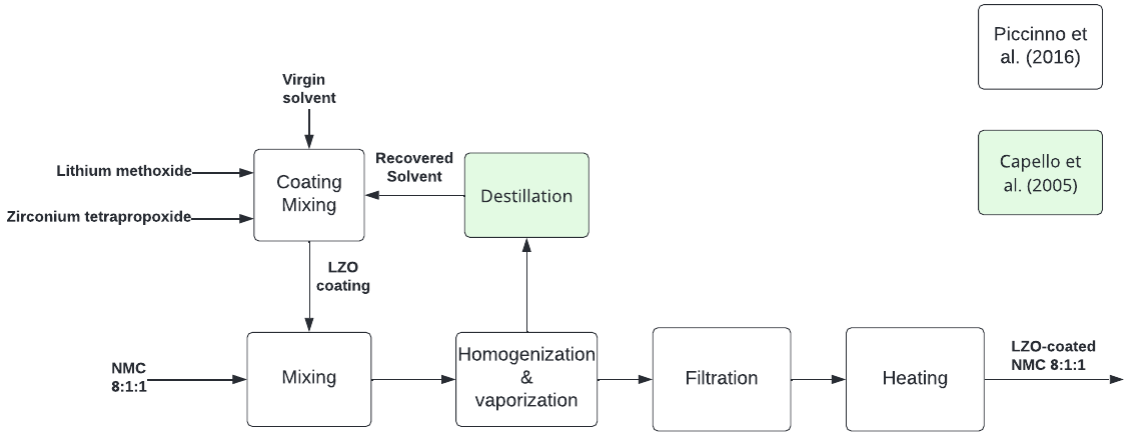

Figure A1.3: *Flowchart showing the sol-gel coating.*

The quantitative input of the LZO solution was based on stoichiometric calculations, with an assumed 100% reaction yield (Appendix B2.1). The mixing ratio between the LZO coating solution and the NMC 811 powder was not stated in Lee et al. (2020). Therefore, an assumption was made that 0.5 mol% LZO coating solution was used in the preparation, based on a study of an LZO-coated NCA cathode (Ito et al., 2014). The coating process was assumed to have a yield of 100% as no other information was available from the lab-scale description (Lee et al., 2020).

The process energy for the sol-gel coating procedure, as well as material inputs, are summarized in Table A1.3. Detailed calculations and assumptions on the process energy can be found in Appendix C1.1. The process energy for mixing the LZO coating solution was excluded, as it was assumed neglectable.

The sol-gel coating itself does not require solvent input, but the LZO solution contains inputs of both propanol and methanol (from the lithium methoxide solution). As the amount of methanol from the lithium methoxide is small compared to the propanol, the amount of methanol was neglected from solvent recirculation and emission calculations. The process energy for recirculation was calculated by replacing the vacuum drying with distillation energy as described in Section 4. The sonication step of the drying was assumed to be required and therefore included in the total process energy for the sol-gel coating.

Data inventory for the NMC 811 powder production was collected from Chordia et al. (2021). The propanol solvent was not available, but instead approximated with isopropanol from Ecoinvent v3.8. Inventory data for lithium methoxide (10%) were not found in Ecoinvent v.3.8 and the inventory data used for its modeling is presented in Appendix A1.4.

Zirconium (IV) tetrapropoxide was also not available in Ecoinvent v3.8, and no synthesis method was found. Instead, the inventory data was approximated with an input of zirconium oxide only. This choice was made as the process energy for the preparation is likely negligible due to very small quantities used. The zirconium requirement for the production of the pouch cell was based on stoichiometric relations (Appendix B2.1.2), and the amount of zirconium oxide input was calculated based on the zirconium requirement.

Table A1.3: Unit process data results for sol-gel coating production.

Material Inputs normalized to unit process			
Component/process	**Quantity**	**Unit**	**Linked upstream process**
NMC 811	0.992	G	NMC 811 production (process A1.1)
Lithium methoxide	0.0126	G	Lithium methoxide production (process A1.2.1)
Zirconium (IV) tetrapropoxide	0.0063 (0.0024*)	G	market for zirconium oxide | zirconium oxide | Cutoff, S – GLO
Process inputs normalized to unit process			
2-propanol	0.233	G	market for isopropanol | isopropanol | Cutoff, S - RER
Cooling water	0.0066	g	market group for tap water | Cutoff, S - GLO
Electricity	0.106	Wh	market for electricity, medium voltage | Cutoff, S - SE/SK
Heat	1.57	kJ	Swedish heat production (A6.3) / market for heat, district or industrial, natural gas | Cutoff, S - RoW
Emissions to air			
NMVOC	0.00233	g	emission to air, unspecified
Outputs			
LZO NMC 811 cathode	1	g	
Solvents, recovered	0.221 (0.116**)	g	Recovered resource
Hazardous waste, for incineration	0.0116 (0.116**)	g	market for hazardous waste, for incineration | Cutoff, S - RoW

*Amount of zirconium oxide used as proxy
**Pessimistic scenario

A1.2.1 Lithium methoxide production

The unit-process data for lithium methoxide production was estimated based on a patented production method by Cao (2008). The process consists of mixing the input materials of lithium (Li) and methanol (CH_3OH) in a 1.5:90 ratio. The mixture is stirred for 7 hours. The patent includes further process steps, but they were excluded from this study as the achieved solution mixture is the desired product. The process energy calculations for the mixing are presented in Appendix C1.1.1.

The quantities of lithium methoxide produced from the process was not stated in the patent and have therefore been calculated based on stoichiometry. The calculations were made with the assumption that only lithium methoxide, methanol and hydrogen gas is produced in the reaction, with a 100% reaction yield. In the impact assessment calculation, the hydrogen gas produced was excluded due to assumed neglectable impact. The unit

process data is summarized in Table A1.4. Detailed calculations of the mass balancing can be found in Appendix B2.1.1.

Table A1.4: *Unit process data results for lithium methoxide production.*

Material Inputs normalized to unit process			
Component/process	**Quantity**	**Unit**	**Linked upstream process**
Lithium	0.0164	g	market for lithium | lithium | Cutoff, S - GLO
Methanol	0.986	g	methanol production | methanol | Cutoff, S - GLO
Process inputs normalized to unit process			
Electricity	0.000126	Wh	market for electricity, medium voltage | Cutoff, S - SE/SK
Emission to air			
Hydrogen gas	0.0022	g	Neglected
Outputs			
Lithium methoxide (10% in methanol)	1	g	

A1.3 Carbon nanofibers

A small amount of CNF is added to the catholyte slurry to reduce interface problems and increase conductivity (Boaretto et al. 2020). CNFs have only recently begun to be used on an industrial scale, but its manufacturing techniques have seen rapid improvements due to its rising popularity in multiple applications (Yadav et al. 2020).

Since no Ecoinvent data for CNF production could be found, the inventory in this study was based on data from an LCA performed by Khanna et al. (2008). They model production of vapor-grown CNF (Figure A1.4), a method that has been used for several decades (Yadav et al. 2020). The production method includes using a quartz tube electric furnace with a carbon feedstock together with metals or alloys as catalysts (Yadav et al. 2020), hydrogen gas, a solvent and small amounts of sulfur to facilitate the CNF formation (Khanna et al., 2008). Further, the study by Khanna et al. (2008) considers three different carbon feedstocks: methane, ethylene, and benzene, where the methane feedstock was used in the pessimistic and benzene in the optimistic. The unit-process data in Khanna et al. (2008) does not account for emissions in the synthesis step of the CNF.

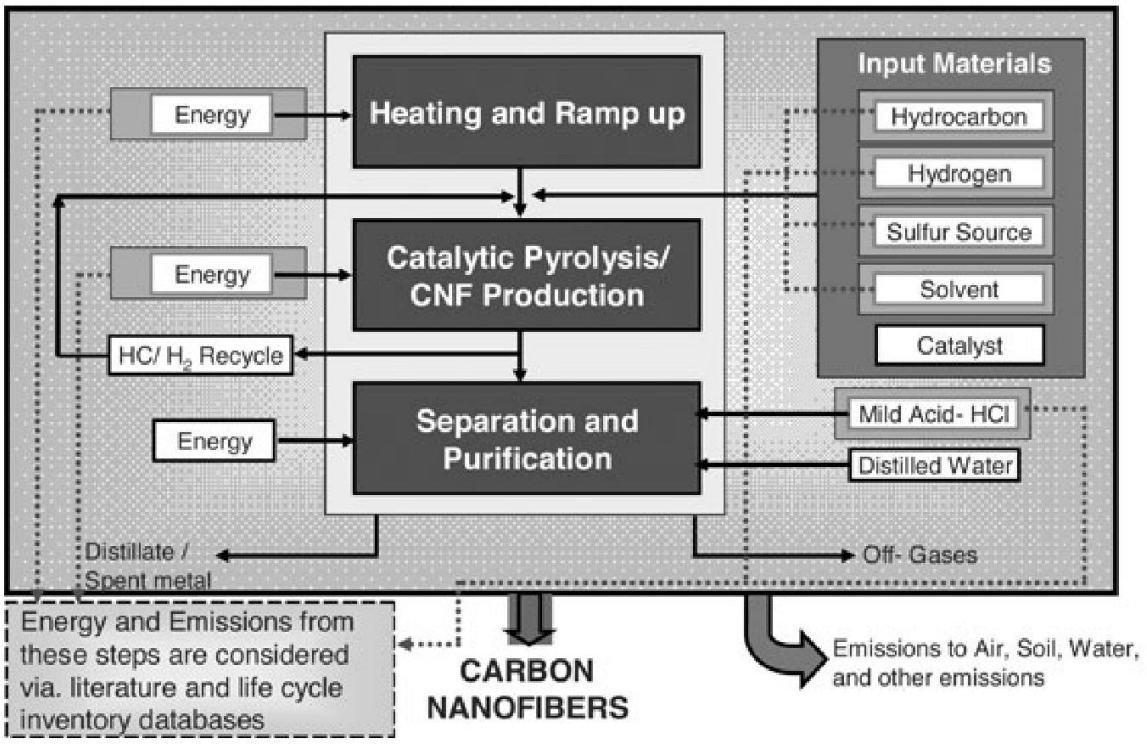

Figure A1.4: *Production process for vapor-grown CNFs. Obtained from Khanna et al. (2008) under license nr: 5334090349857.*

A1.3.1 Methane feedstock

The production process from Khanna et al. (2008) that has the highest impact is when methane is used as the feedstock. In this study, values for a methane feedstock without recycled streams was considered for the pessimistic scenario, since this is the feedstock most commonly used today (Yadav et al. 2020). When using methane as the feedstock, the catalyst of choice was ferrocene, the solvent hexane and the sulfur source was from hydrogen sulfide. The unit process data for CNF with methane as feedstock is presented in Table A1.5.

Table A1.5: *Unit process data results for CNF production using methane feedstock.*

Material Inputs normalized to unit process			
Component/process	**Quantity**	**Unit**	**Linked upstream process**
Methane	2.67	g	market for natural gas liquids| Cutoff, S – GLO
Process inputs normalized to unit process			
Hydrogen sulfide	0.28	g	market for hydrogen sulfide| Cutoff, S – RER
Hexane	14.3	g	market for hexane | Cutoff, S – GLO
Hydrogen gas	1.57	g	market for hydrogen, gaseous | Cutoff, S – GLO
Ferrocene	0.22	g	Neglected
Hydrochloric acid	16	g	market for hydrochloric acid, without water, in 30% solution state| Cutoff, S – RER
Electricity	2650	Wh	market for electricity, medium voltage | Cutoff, S - SE/SK
Outputs			
CNF	1	g	

A1.3.2 Benzene feedstock

Benzene as feedstock was selected for the optimistic scenario, as this feedstock required the least amount of process energy. The values without recycled streams from Khanna (2008) were used. In the production process where benzene is used as feedstock, the hydrogen source is thiophene, which were not available in Ecoinvent v3.8 and instead modeled as described in Section A1.3.2.1. The unit process data for CNF with benzene feedstock is summarized in Table A1.6.

Table A1.6: *Unit process data results for CNF production using methane feedstock.*

Material inputs normalized to unit process			
Component/process	**Quantity**	**Unit**	**Linked upstream process**
Benzene	4.7	g	market for benzene | Cutoff, S - GLO
Thiophene	0.03	g	Thiophene production (process A1.4.1)
Hydrogen gas	1.72	g	market for hydrogen, gaseous | Cutoff, S - GLO
Hydrochloric acid	16	g	market for hydrochloric acid, without water, in 30% solution state| Cutoff, S - RER
Electricity	678	Wh	market for electricity, medium voltage | Cutoff, S - SE/SK
Outputs			
CNF	1	g	

A1.3.2.1 Thiophene production

Trace amounts of a sulfur source are added in the production of the vapor-grown CNF. When using the benzene feedstock, the sulfur source of choice is thiophene (Khanna et al., 2008), which shares some characteristics with benzene. Thiophene was not included in Ecoinvent, so the unit process data were instead taken from Sonnemann et al. (2018). The results are presented in Table A1.7.

Table A1.7: *Unit process data results for thiophene production.*

Material inputs normalized to unit process			
Component/process	**Quantity**	**Unit**	**Linked upstream process**
Aluminum oxide	0.4	g	market for aluminium oxide, metallurgical | Cutoff, S - IAI Area, EU27 & EFTA
Butane	0.69	g	market for butane | Cutoff, S - GLO
Chromium oxide	0.8	g	market for chromium oxide, flakes | Cutoff, S - GLO
Hydrogen sulfide	1.22	g	market for hydrogen sulfide | Cutoff, S - RER
Sulfur	1.52	g	market for sulfur | Cutoff, S - GLO
Heat	1.81	MJ	Swedish heat production (process A6.3) / market for heat, district or industrial, natural gas | Cutoff, S - RoW
Outputs			
Thiophene	1	g	

A2. Electrolyte sheet

The production of the solid electrolyte sheet starts with an argyrodite electrolyte powder being mixed with a non-aqueous acrylate-type binder in a solvent consisting of 50% dehydrated xylene and 50% anhydrous isobutyl isobutyrate (Lee et al. 2020). The weight ratio between electrolyte powder and binder is 99:1, and an assumption is made that that relation refers to the dry weight of the binder. The input materials are mixed with a planetary centrifugal mixer with 4 Å molecular sieves and ZrO_2 beads at 2,000 r.p.m. for 6 min (Lee et al. 2020). The resulting electrolyte slurry is thereafter coated on a 75 µm thick PET film using doctor blading. After the doctor blading, the sheet is dried on a hotplate for a few minutes at 50°C, followed by a longer drying in a vacuum oven at 40°C overnight (12 h assumed). The prepared electrolyte sheet then requires some densification, but that happens in the pouch cell assembly, described in Appendix A5, where the entire stacked cell is pressed. The production process for the electrolyte sheet is shown in Figure A2.1.

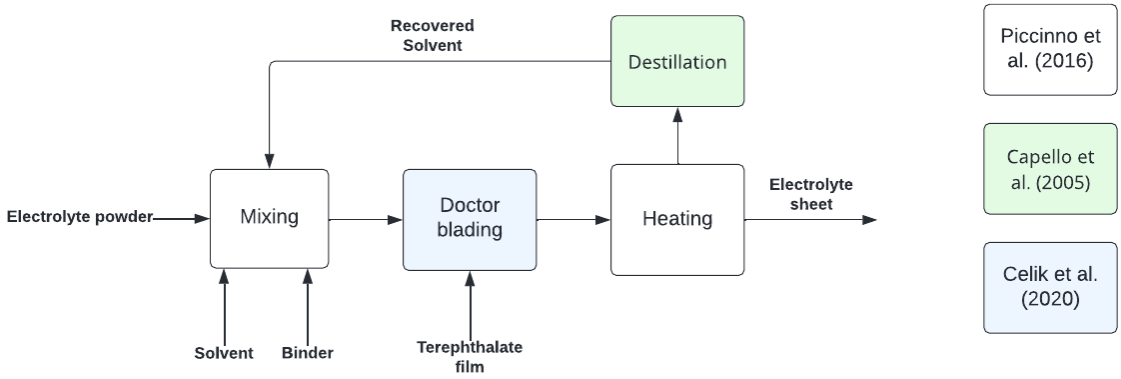

Figure A2.1: *Flowchart showing the electrolyte sheet production.*

The quantitative material input was not stated in Lee et al. (2020). Instead, the geometry and densities were used. Detailed descriptions of the mass calculations are found in Appendix B1.2. The amounts of xylene and isobutyl isobutyrate were assumed as described in Section 4.3. The xylene solvent was modeled using xylene as available in Ecoinvent v3.8. Isobutyl isobutyrate was missing in Ecoinvent and therefore isobutyl acetate was used as a proxy in the modeling. The PET film used was also not available in Ecoinvent v3.8, and instead modeled as described in Section A2.2. A summary of the unit process data is presented in Table A2.1.

The publication from Lee et al. (2020) does not provide any data on the amount of energy consumed in each of the production steps, and the energy was instead approximated using equations from Piccinno et al. (2016). The details of these calculations can be found in Appendix C2.

Table A2.1: *Unit process data results for electrolyte sheet production.*

Material inputs normalized to unit process			
Component/process	**Quantity**	**Unit**	**Linked upstream process**
Electrolyte powder	0.99	g	Electrolyte powder production (process A2.1)
Non-aqueous acrylate-type binder	0.01	g	market for acrylic binder, without water, in 34% solution state | Cutoff, S - RER
Process inputs normalized to unit process			
Xylene	0.5	g	market for xylene | Cutoff, S - RER
Anhydrous isobutyl isobutyrate	0.5	g	market for isobutyl acetate | Cutoff, S - GLO
Polyethylene terephthalate film	1.58	g	Terephthalate film production (process A2.2)
Electricity	1.20	Wh	market for electricity, medium voltage | Cutoff, S - SE/SK
Heat	4.28	KJ	Swedish heat production (A6.3) / market for heat, district or industrial, natural gas | Cutoff, S - RoW
Water	0.027	g	market group for tap water | Cutoff, S - GLO
Emissions to air			
NMVOC	0.01	g	Emission to air, unspecified
Outputs			
Electrolyte sheet	1	g	
Xylene (recovered)	0.95 (0.5*)	g	recovered resource
Spent solvent, for incineration	0.05 (0.5*)	g	market for hazardous waste, for incineration | Cutoff, S – RoW
waste polyethylene terephthalate	1.577	g	market group for waste polyethylene terephthalate | Cutoff, S - Europe without Switzerland

*Pessimistic scenario

A2.1 Electrolyte powder production

The argyrodite battery cell contained electrolyte powder with the chemical formula Li_6PS_5Cl. Lee et al. (2020) refers to a solvent-based production method by Zhou et al. (2018), which according to the authors is more scalable than an all-solid manufacturing method for this specific electrolyte powder. The process modeling was therefore based on the processes as described by Zhou et al. (2018).

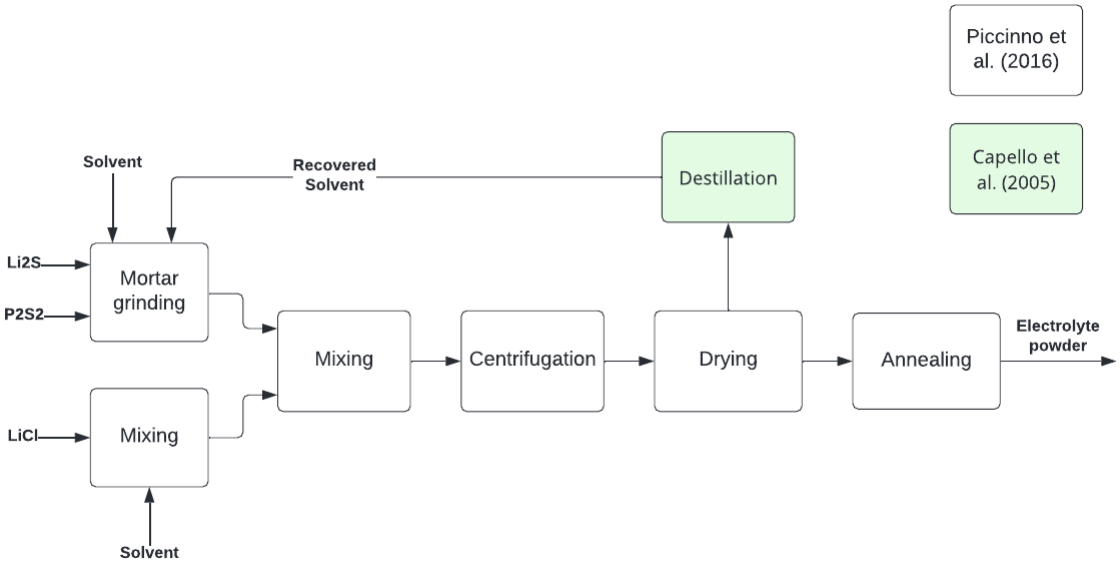

Figure A2.2: *Flowchart showing the rlectrolyte powder production.*

The solvent-based method begins by mixing a 3:1 molar ratio of Li_2S and P_2S_5 in a mortar and dispersing it in an anhydrous tetrahydrofuran solvent. This mixture is then stirred for 24 h at room temperature. More Li_2S are then dissolved together with LiCl in anhydrous ethanol solvent. The two mixtures are added to the same container, which is stirred overnight (12 h). The mixture was thereafter rapidly centrifuged at 8000 rpm, after which the solution was dried in a Buchi oven at 140°C under vacuum for 20 hours to evaporate the solvents. Finally, to achieve full crystallization of the Li_6PSCl, the powder is pressed into a pellet and sealed in a carbon-coated quartz tube where it is annealed at 550°C for 6 hours (Zhou et al., 2018). The production steps are presented in Figure A2.2.

The material input was estimated based on stoichiometry, which in turn was based on the stated ratio in Zhou et al. (2018). The amount of solvent was not disclosed in Lee et al. (2020). Therefore, the assumptions as described in Section 4.3 were used. The full unit process data results for the electrolyte powder is presented in Table A2.2.

Table A2.2: Unit process data results for electrolyte powder production.

Material inputs normalized to unit process			
Component/process	**Quantity**	**Unit**	**Linked upstream process**
Lithium sulfide	0.428	g	Lithium sulfide production (process B2.1.1)
Phosphorus pentasulfide	0.414	g	Phosphorus pentasulfide production (process B2.1.2)
Lithium chloride	0.158	g	market for lithium chloride | Cutoff, S - GLO
Process inputs normalized to unit process			
Anhydrous tetrahydrofuran	0.5	g	market for tetrahydrofuran | Cutoff, S - GLO
Anhydrous ethanol	0.5	g	market for ethanol, without water, in 99.7% solution state, from fermentation | Cutoff, S - GLO
Water	0.027	g	market group for tap water | Cutoff, S - GLO
Electricity	0.357	Wh	market for electricity, medium voltage | Cutoff, S - SE/SK
Heat	5.26	kJ	Swedish heat production (process A6.3) / market for heat, district or industrial, natural gas | Cutoff, S - RoW
Emission to air			
NMVOC	0.01	g	Emission to air, unspecified
Outputs			
Electrolyte	1	g	
Solvents (recovered)	0.95 (0.5*)	g	Recovered resources
Spent solvent, for incineration	0.05 (0.5*)	g	market for hazardous waste, for incineration | Cutoff, S - RoW

*Pessimistic scenario

A2.1.1 Lithium sulfide production

Lithium sulfide is produced by a synthesis reaction between sulfur powder and lithium hydride and was assumed based on a patent by Chu et al. (2015). The first step includes drying the sulfur powder at 100°C for 12 h, then the sulfur powder is mixed with lithium hydride and placed in a ball mill tank, which is then placed in a ball mill jar, and milled at 400 r/min for 8 hours at room temperature. The amount of each substance input and waste flow were calculated using stoichiometry, based on 100% reaction yield, resulting in only hydrogen gas as emissions, which was neglected from the impact assessment calculations. The unit process data is summarized in Table A2.3. Detailed calculations on the mass balancing can be seen in Appendix B2.3.1 and the process energy calculations in Appendix C2.2.

Table A2.3: Unit process data results for lithium sulfide production.

Inputs normalized to unit process			
Component/process	**Quantity**	**Unit**	**Linked upstream process**
Sulfur powder	0.696	g	market for sulfur | Cutoff, S – GLO
Lithium hydride	0.348	g	Lithium hydride production (process A2.1.1.1)
Electricity	0.016	Wh	market for electricity, medium voltage | Cutoff, S - SE/SK
Heat	81.7	J	Swedish heat production (process A6.3) / market for heat, district or industrial, natural gas | Cutoff, S - RoW
Emissions to air			
Hydrogen	0.0438	g	Emission to air
Outputs			
Lithium sulfide	1	g	

A2.1.1.1 Lithium hydride production

Lithium hydride is produced in a reaction between lithium and hydrogen gas at high temperature (Sato and Takeda, 2013). The mass of each substance was calculated using stoichiometric proportions, assuming 100% yield. The unit process data is summarized in Table A2.4. Detailed mass balancing and energy calculations can be seen in Appendix B2.3.1.3 and C2.2.1, respectively. The hydrogen gas was excluded due to uncertainty regarding where the hydrogen ended up.

Table A2.4: Unit process data results for lithium hydride production.

Inputs normalized to unit process			
Component/process	**Quantity**	**Unit**	**Linked upstream process**
Lithium	0.873	g	market for lithium | Cutoff, S - GLO
Hydrogen gas	0.127	g	Neglected
Heat	3.20	kJ	Swedish heat production (process A6.3) / market for heat, district or industrial, natural gas | Cutoff, S - RoW
Outputs			
Lithium hydride	1	g	

A2.1.2 Phosphorus pentasulfide production

The inventory data for phosphorus pentasulfide was modeled using a commonly used production method (ChemEuroupe, n.d; Bettermann et al., 2000), where liquid white phosphorus reacts with sulfide above 300°C. Stoichiometry was used for calculations with a 100% reaction yield. The unit process data is presented in Table A2.5. The detailed mass balancing is presented in Appendix B2.3. and the process energy calculations in Appendix C2.3.

Table A2.5: Unit process data results for phosphorus pentasulfide production.

Inputs normalized to unit process			
Component/process	**Quantity**	**Unit**	**Linked upstream process**
Phosphorous, white	0.279	g	market for phosphorus, white, liquid | Cutoff, S – GLO
Sulfur	0.721	g	market for sulfur | Cutoff, S – GLO
Heat	236	kJ	Swedish heat production (process A6.3) / market for heat, district or industrial, natural gas | Cutoff, S - RoW
Outputs			
Phosphorus pentasulfide	1	g	

A2.2 Terephthalate film production

The production of the electrolyte sheet involves coating the electrolyte slurry on a thin (75μm) film made of terephthalate (Lee et al., 2020). Due to lack of Ecoinvent data for such a film, the manufacturing was approximated with an input of polyethylene terephthalate granulate combined with a plastic film extrusion process. The extrusion process includes energy, waste, emissions, and transports. The summarized unit process data is presented in Table A2.6. The input weight is slightly higher than the output due to a yield that is specified in the extrusion process.

Table A2.6: Unit process data results for terephthalate film production

Inputs normalized to unit process			
Component/process	**Quantity**	**Unit**	**Linked upstream process**
polyethylene terephthalate	1.025	g	market for polyethylene terephthalate, granulate, bottle grade | Cutoff, S – GLO
Extrusion, plastic film	1.025	g	market for extrusion, plastic film | Cutoff, S – GLO
Outputs			
Terephthalate film	1	g	

A3. Ag-C separator layer production

The process of producing the Ag-C separator layer was described in Lee et al. (2020) and starts with mixing of AgNPs and carbon black with a polyvinylidene fluoride (PVDF) binder. The input materials are slowly mixed and dissolved in a N-methylpyrrolidone (NMP) solvent. The slurry is then coated on a 10-μm thick stainless-steel foil using a screen printer, after which the sheet is dried at 100°C for 12 h in a vacuum oven. The process is described in Figure A3.1.

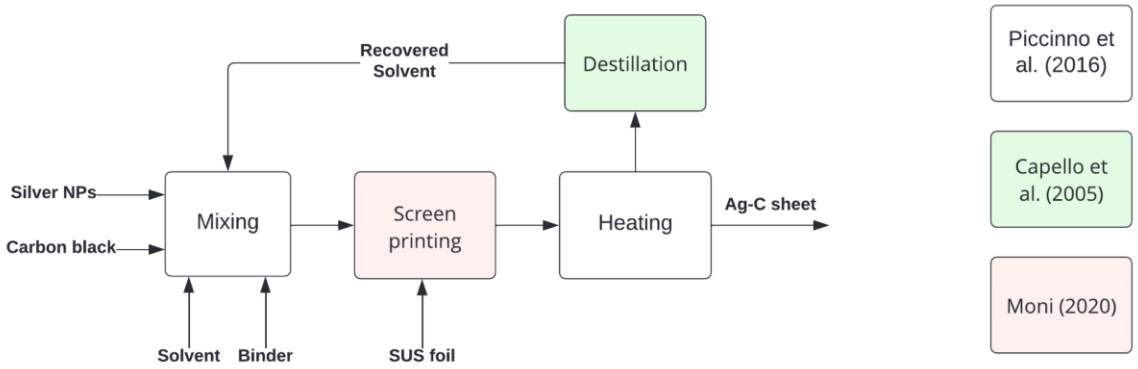

Figure A3.1: *Flowchart showing the Ag-C separator layer production process.*

Quantitative data on the amount of AgNPs and carbon black were not stated, but a ratio of 1:3 was provided. The input of each material was therefore based on the geometry and density calculations, combined with the weight ratio. The quantitative input of binder was also estimated based on a provided ratio between the solvent and binder. The solvent amount was assumed as described in Section 4.3. Details on mass calculations can be found in Appendix B1.3. The unit process data results are presented in Table A3.1.

Inventory data for AgNPs were not available in Ecoinvent v3.8, and instead based on LCI data from Temizel-Sekeryan and Hicks (2020) as presented in Section A3.2. The PVDF and carbon black were available in Ecoinvent v3.8. There is also a current collector consisting of stainless steel on each side of the argyrodite battery cell. Stainless-steel foil was not available in Ecoinvent v3.8 and instead modeled as described in Section A4.2.

Table A3.1: *Unit process data results for Ag-C separator layer production.*

Material inputs normalized to unit process			
Component/process	**Quantity**	**Unit**	**Linked upstream process**
AgNP	0.0744	g	AgNP production (process A3.2)
Carbon black powder	0.223	g	market for carbon black | Cutoff, S – GLO
PVDF	0.00301	g	market for polyvinyl fluoride | Cutoff, S – GLO
Stainless steel foil	0.700	g	Stainless steel foil production (process A4.2)
Process inputs normalized to unit process			
N-methylpyrrolidone	0.0399	g	market for N-methyl- 2-pyrrolidone | Cutoff, S – GLO
Electricity	0.159	Wh	market for electricity, medium voltage | Cutoff, S – SE/SK
Heating	171	J	market for steam, in chemical industry | Cutoff, S – RER
Water	0.00108	g	market group for tap water | Cutoff, S – GLO
Emissions to air			
NMVOC	0.000399	g	Emission to air, unspecified
Outputs			
Ag-C separator layer	1	g	
N-methylpyrrolidone, recovered	0.0379 (0.0200*)	g	market for N-methyl-2-pyrrolidone | N-methyl-2-pyrrolidone | Cutoff, S – GLO
Spent solvent, for incineration	0.00200 (0.0200*)	g	market for hazardous waste, for incineration | Cutoff, S – RoW

*Pessimistic Scenario

A3.2 Silver nanoparticles production

The use of AgNPs as a stabilizing agent in the separator layer was in many ways what characterized the studied battery cell. While the silver content is rather low (8-16 mg/Ah) (Lee et al., 2020), it was still expected to have a large impact on both the energy requirement and the mineral resource depletion impact category. Since no dataset for AgNPs were available in Ecoinvent, inventory data from an LCA of AgNP production from Temizel-Sekeryan and Hicks (2020) was used. In their work, they explore 13 different production methods for AgNPs. For this study, two of the methods that were claimed to be suitable for producing nanoparticles of correct size (diameter ≈ 60 nm) for electronic applications were chosen.

A3.2.1 Silver nanoparticles production (reactive magnetron sputtering)

In reactive magnetron sputtering (RMS) method, argon (Ar) is used for bombardment of the sputtering target, i.e. the silver. A mixture of Ar and nitrogen gas is used to place films of oxide or nitride forms of the target

material onto the substrate surface. All of the input materials were available in Ecoinvent v3.8. The data of the RMS production process is summarized in Table A3.2.

***Table A3.2**: Unit process data results for AgNPs with RMS production.*

Inputs normalized to unit process			
Component/process	**Quantity**	**Unit**	**Linked upstream process**
Silver	1	g	Market for silver | Cutoff, S - GLO
Argon	0.124	g	market for argon, liquid | Cutoff, S - RER
Nitrogen	0.0104	g	market for nitrogen, liquid | Cutoff, S - RER
Electricity	27.8	Wh	market for electricity, medium voltage | Cutoff, S - SE/SK
Outputs			
AgNP (RMS)	1	g	

A3.2.2 Silver nanoparticles production (arc plasma)

The arc plasma (AP) method uses energy delivered through continuous electrical discharge to produce pure metallic nanoparticles. The summarized data for the AP production method is summarized in Table A3.3.

***Table A3.3**: Unit process data results for AgNPs with AP production.*

Inputs normalized to unit process			
Component/process	**Quantity**	**Unit**	**Linked upstream process**
Silver	1	g	market for silver | Cutoff, S - GLO
Argon	7.5	g	market for argon, liquid | Cutoff, S - RER
Electricity	41.7	Wh	market for electricity, medium voltage | Cutoff, S - SE/SK
Outputs			
AgNP(AP)	1	g	

A3.3 Magnesium production

As a part of the sensitivity analysis, a hypothetical replacement of the AgNPs with magnesium was explored. This was mentioned as a possibility by one of the consulted battery experts, and was proven to be a possibility by Yang et al (2019). To perform the sensitivity analysis, the AgNPs in the Ag-C separator layer were replaced with the Ecoinvent flow of magnesium as presented in Table A3.4.

***Table A3.4**: Unit process data results for magnesium production.*

Replacement flow			
Component/process	**Quantity**	**Unit**	**Linked upstream process**
Magnesium	0.0744	g	market for magnesium | Cutoff, S – GLO

4 Auxiliaries

A4.1 Nickel tab production

The pouch cell contains two small nickel (Ni) tabs that are ultrasonically welded onto the anode side of the battery cell (Lee et al. 2020) to provide a way to charge/discharge the battery cell. The production of the tabs was approximated in a similar manner as in Ellingsen (2014) with a metal input and a sheet rolling process. Nickel was available as input material in Ecoinvent v3.8. Since there was no specific sheet rolling process for nickel, aluminum sheet rolling was assumed to be a reasonable proxy. Template transport values were also included in the market processes. The summarized unit process data is presented in Table A4.1.

***Table A4.1**: Unit process data results for nickel tab production.*

Inputs normalized to unit process			
Component/process	**Quantity**	**Unit**	**Linked upstream process**
Nickel, class 1	1	g	market for nickel, class 1| Cutoff, S – GLO
Sheet rolling	1	g	market for sheet rolling, aluminum | Cutoff, S – GLO
Outputs			
Ni tab	1	g	

A4.2 Stainless steel foil production

The production process of the stainless steel (SUS) foil used as a current collector in the production process was modeled in a similar way as foil production was modeled by Ellingsen (2014) and Chordia et al. (2021), with a metal input and a sheet rolling process. The sheet rolling process includes the energy, waste, typical production scrap and emissions from the production. Template transport values were also included in the market processes. Data for both chromium steel and sheet rolling of steel were available in Ecoinvent v3.8. The unit process data is presented in Table A4.2.

***Table A4.2:** Unit process data results for SUS foil production*

Inputs normalized to unit process			
Component/process	**Quantity**	**Unit**	**Linked upstream process**
Chromium steel, hot rolled	1	g	market for steel, chromium steel 18/8, hot rolled | steel, chromium steel 18/8, hot rolled | Cutoff, S – GLO
Sheet rolling, steel	1	g	market for sheet rolling, steel | sheet rolling, steel | Cutoff, S – GLO
Outputs			
SUS foil	1	g	

A4.3 Aluminum foil/tab production

The aluminum foils used for the pouch bag, current collector and the tab used when charging/discharging the battery cell were all assumed to be similar enough to be modeled with the same unit process. The approach used in this study was similar to how aluminum foil production was modeled by Ellingsen (2014) and Chordia et al. (2021), with a metal input equal to the output and a sheet rolling process from Ecoinvent to approximate energy,

waste, typical production scrap losses and emissions. Template transport values were also included in the market processes. Both aluminum and sheet rolling of aluminum were available in Ecoinvent v3.8. The summarized unit process data is presented in Table A4.3.

Table A4.3: *Unit process data results for aluminum foil/tab production.*

Inputs normalized to unit process			
Component/process	**Quantity**	**Unit**	**Linked upstream process**
Aluminium, wrought alloy	1	g	market for aluminium, wrought alloy | Cutoff, S – GLO
Sheet rolling, aluminium	1	g	market for sheet rolling, aluminium | Cutoff, S – GLO
Outputs			
Aluminum foil/tab	1	g	

A4.4 Laminate bag

To protect the anode, catholyte and separator, the components are enclosed in a protective laminate bag with multiple layers. The dimensions of the bag were given by Lee et al. (2020) and the bag was assumed to be a standardized type as sold by the company MTI (MTI corporation, 2022). The mass of each component was then calculated from the densities of the materials, described in Section B1.6. The MTI specifications include two different types of adhesives, but since Ecoinvent dataset only exists for the polyurethane adhesive, that was considered a reasonable proxy also for the second type of adhesive. The summarized unit process data is presented in Table A4.4.

Similarly to Ellingsen (2014), the laminate bag was assumed to be produced with a combination of aluminum sheet rolling and injection molding. The sheet rolling energy, emissions and waste were included in the aluminum foil/tab unit process. See Section A4.3. Polypropylene, Nylon 6 and the adhesive were approximated to be manufactured with an injection molding process from Ecoinvent. The injection molding process includes energy, waste, emissions, and average transports. The energy for the lamination process was included in the pouch cell assembly, described in Appendix A5.

Table A4.4: *Unit process data results for the laminate bag production.*

Inputs normalized to unit process			
Component/process	**Quantity**	**Unit**	**Linked upstream process**
Nylon 6 (JIS Z1714)	0.330	g	market for nylon 6 |Cutoff, S - RER
Adhesive: polyurethane	0.0688	g	market for polyurethane adhesive | Cutoff, S - GLO
Aluminum foil	0.155	g	Aluminum foil/tab production (process B4.3)
Polypropylene	0.447	g	market for polypropylene, granulate | Cutoff, S - GLO
Injection molding	0.845	g	market for injection molding | Cutoff, S - GLO
Outputs			
Laminate bag	1	g	

A5 Pouch cell assembly

The assembly of the pouch cell starts with cutting of the main components (Ag-C separator layer, catholyte sheet and electrolyte sheet) using a punching machine before stacked and placed in a laminate bag. Vacuum is then applied to the laminate bag before sealing it. The prepared laminate bag is then pressurized using a warm isostatic press (WIP) at 490 MPa. After pressing, the prepared pouch cell is removed from the laminate bag and both the aluminum and nickel tabs are welded on to the cell using an ultrasonic welder, before packing the cell into another laminate bag and then sealing it. The majority of the process steps in the assembly were performed in dry air (Lee et al., 2020). The process of the assembly is presented in Figure A5.1.

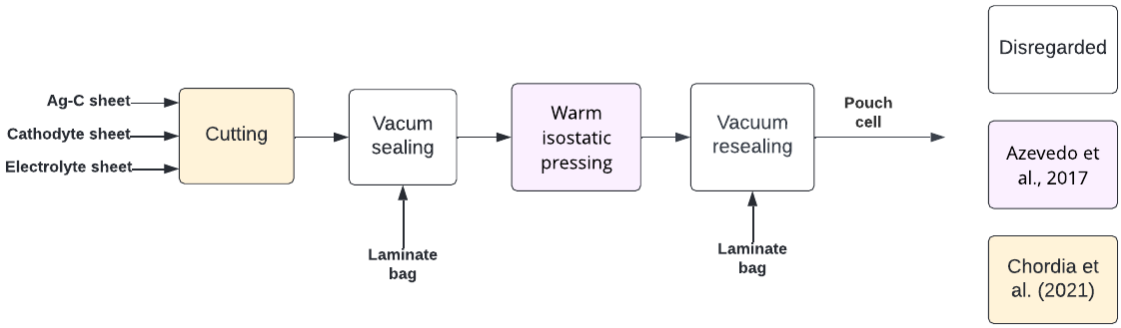

Figure A5.1: *Flowchart showing the pouch cell assembly process.*

Regarding the process energy, the ultrasonic welding was approximated using an arc welding process in Ecoinvent v3.8. The data in Ecoinvent is calculated using the length of the welding to calculate the energy, where the assumption of 0.8 cm/pouch cell was used, based on the geometry of the tabs.

The energy for cutting the pouch cell components was based on energy for cutting a NMC 811 cylindrical cell, received from the study by Chordia et al. (2021). For the pressing process, the process energy was calculated based on the energy requirement for hot isostatic pressing (HIP) of steel powder from Azevedo et al. (2017). This proxy was chosen as there was no information found on WIP processes for battery cells or recommendations for how the scaling from lab-scale to industrial scale should be done. Solid electrolytes usually require some sort of pressure application (calendaring) or temperature treatment (sintering) to increase the contact area between the electrolyte and cathode material (Schnell et al., 2018). Argyrodite electrolyte have the advantage that they can be pressed at room temperature (Sakuda et al., 2013), which is one reason why a pressing process and not sintering was chosen. The unit process data presented below is the total energy requirement for the assembly processes (cutting, pressing, and welding). Detailed figures regarding process energy are presented in Appendix C5, but the exact calculation figures were excluded due to confidentiality of the inventory data. The waste from the cutting process were not stated in Lee et al. (2020) and was therefore excluded.

The unit process data was normalized to the production of one pouch cell, and the input data comes from the previously described processes and the quantities of each product input were based on calculations of the pouch cell geometry as stated by Lee et al. (2020). The unit process data for assembly of the pouch cell is presented in Table A5.1. Detailed mass calculations are presented in Appendix B.

Table A5.1: *Unit process data results for pouch cell assembly.*

Inputs normalized to unit process			
Component/process	**Quantity**	**Unit**	**Linked upstream process**
Catholyte sheet	2.78	g	Catholyte sheet production (process A1)
Electrolyte sheet	0.516	g	Electrolyte sheet production (process A2)
Ag-C separator layer	1.118	g	Ag-C separator layer production (process A3)
Laminate bag	1.31	g	Laminate bag production (process A4.4)

Aluminum tab and current collector	0.205	g	Aluminum foil/tab production (process A4.3)
Nickel tab	0.356	g	Nickel tab production (process A4.1)
Welding	0.8	cm	market for welding, arc, aluminum | Cutoff, S - GLO
Electricity	2.74	Wh	market for electricity, medium voltage | Cutoff, S - SE/SK
Outputs			
1 pouch cell	1	Pouch cell	

A6 Support processes

A6.1 Wastewater treatment (waste flow)

The wastewater treatment process was modeled in the same way as in Chordia et al. (2021). The motivation for this was that approximately 95% of the wastewater generated in the production comes from the production of the active cathode material, which in this study is also modeled in the same way as Chordia et al. (2021). The process was modeled as being adjacent to the factory, the emission amounts were based on the highest allowed amounts in Sweden and the electricity is the estimated power required to reduce the emissions to those levels.

The unit process data results are presented in Table A6.1. Here, the reference flow is an input since the function of the unit process is to treat a waste flow (wastewater) rather than produce a product flow.

Table A6.1: Unit process data results for wastewater treatment.

Inputs normalized to unit process			
Component/process	**Quantity**	**Unit**	**Linked upstream process**
Wastewater, for treatment	1	g	
Electricity	3.32E-5	kWh	market for electricity, medium voltage | Cutoff, S - SE/SK
Emissions to water, normalized to unit process			
Ammonium nitrate	3.8E-8	g	Emission to water/ground water
Cobalt	1.9E-11	g	Emission to water/ground water
Flouride	1.08E-14	g	Emission to water/ground water
Hydrogen fluoride	4.15E-14	g	Emission to water/ground water
Lithium	1.9E-10	g	Emission to water/ground water
Methyl ethyl ketone	4.40E-13	g	Emission to water/ground water
Nickel	1.9E-11	g	Emission to water/ground water
Phosphate	3.94E-14	g	Emission to water/ground water
Sodium ion	6.15E-7	g	Emission to water/ground water
Sulfate, ion	1.28E-6	g	Emission to water/ground water
Returned resource, normalized to unit process			
Water	1	g	Returned

A6.2 Scrap transport

This process represents burdens from the transport of recyclable production scrap to a recycling facility. The numbers were based on a similar process from Chordia et al. (2021). Table A6.2 summarizes the unit process data.

Table A6.2: Unit process data results for scrap transport.

Inputs normalized to unit process			
Component/process	**Quantity**	**Unit**	**Linked upstream process**
Transport, train	0.0112	ton*km	market group for transport, freight train | Cutoff, S - GLO
Transport, lorry	0.0193	ton*km	market group for transport, freight, lorry, unspecified | Cutoff, S - GLO
Outputs			
Recycling transport	1	kg	

A6.3 Swedish heat production

The Swedish heat production was modeled in the same way as in Chordia et al. (2021), who used numbers from a report from the Swedish Energy Agency (SEA, 2020) to derive a heating mix that would be likely for industrial usage in Sweden. The linked flows "heat, air-water heat pump 10kW -SE" and "heat production, wood pellet, at furnace 9kW, state-of-the-art 2014 -SE" have been adapted from the Swiss versions of those processes by replacing the energy inputs with the Swedish electricity mix. The result of the unit process data is presented in Table A6.3.

Table A6.3: *Unit process data results for Swedish heat production.*

Inputs normalized to unit process			
Component/process	**Quantity**	**Unit**	**Linked upstream process**
heat, air-water heat pump 10kW	0.0717	MJ	heat, air-water heat pump 10kW |Cutoff, S -SE
heat, central or small-scale, other than natural gas	0.0723	MJ	heat production, wood pellet, at furnace 9kW, state-of-the-art 2014 |Cutoff, S -SE
heat, district or industrial, natural gas	0.0212	MJ	heat and power co-generation, natural gas, conventional power plant, 100MW electrical|Cutoff, S - SE
heat, district or industrial, other than natural gas	0.119	MJ	heat, from municipal waste incineration to generic market for heat district or industrial, other than natural gas | Cutoff, S - SE
heat, district or industrial, other than natural gas	0.152	MJ	heat, from municipal waste incineration to generic market for heat district or industrial, other than natural gas | Cutoff, S - SE
heat, district or industrial, other than natural gas	0.0174	MJ	heat and power co-generation, oil| Cutoff, S - SE
heat, district or industrial, other than natural gas	0.427	MJ	heat and power co-generation, wood chips, 6667 kW, state-of-the-art 2014 | Cutoff, S - SE
heat, district or industrial, other than natural gas	0.0367	MJ	treatment of blast furnace gas, in power plant | Cutoff, S - SE
Heat, electric emersion heater	0.0035	MJ	Electricity, medium voltage
heat, excess	0.0789	MJ	Excess industrial heat, process B6.3.1
Outputs			
Swedish industrial heat	1	MJ	

A6.3.1 Excess industrial heat production

This process corresponds to excess process heat being reused within the factory. This was approximated by a process that only has one output and zero inputs, since the reuse of heat could be considered nearly burden-free. The Table A6.4 presents the unit process data results for the process.

Table A6.4: *Unit process data results for excess industrial heat.*

Inputs normalized to unit process			
Component/process	**Quantity**	**Unit**	**Linked upstream process**

Outputs			
Excess heat	1	MJ	

A6.4 Swedish cooling

As there were no Swedish provider for the Ecoinvent 3.8 flow called "*cooling energy, from natural gas, at cogen unit with absorption chiller 100kW | cooling energy | Cutoff, S*", the flow was modified in two ways to make it representative for Swedish cooling production. Firstly, all electricity providers were changed to Swedish electricity mix. Secondly, the heat providers were changed to the Swedish heat production as described in Section A6.3. This is the same approach as was used by Chordia et al. (2021).

A7 Factory construction and operations

As the LCA was prospective and no specific factory exists, the inventory data for the factory building and operations were based on data from the LCA by Chordia et al (2021), who modeled an upscaled version of a LIB cell factory.

The inventory data for this unit process consisted mainly of three components: the building of the factory and the machines, energy usage from the operating of dry rooms and energy use for daily factory operations such as ventilation, control systems, tool use, lighting, and the running of other equipment in the building. The summarized unit process data is presented in Table A7.1.

Table A7.1: *Unit process data results for factory construction and operations.*

Inputs normalized to unit process			
Component/process	**Quantity**	**Unit**	**Linked upstream process**
Electronic component factory	0.056	electronics factory	market for electronic component factory | Cutoff, S - GLO
Precious metal refinery	0.6	metal factory	market for precious metal refinery | Cutoff, S - GLO
Electricity	230	GWh	market for electricity, medium voltage | Cutoff, S - SE/SK
Heating	1.93E+5	GJ	Swedish heat production (A6.3) / market for heat, district or industrial, natural gas | Cutoff, S - RoW
Cooling	2.46E+5	GJ	cooling energy, from natural gas, at cogen unit with absorption chiller 100kW| Cutoff, S - SE/ROW
Outputs			
Operating factory	1	years of factory operation	

A7.1 Factory construction

The building of the factory and machines were approximated with Ecoinvent data for building an electronic component factory and a precious metal refinery. In line with how the factory was modeled by Chordia et al. (2021), an assumption was made that the battery cell factory can be approximated as consisting of around 80% electronics factory and 20% precious metal refinery. Furthermore, it was assumed that the factory would operate

for 25 years. Since the factory items in Ecoinvent covers a specific area, the data for those items needed to be scaled to the size of the studied battery cell factory. Details of this are presented in Table A7.2.

Table A7.2: Unit process data results for factory construction.

Factory type	**Value**	**Unit**
Total space occupied	150 000	m^2
Electronics factory	120 000	m^2
Precious metal refinery	30 000	m^2
Ecoinvent item	**Value**	**Unit**
Electronics factory	85 587	m^2 / factory
Precious metal refinery	2 000	m^2 / factory
Factory ratio	**Value**	**Unit**
Electronics factory (existing for 25 years)	1.4	Ecoinvent factory/ battery factory
Precious metal refinery (existing for 25 years)	15	Ecoinvent factory/ battery factory
Annual factory burden	**Value**	**Unit**
Electronics factory	0.056	Ecoinvent factory/ year of operation
Precious metal refinery	0.6	Ecoinvent factory/ year of operation

A7.2 Dry rooms and miscellaneous factory operations

The factory operations include operating dry rooms as well as a small amount of energy required for heating, cooling, lighting and ventilating the factory. The dry room energy was estimated by data from Deng et al. (2017), who modeled energy use for a scaled-up version of an industrial dry room. The dry room modeled by Deng et al. (2017) was capable of maintaining 21°C at 100 ppm moisture content, which corresponds to a dewpoint of about -42 °C. This was deemed close enough to Lee et al. (2020) recommendation of a dewpoint of -50C. The process is shown in Figure A7.1.

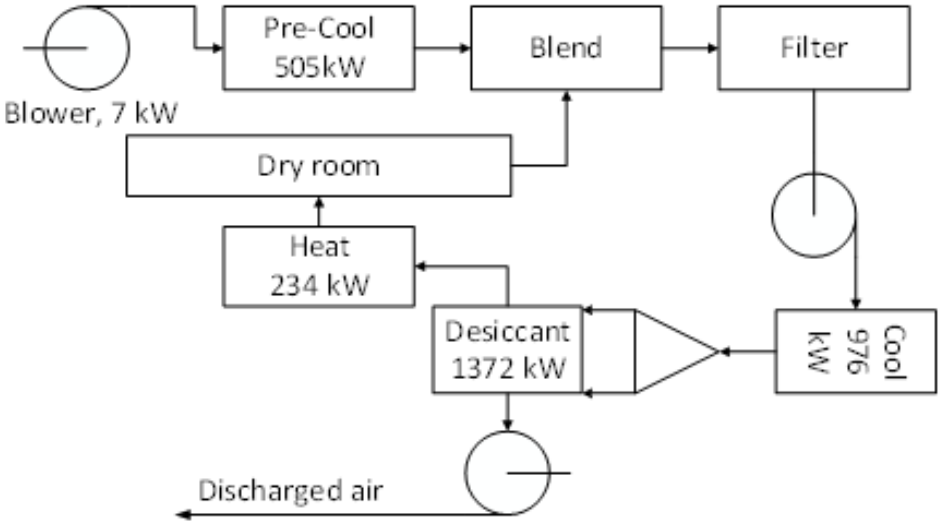

Figure A7.1: *Schematic dry room setup. Obtained from Deng et al. (2017) supplementary information under license nr: 5334081333438.*

The dry room modeled by Deng et al. (2017) covered 4000 m^2 and required an average power of 0.51 kW/m^2 to operate. These values together with some further assumptions allowed a dry room energy to be estimated, see Appendix C5 for the details on the energy use calculation.

For the miscellaneous energy for the factory operations, data from Chordia et al. (2021) was used. In their work, they provide aggregated numbers for dry rooms and miscellaneous energy. With help of unpublished and confidential data from Chordia et al. (2021), this data was disaggregated and combined with the dry-room energy modeling from this study, which is the numbers presented in the unit process B7.

A8 Storage capacity generation

This unit process does not correspond to any physical process within or outside the factory. Instead, its function is to connect the amount of pouch cells and the fraction of factory building and operations required to produce 1 kWh of theoretical storage capacity, i.e. the defined functional unit. The share of factory operations was calculated by dividing the 1 kWh functional unit with the assumed annual production capacity (16 GWh) of the factory. The summarized unit process is presented in Table A8.1.

The amount of pouch cell required was then calculated with the formula:

$$Cells\ required = \frac{FU\ capacity}{Pouch\ cell\ capacity}$$

where the FU capacity was 1 kWh and the pouch cell capacity was 2.4064 Wh. The details on how the pouch cell capacity has been calculated can be found in Section 3.2.

Table A8.1: *Unit process data results for storage capacity generation.*

Inputs normalized to unit process			
Component/process	**Quantity**	**Unit**	**Linked upstream process**
Operating battery factory	6.25E-8	factory operation	Factory construction and operations (process A7)
Formed cell	416	pouch cells	Pouch cell assembly (process A5)
Outputs			
Battery cell theoretical storage capacity	1	kWh	Functional unit

Appendix B

Volume and mass calculations

This appendix includes detailed geometrical calculations (B1), mass balancing (B2) and a summary (B3).

B1 Geometrical calculations

The geometry of each component was estimated and calculated based on the article by Lee et al. (2020). This section includes the layer volume calculations using geometric descriptions. The following abbreviations were used:

$$\begin{aligned} \mathrm{V} &= \text{volume} \\ \mathrm{m} &= \text{mass} \\ \mathrm{d} &= \text{density} \end{aligned}$$

B1.1 Catholyte sheet

The catholyte has a total thickness of 95-105 µm, placed on both sides of the aluminum current collector. In this study, we assumed the maximum thickness, resulting in a total thickness of 210 µm. The area of the cathode layer was presented to be 53 mm × 88 mm according to Lee et al. (2020) and was used to calculate the catholyte sheet volume:

$$V_{catholyte} = 0.021 * 5.3 * 8.8\ cm = 0.979\ cm^3$$

The catholyte consists of four components: LZO-coated NMC 811(LZO/NMC), argyrodite powder (SSEp), CNF and polytetrafluoroethylene (PTFE). These were mixed with a ratio of 85:15:3:1.5 by weight, shown in Table B1.1. To calculate the mass of the catholyte, in a first step, the mass of each component was calculated with the following system equation:

$$V_{catholyte} = V1 + V2 + V3 + V4 = (85/105) * m_{catholyte} / d_{catholyte}$$

Using each components density (see table B1.1), the volumes were calculated as:

$$\begin{aligned} V1 = V_{LZO/NMC} &= (85/105) * m_{catholyte}/3.4\ g/cm^3 \\ V2 = V_{SSE} &= (15/105) * m_{catholyte}/1.64\ g/cm^3 \\ V3 = V_{CNF} &= (3/105) * m_{catholyte}/1.5\ g/cm^3 \\ V4 = V_{PTFE} &= (1.5/105) * m_{catholyte}/2.16\ g/cm^3 \end{aligned}$$

The mass of each component was then calculated by first calculating $m_{catholyte}$ based on the total volume $V_{catholyte}$ and the total density, resulting in 2.78 g. The masses of the components were:

$$\begin{aligned} m_{LZO/NMC} &= 2.26\ g \\ m_{SEE} &= 0.399\ g \\ m_{CNF} &= 0.0798\ g \\ m_{PTFE} &= 0.0399\ g \end{aligned}$$

Table B1.1: *Data input and result for calculation of catholyte sheet geometry and mass.*

Catholyte sheet				
Material layer	**Density [g/cm³]**	**Mixing ratio [wt]**	**Weight [g]**	**Density reference**
LZO/NMC 811	3.4	85	2.26	MSE Supplies. (2022)
SSE	1.64	15	0.399	Zhou et al. (2018), supplementary information
CNF	1.5	3	0.0798	Burton et al. (n.d.)
PTFE	2.16	1.5	0.0399	Aetna Plastics Corp. (n.d.)

B1.2 Electrolyte sheet

The electrolyte sheet thickness was reduced to 30 μm after pressurization, and in the pouch cell, there is one layer of SSE sheet on each side, resulting in a total thickness of 60 μm. The size of the SEE sheet is 57 mm × 92 mm (Lee et al., 2020), used to calculate the total volume:

$$V_{SSE} = 0.006 * 5.7 * 9.2\ cm = 0.315\ cm^3$$

The SSE sheet consists of the solid electrolyte Li_6PS_5Cl and a non-aqueous acrylate-type binder with the weight ratio 99:1. The weight was therefore first calculated using the theoretical density of Li_6PS_5Cl (see Table B1.2).

$$m_{Li6PS5Cl} = (1.64\ g/cm^3 * 0.315\ cm^3) * 99/100 = 0.51085\ g$$

$$m_{binder} = 0.511\ g\ /\ 99 = 0.00516\ g$$

The mass of the SSE sheet was calculated as the sum of the Li_6PS_5Cl and the binder:

$$m_{SEE} = 0.511 + 0.00516\ g = 0.516\ g$$

Table B1.2: *Data input and result for calculation of electrolyte sheet geometry and mass.*

Electrolyte Sheet size				
Material layer	**Density [g/cm³]**	**Mixing ratio [wt]**	**Weight [g]**	**Density reference**
Li_6PS_5Cl	1.64	99	0.511	Zhou et al. (2018), Supplementary information
Non-aqueous acrylate-type binder	-	1	0.00516	-

B1.3 Ag-C separator layer

The Ag-C separator layer had a thickness of 5–10 μm, on each side of the aluminum current collector. In this study, we assumed an Ag-C separator layer using maximum thickness, resulting in a total of 20 μm for both sides. The area of the Ag-C separator layer is 55 mm × 90 mm (Lee et al., 2020) and this was used to calculate the volume:

$$V_{Ag\text{-}C} = 0.002 * 5.5 * 9\ cm = 0.099\ cm^3$$

The weight of the Ag-C separator layer was further calculated by the materials that the Ag-C separator layer is composed of, which is AgNPs and carbon black at a weight ratio of 1:3. It was further reported in Lee et al. (2020) that the silver occupied 8% of the volume of the final composite.

$$V_{Ag} = 0.099\ cm^3 * 0.08 = 0.00792\ cm^3$$

The mass of the silver was then calculated from the density of silver (see TableB1.3):

$$m_{Ag} = 0.00792\ cm^3 * 10.5\ g/cm^3 = 0.0832\ g$$

The mass of carbon black was then calculated using the weight ratio between the silver and carbon black as given in Lee et al. (2020):

$$m_{CB} = 0.0832\ g * 3 = 0.249\ g$$

The Ag-C is mixed with a N-methylpyrrolidone (NMP) solvent containing 7wt% of polyvinylidene fluoride (PVDF). The solvent is not part of the final product, but the PVDF is assumed to act as a binder, which has to be added to the weight of the Ag-C separator layer. There was no information about the amount of solvent and binder that was used in the preparation, but an estimation of 1 wt% of binder in the final composite was assumed:

$$m_{PVDF} = (0.0832 + 0.249\ g) / 99 = 0.00336\ g$$

The amount of NMP solvent used was then calculated based on the ratio between the PVDF and solvent. First the mass of PVDF is divided by 7 to get the weight of 1%, that number is then multiplied with 93 to get the weight for 93%, which is the weight of the solvent:

$$m_{NMP} = (0.00336/7)*93 = 0.0446\ g$$

The total mass of the Ag-C separator layer was calculated summing the materials together:

$$m_{Ag\text{-}C} = 0.0832 + 0.249 + 0.00336\ g = 0.336\ g$$

Table B1.3: *Data input and result for calculation of Ag-C separator layer geometry and mass.*

Ag-C separator layer					
Material layer	**Sub layer**	**Density [g/cm³]**	**Mixing ratio [wt]**	**Weight [g]**	**Density reference**
Ag-C	AgNPs	10.50	1 (Ag:C)	0.0832	SkySpring (2022)
	Carbon black	2.10	3 (Ag:C)	0.249	Flexicon (n.d.)
NMP	-	-	93 (solvent:binder)	0.0446	-
PVDF	-	1.78	7 (solvent:binder)	0.00336	Lorric (2022)

B1.4 SUS foil

The SUS foil had a thickness of 10 µm, placed on both sides of the aluminum current collector. The size of the SUS foil was not stated in Lee et al. (2020) and was therefore assumed to be the same size as the Ag-C separator layer, as they were assembled in the same step. The volume was therefore calculated as:

$$V_{SUS\ foil} = 0.002 * 5.5 * 9 = 0.099\ cm^3$$

The mass was then calculated using the density of SUS current collectors:

$$m_{SUS\ foil} = 0.099\ cm^3 * 7.9\ g/cm^3 = 0.78\ g$$

B1.5 Aluminum foil

The aluminum foil is used at the center of the battery cell and has a thickness of 12 μm. The aluminum foil size was not specified in Lee et al. (2020) and was therefore assumed to be the size of the catholyte layer, as the catholyte is in direct contact with the aluminum foil core. The volume was calculated as:

$$V_{Al\ foil} = 0.0012 * 5.3\ x\ 8.8\ cm = 0.056\ cm^3$$

The mass was then calculated using the density of aluminum current collectors:

$$m_{Al\ foil} = 0.056\ cm^3 * 2.7\ g/cm^3 = 0.15\ g$$

B1.6 Pouch bag

The pouch bag consists of two laminate films, each with a thickness of 120 μm. The size of the pouch bag is 67 mm × 112 mm (Lee et al., 2020), which was used to calculate the total volume:

$$V_{Pouch\ bag} = 0.024 * 6.7 * 11.2\ cm = 1.80\ cm^3$$

The material composition of the laminate bag that the pouch cell is composed of was not specified more than that it is an "aluminum-laminate". To estimate the weight of the pouch cell components, the material composition and thickness was adapted from MTI (2022). The materials included Nylon 6, polyurethane adhesive, aluminum foil and polypropylene (Table B1.4). Both types of adhesives used in the pouch cell were approximated as a single adhesive.

Table B1.4: *Data input and result for calculation of pouch bag geometry and mass.*

Ag–C separator layer				
Material layer	**Density [g/cm^3]**	**Thickness [μm]**	**Weight [g]**	**Density reference**
Nylon 6	1.14	25	0.431	Estes and Schweizer (2011)
Polyurethane adhesive	1.2	5	0.0900	Burchardt and Merz (2006)
Aluminum foil	2.7	43	0.203	Zhu et al., (2021)
Polypropylene	0.906	47	0.586	INEOS (n.d.)

B2. Reactions and mass balances

This appendix presents the mass balance calculations. At the end of the appendix, a summary of the calculation results for the layer volume and mass are found.

B2.1 LZO coating solution

The amount of LZO coating solution resulting from the mixing was calculated based on simplified stoichiometry, using the molar ratio 20:1:200 of lithium methoxide (10% lithium methoxide in a methanol solution), zirconium(IV) tetrapropoxide and anhydrous 2-propanol solvent as reported in Lee et al. (2020). The results can be seen in Table B2.1.

Table B2.1: *Data input for LZO coating solution mass calculation.*

LZO solution			
Substance	**Chemical Formula**	**Molar mass [g/mol]**	**Reference**
Lithium	Li	6.94	Rumble (2021)
Oxygen	O	16	Rumble (2021)
Zirconium	Zr	91.2	Rumble (2021)
Carbon	C	12	Rumble (2021)
Lithium methoxide	$LiCH_3O$	38*	-
Methanol	CH_3OH	32*	-
Zirconium (IV) tetrapropoxide:	Zr(OC3H7)4	328*	-
2-propanol	$(CH_3)_2CHOH$	60.1*	-
LZO solution	Li2O-ZrO2	153*	-
Lithium methoxide (10% in methanol)	$LiCH_3O + CH_3OH$	32.6**	-

*Calculated based on stoichiometry
**Mean value calculated based on 10% lithium methoxide in methanol solution

The reaction was written as an unbalanced and simplified stochiometric reaction, assuming the zirconium as a limiting substance, and a 100% reaction yield:

$$20\ (LiCH_3O\ (10\%)\ + CH_3OH) + 1\ Zr(OC_3H_7)_4 + 200\ (CH_3)_2CHOH \rightarrow X\ Li_2O\text{–}ZrO_2 + extra\ solvent$$

Based on the balancing of the formula, the solution can only yield one mol of LZO coating solution, as lithium and zirconium become limiting substances. This gives:

$$X = 1\ mol\ Li_2O\text{–}ZrO_2$$

The amount of LZO coating from the above reaction was then calculated using the molar mass of $Li_2O\text{–}ZrO_2$ (see table B2.1).

$$1\ mol * 153\ g/mol = 153\ g\ Li2O\text{–}ZrO2$$

The quantitative input of each reactant to achieve 153 g *Li2O–ZrO2* was calculated using the amount of mol put into the reaction and the molar mass of each.

$$LiCH_3O\ (10\%) + CH_3OH: 20*32.6/\ (20*32.6 + 1*328 + 200*60.1) = 0.0502\ g$$

$$Zr(OC_3H_7)_4: 1*328/\ (20*32.6 + 1*328 + 200*60.1) = 0.0252\ g$$

$$(CH_3)_2CHOH: 200*60.1/\ (20*32.6 + 1*328 + 200*60.1) = 0.925\ g$$

B2.1.1 Lithium methoxide

This process includes the mixing of 15 kg lithium and 900 kg of methanol (Cao, 2008). The calculations were based on stoichiometry with an assumption of 100% yield, with only hydrogen gas as excess product. Data used are presented in Table B2.1. The reaction of lithium and methanol to produce lithium methoxide was assumed according to the following unbalanced and simplified stochiometric reaction formula:

$$Li + CH_3OH => LiCH_3O + CH_3OH + H_2$$

The reaction was calculated with the input quantities as reported by Cao (2008), where the amounts of different products are unknown:

$$15\ kg\ Li + 900\ kg\ CH_3OH => X\ kg\ LiCH_3O + Y\ kg\ CH_3OH + Z\ kg\ H_2$$

The amount of mol of lithium added to the process was calculated using the molar mass of lithium:

$$15\ kg\ Li = 15\ 000\ g\ /\ 6.94\ g/mol = 2160\ mol$$

Lithium was assumed to be the limiting substance in the formation of lithium methoxide, meaning that 1 mol of lithium equals 1 mol of lithium methoxide. The mass of lithium methoxide was calculated using its molar mass:

$$X = 2160\ mol\ LiCH_3O\ x\ 38\ g/mol = 82.1\ kg\ LiCH_3O$$

The amount of mol of methanol used in the production process was calculated by the molar mass of methanol and the mass of input:

$$Mol\ CH_3OH = 900\ 000\ g\ /\ 32\ g/mol = 28\ 100\ mol$$

According to the formula, 1 mol of methanol is required in the formation of 1 mol lithium methoxide (with the excess of a hydrogen atom). It was assumed that 2160 mol methanol reacts to form lithium methoxide, and the remaining fraction remains as excess methanol solution.

$$Excess\ CH_3OH:\ 28\ 100\ mol\ -\ 2160\ mol = 25\ 900\ mol$$

The mass of the excess methanol was calculated based on the molar mass of methanol as follows:

$$Y = 25\ 900\ mol\ *\ 32\ g/\ mol = 831\ kg\ of\ methanol$$

In the reaction, an excess of hydrogen is likely to form, with the same amount of mol as the lithium methoxide solution according to the reaction formula (or half the amount of mol hydrogen gas, H_2):

$$Mol\ H = 2160\ mol\ *\ 1.01\ g/mol = 2.18\ kg$$

As input material in the process of producing the argyrodite battery cell, the desired product is 10% lithium methoxide in methanol solution. The solution created from the reaction formula here was calculated to be approximately 9% of the product (excl. hydrogen gas):

$$82.1/913kg = 0.0899 = 8.9\%$$

B2.1.2 Zirconium (IV) tetrapropoxide

The amount of zirconium needed was based on simplified stoichiometry, where it was assumed that 1 mol of zirconium was needed in the formation of 1 mol of zirconium tetrapropoxide.

$$1\ mol\ Zr => 1\ mol\ Zr(OC_3H7)_4$$

The mass of zirconium required was calculated based on the weight ratio using the molecular mass of both zirconium and zirconium (IV) tetrapropoxide:

$$91.2\ g\ Zr\ /328\ g\ Zr(OC_3H_7)_4 = 0.278$$

B2.2 Sol-gel coating

The amount of LZO used to coat the NMC 811 cathode was not reported in Lee et al. (2020). The proportions were instead estimated based on a similar process from Ito et al. (2014), where a LZO solution was used to coat a

NCA cathode, creating a 6-8 nm thick coating, which is similar to the thickness in Lee et al. (2020). As the molar mass of NMC and NCA were similar (see Table B2.2), the same molar ratio with the LZO coating was assumed.

Table B2.2: *data input for mass calculation of LZO coated NMC cathode*

LZO NMC cathode			
Substance	**Chemical formula**	**Molar mass [g/mol]**	**Reference**
Lithium	Li	6.94	Rumble (2021)
Nickel	Ni	58.7	Rumble (2021)
Cobalt	Co	58.9	Rumble (2021)
Magnesium	Mn	54.9	Rumble (2021)
Aluminum	Al	27	Rumble (2021)
Oxygen	O	16	Rumble (2021)
LZO solution	Li_2O-ZrO_2	153*	-
NMC 8:1:1	$LiNi_{0.8}Co_{0.10}Mn_{0.10}O_2$	97.3*	-
NCA	$LiNi_{0.8}Co_{0.15}Al_{0.05}O_2$	96.1*	-

*Calculated based on the chemical formula

The amount of LZO coating and NMC 811 needed were calculated with data from Table B2.2 and the molar fraction between LZO and NMC 811, being 0.5:99.5.

$$LZO: 0.5\ mol * 153\ g/mol = 76.6\ g$$
$$NMC\ 8:1:1 = 99.5\ mol * 97.3\ g/mol = 9680\ g$$

The total amount of each input to produce 1 g of coated NMC 811 was then calculated by dividing each component with 9760 g of finished product.

$$LZO: 76.6\ g / 9760\ g = 0.0078\ g$$
$$NMC\ 811: 9680\ g / 9760\ g = 0.99\ g$$

As the quantitative LZO input is based on the dry weight needed to achieve the right ratio in the finished product, the quantitative input of LZO solution is higher, as the liquid solvents used are evaporated before obtaining the final product. The amount of LZO solution needed was therefore assumed by calculating the amount of solution needed to achieve the desired end-product ratio. This was done by adding the LZO of 0.0078 g and the ratio of liquid mass to dry mass. The liquid mass being 90% of the lithium methoxide solution and the propanol, and the dry mass 10% of the lithium methoxide solution and the zirconium (IV) tetrapropoxide:

$$LZO\ (dry\ fraction) * (liquid\ mass/dry\ mass) = 0.0078\ g * (0.9 * m_{lithiummetoxid} + m_{propanol}) / (0.1 * m_{lithiummetoxid} + m_{zirconiumtetraproxid}) = 0.25\ g$$

B2.3 Electrolyte powder

The amounts of input from each of component in the electrolyte powder were calculated based on balancing the reaction with stoichiometric proportions:

$$5\ Li_2S + P_2S_5 + 2\ LiCl => 2\ Li_6PS_5Cl$$

The amount input of each of these components were then based on the molecular weight presented in Table B2.3:

$$Li_2S: 45.9\ g\ /\ mol * 5\ mol = 229\ g$$
$$P_2S_5: 222\ g/mol * 1\ mol = 222\ g$$
$$LiCl: 42.4\ g/mol * 2\ mol = 84.8\ g$$
$$Li_6PS_5Cl: 268\ g/mol * 2\ mol = 537\ g$$

The amount of each component needed for the production of 1 g Li_6PS_5Cl were then calculated by dividing by the weight of Li_6PS_5Cl for all components.

Table B2.3: *Data input for calculation electrolyte powder mass.*

Electrolyte powder			
Substance	**Chemical formula**	**Molar mass [g/mol]**	**Reference**
Lithium	Li	6.94	Rumble (2021)
Sulfur	S	32.1	Rumble (2021)
Hydrogen	H	1.01	Rumble (2021)
Phosphorus	P	31	Rumble (2021)
Chlorine	Cl	35.5	Rumble (2021)
Lithium sulfide	Li_2S	45.9*	-
Phosphorus pentasulfide	P_2S_5	222*	-
Lithium chloride	LiCl	42.4*	-
Argyrodite powder	Li_6PS_5Cl	268*	-

*Calculated based on the chemical formula

B2.3.1 Lithium sulfide

The mass of lithium sulfide was calculated based on a patent by Chu et al. (2015), presenting a synthesis of lithium sulfide using 0.32 g sulfur powder and 0.16 g of lithium hydride, using data from Table B2.3. The resulting amount of lithium sulfide from the production process was calculated using stoichiometry. The amount of mol of each substance was calculated based on the mass and the molar mass:

$$Sulfur: 0.32\ g/32.065\ g/mol = 0.0099\ mol$$

$$Lithium\ hydride: 0.16\ g/\ (6.94 + 1.01)\ g/mol = 0.0201\ mol$$

The molar ratio between lithium and sulfur is approximately 2:1, and the reaction with the given mass input can therefore be written as:

$$0.01\ S + 0.02\ LiH => 0.01\ Li_2S + 0.01\ H_2$$

As the proportions of input between lithium and sulfur is in accordance with the molar ratio of lithium sulfide, it is assumed that only hydrogen gas is produced besides the product of lithium sulfide. The resulting mass of Li_2S is therefore:

$$45.9\ g/mol * 0.01\ mol = 0.459\ g$$

B2.3.1.3 Lithium hydride

The reaction of lithium metal with hydrogen gas forms lithium hydride, with the following stoichiometric reaction:

$$2\ Li + H_2 => 2\ LiH$$

With data from Table A2.2, the masses were calculated as follows:

$$m(2\ Li) = 2 * 6.94 = 13.9\ g$$
$$m(H_2) = 1.01 * 2 = 2.02\ g$$
$$m(2\ LiH) = (6.94+1.01) * 2 = 15.9\ g$$

The two input substances were then normalized to the production of 1 kg LiH.

B2.3.2 Phosphorus pentasulfide

Phosphorus pentasulfide was calculated using a simple production method from Chemeuroupe (n.d), in which phosphorus and sulfide is heated above 300°C to produce the desired product. The mass was calculated based on stoichiometric proportions:

$$2\ P + 5\ S => P_2S_5$$

Input masses were calculated using the molar mass of each substance, found in Table B2.3.

B3 Layer geometry and mass summary

Table B3.1 presents a summary of the component mass and volume, presented on both component and material level.

Table B3.1: *Summary of layer masses and volumes.*

Mass and Volume of 1 pouch cell			
Layer	**Sub-layer**	**Weight [g]**	**Volume [cm^3]**
Ag-C separator		1.118*	0.099
	AgNPs	0.0832	0.00792
	Carbon black	0.249	0.119
	NMP	0.0446	-
	PVDF	0.00336	-
Electrolyte sheet		0.516	0.315
	Li_6PS_5Cl	0.511	-
	Non-aqueous acrylate-type binder	0.00516	-
Catholyte sheet		2.78	0.979
	LZO/NMC 811	2.26	-
	SSE	0.399	-
	CNF	0.0798	-
	PTFE	0.0399	-
Pouch bag		1.3088	1.80
Auxiliaries			
	SUS foil	0.782	0.09
	Aluminum foil + tab	0.205	0.0760
	Nickel tab	0.356	0.04

*Includes the weight of the SUS foil

Appendix C

Detailed energy calculations

For many processes in the studied system, the energy requirement had to be calculated since no primary data can exist for a hypothetical production system. In each table heading, the process and name as described in Lee et al. (2020), and presented in Appendix A, is presented first without brackets. The scaled up process, which has been used to calculate the energy requirements, is then shown within brackets in the table headers. Most of the calculations were performed based on data from the framework by Piccinno et al. (2016). All the energy calculations and assumptions are presented in detail below.

C1. Catholyte sheet

The preparation of the catholyte sheet, described in Appendix B, is divided into preparation of the LZO-coated NMC and the sol-gel coating. Detailed process energy calculations are presented below.

C1.1 LZO coating

The process used to prepare the LZO coating solution was, based on Lee et al. (2020), assumed to be simple mixing of lithium methoxide and zirconium(IV) tetrapropoxide in anhydrous 2-propanol. The mixing process was scaled using the stirring energy (E_{stir}) equation from Piccinno et al. (2016), with symbols as shown in Table C1.1:

$$E_{stir} = \frac{N_p * \rho_{mix} * N^3 * d^5 * t}{\eta_{stir}}$$

Table C1.1: *Data for calculating the mixing of the input materials of the LZO solution.*

Mixing (Stirring energy)				
Parameter	**Description**	**Value**	**Unit**	**Reference**
N_p	Power number of impeller	0.79	-	Piccinno et al. (2016)
ρ_{mix}	Density for the mix	798*	kg/m^3	-
N	Rotational speed	1.42	-	Piccinno et al. (2016)
d	Impeller diameter	0.373	m	Piccinno et al. (2016)
t	Time	1	h	Assumed Lee et al. (2020)
η_{stir}	Efficiency of agitator	0.9	-	Piccinno et al. (2016)
$V_{reactor}$	Volume of reactor	1	m^3	-

*The mean density of the mixture was calculated using the density of each material input with a weight ratio based on molar weight and ratios of input. $(m_{Lithium\ Methoxide}/m_{total})) * \rho_{Lithium\ methoxide} + (m_{Zirconum}/m_{tota} * \rho_{Zirconium} + (m_{propanol}/m_{tota})) * \rho_{propanol}$

Using the data from Table C1.1 in the stirring energy equation resulted in the following energy requirement, calculated for the output of 1 kg of LZO solution mixture:

$$E_{stir} = 15.1\ J/kg = 0.00420\ Wh/kg$$

C1.2 Sol-gel coating

The sol-gel coating consists of mixing, vacuum drying with sonication, filtration, and heating, seen in Appendix A1.2. Below, the total processes energy consumption was calculated, normalized to 1 kg of dry product output,

which is LZO-coated NMC 811. The energy requirements for the initial 1 h mixing of LZO coating and NMC 811 powder was calculated based on stirring energy equation from Piccinno et al. (2016), shown in Section C1.1.

***Table C1.2**: Dispersion of NMC 811 in LZO solution.*

Sol-gel mixing (Stirring energy)				
Parameter	**Description**	**Value**	**Unit**	**Reference**
N_p	Power number of impeller	0.79	-	Piccinno et al. (2016)
ρ_{mix}	Density for the mix	3380*	kg/m^3	Calculated
N	Rotational speed	1.42	-	Piccinno e al. (2016)
d	Impeller diameter	0.373	m	Piccinno et al. (2016)
t	Time	3600	s	Lee et al. (2020)
η_{stir}	Efficiency of agitator	0.9	-	Piccinno et al. (2016)
$V_{reactor}$	Reactor volume	1	m^3	-
m_{dry}	Dry output	3370**	kg	-

*Mean density of the mixture ($\rho_{LZOsolution}$ * share LZO solution + ρ_{NMC811} * share NMC 811)
**Quantities of LZO coated NMC 811 (excl. solvents)

Using data from Table C1.2 in the stirring energy equation resulted in the following energy requirement:

$$E_{stir} = 65.030\ J/kg = 0.018\ Wh/kg\ LZO\text{-}coated\ NMC\ 811$$

The second process step, the energy requirement for vacuum drying with sonication was calculated using the processes distillation as described by Capello et al. (2005), with additional energy for sonication, calculated by stirring energy as presented by Piccinno et al. (2016). The distillation equations from Capello et al. (2005) for electricity (E_{dist}) and for heating (Q_{dis}) is shown below, with symbols shown in Table C1.3.

$$E_{dist} = E * m_{solv}$$
$$Q_{dist} = C_{heat} * m_{steam} * m_{solv}$$

***Table C1.3**: Vacuum drying energy for sol-gel coating.*

Vacuum drying (Distillation)				
Parameter	**Description**	**Value**	**Unit**	**Reference**
E	Electricity	330	Wh/kg solvent	Capello et al. (2005)
m_{steam}	Amount of steam	1.53	kg/kg solvent	-
C_{heat}	Heat content	2800000	J/kg steam	Capello et al. (2005)
m_{solv}	Amount of solvent	0.186*	Kg/ kg *Coated NMC 811*	-

**Total solvent (Methanol+Propanol)*

Using data from Table C1.3 in the distillation equations resulted in the following energy requirement:

$$E_{dist} = 61.5\ Wh/kg\ coated\ NMC\ 811$$
$$Q_{dist} = 7.98 \times 10^5\ J/kg\ coated\ NMC\ 811$$

The distillation energy was complemented with additional energy requirement for the sonication and was calculated as a homogenizing process from Piccinno et al. (2016), using the stirring energy equation as presented in section C1.1.

Table C1.4: *Sonication energy used during the evaporation of solvents.*

Sonication (Stirring)				
Parameter	**Description**	**Value**	**Unit**	**Reference**
N_p	Power number of impeller	2.39	-	Piccinno et al. (2016)
ρ_{mix}	Density for the mix	3380*	kg/m^3	Calculated
N	Rotational speed	48.3	-	Piccinno et al. (2016)
d	Impeller diameter	0.139	m	Piccinno et al. (2016)
t	Time	3600	s	Assumption
η_{stir}	Efficiency of agitator	0.9	-	Piccinno et al. (2016)
$V_{reactor}$	Reactor volume	1	m^3	-
m_{dry}	Dry output	3370	kg	NMC 811

*mean density: $(m_{Lithium\ Methoxide}/m_{total}))$ *$\rho_{Lithium\ methoxide}$+ $(m_{Zirconum}/m_{tota}$*$\rho_{Zirconium}$+$(m_{propanol}/m_{tota}))$ *$\rho_{propanol}$)

Using data from Table C1.4 in the stirring energy equation resulted in the following energy requirement:

$$E_{sonic} = 56100\ J/kg = 15.6\ Wh/kg\ Coated\ NMC\ 811$$

The filtration energy requirement was calculated based on the filtration energy requirement from Piccinno et al. (2016), which only states a range between 1 and 10 kWh per ton of dry material. In this study, the higher estimate of 10 kWh/ton of dry output, or 10 Wh/kg, was chosen due to lack of available information on the process.

The last step is heating, which was calculated and scaled using the formula for heating requirement energy from Piccinno et al. (2016), with symbols as in Table C1.5:

$$E_{heat} = \frac{C_p * m_{mix} * (T_r - T_0) + A * ka/S * (Tr - To) * t}{\eta_{heat}}$$

***Table C1.5**: Final heating of the coating process.*

Heating (Heating)				
Parameter	**Description**	**Value**	**Unit**	**Reference**
C_p	Specific heat capacity of mix	1440	J/kg*K	Morganti et al. (2019)
m_{mix}	Mass of reaction mixture	3060*	kg	-
T_r	Reaction temp	300	°C	Lee et al. (2020)
T_0	Starting temp	25	°C	Assumption
A	Surface area of the reactor	5.90	m^2	Piccinno et al. (2016)
ka	Thermal conductivity of insulation	0.042	W/m*K	Piccinno et al. (2016)
S	Insulation thickness	0.075	m	Piccinno et al. (2016)
t	Drying time	3600	s	Lee et al. (2020)
η_{heat}	Efficiency of heating element	75%	-	Piccinno et al. (2016)
$V_{reactor}$	Reactor volume	1	m^3	-
$\%_{use}$	Reactor usage factor	0.9	-	Piccinno et al. (2016)
ρ_{NMC}	density of NMC	3400**	kg/m^3	MSE Supplies (2022)

*Calculated by: $m_{mix} = \rho_{NMC} * V_{reactor} * \%_{use}$
**Pressed density of NMC 811 cathode

Data from Table C1.5 was used in the heat equation, resulting in the following energy requirement:

$$E_{heat} = 528000\ J/kg = 147\ Wh/kg\ LZO\ coated\ NMC\ 811$$

C1.1.1 Lithium methoxide

To calculate the energy demand for producing lithium methoxide, the energy demand for mixing was calculated with stirring energy equation from Piccinno et al. (2016), shown in Section C1.1.

Table C1.6: *Stirring energy for lithium methoxide.*

Mixing (Stirring energy)				
Parameter	**Description**	**Value**	**Unit**	**Reference**
N_p	Power number of impeller	0.79	-	Piccinno et al. (2016)
ρ_{mix}	Density for the mixture	850	kg/m^3	Albemarle (2018)
N	Rotational speed	1.42	1/s	Piccinno et al. (2016)
D	Impeller diameter	0.373	m	Piccinno et al. (2016)
T	Time	25200**	s	Cao (2008)
η_{stir}	Efficiency of agitator	0.9	-	Piccinno et al. (2016)
V_{React}	Reactor volume	1	m^3	Assumption

*The data from Piccinno et al. (2016) was based on estimations of a reactor tank of 1000 L.
**Assumed time due to slow dripping of lithium in methanol.

The stirring energy requirement was calculated with the input parameters from Table C1.6, resulting in the following energy requirement for the mixing of 1 kg of lithium methoxide output:

$$E_{stir} = 454\ J/kg = 0.126\ Wh/kg$$

C1.3 Catholyte sheet

The manufacturing of the catholyte sheet consist of mixing, dry-filming and distillation, as shown in Appendix A1. The calculations are presented for the output of 1 kg catholyte sheet. First, the mixing energy were approximated with the homogenizing process from Piccinno et al. (2016), calculated as stirring energy as presented in section C1.1.

Table C1.7: *Data for mixing calculated with stirring energy.*

Mixing (Stirring)				
Parameter	**Description**	**Value**	**Unit**	**Reference**
N_p	Power number of impeller	2.39	-	Piccinno et al. (2016)
ρ_{mix}	Density for the mixture	1940*	kg/m^3	Calculated
N	Rotational speed	48.3	1/s	Piccinno et al. (2016)
d	Impeller diameter	0.139	m	Piccinno et al. (2016)
t	Time	3600	s	Assumption
η_{stir}	Efficiency of agitator	0.9	-	Piccinno et al. (2016)
m_{dry}	Dry mass	972	kg	-
V_{React}	Reactor volume	1	m^3	

*Calculated using the material specific density and ratios of the input materials

Data from Table C1.7 was used in the stirring energy equation, resulting in the following energy requirement:

$$E_{stir} = 112000\ J/kg = 31.1\ Wh/kg\ catholyte\ sheet$$

The energy requirement of the dry-filming process was calculated based on tape-casting of thin film solar cells from Celik et al. (2020) with the following formula and symbols as shown in Table C1.8:

$$E_{dryfilm} = \frac{E}{h_{layer} * \rho_{mix} * (1-\%_{solv})}$$

Table C1.8: *Data for dry-filming as calculated using energy for tape-casting.*

Dry-film (Tape-casting)				
Parameter	**Description**	**Value**	**Unit**	**Reference**
E	Enery requirement	30	Wh/m^2	Celik et al. (2020)
h_{layer}	Layer thickness	0.000105	m	Lee et al. (2020)
ρ_{mix}	Density of the mixture	1940*	kg/m^3	Calculation
$\%_{solv}$	Solvent fraction	50	%	Assumption

*Calculated based on material ratio and material densities

Using data from Table C1.8 in the tape-casting equation resulted in the following energy requirement:

$$E_{dryfilm} = 294\ Wh/kg\ catholyte\ sheet$$

Lastly, the evaporation and recirculation of solvents that were calculated by a distillation process presented by Capello et al. (2005), shown in Section C1.2.

Table C1.9: *Data to calculate the energy for Evaporation of solvents*

Distillation				
Parameter	**Description**	**Value**	**Unit**	**Reference**
El	Electricity	330	Wh/kg	Capello et al. (2005)
m_{steam}	Amount of steam	1.53	kg/kg solvent	Capello et al. (2005)
C_{heat}	Heat content	2800000	J/kg	Capello et al. (2005)
m_{solv}	Amount solvent	1	kg/kg catholyte	Assumption

Using data from Table C1.9 in the distillation equations resulted in the following energy requirements:

$$E_{dist} = 330\ Wh/kg\ catholyte\ sheet$$
$$Q_{dist} = 4.28\ MJ/Kg\ catholyte\ sheet$$

C2. Electrolyte sheet

The electrolyte sheet production consists of mixing, doctor blading, heating and distillation as shown in Appendix A2. The energy demand is calculated based on the output of 1 kg of dry electrolyte sheet. First, the mixing of argyrodite powder, binder and solvents was calculated using homogenizing, calculated as stirring energy by Piccinno et al. (2016), shown in Section C1.1.

Table C2.1: *Mixing of the components for the electrolyte sheet.*

Mixing (Stirring)				
Parameter	**Description**	**Value**	**Unit**	**Reference**
N_p	Power number of impeller	2.39	-	Piccinno et al. (2016)

ρ_{mix}	Density for the mixture	1250*	kg/m^3	Lee et al. (2020)
N	Rotational speed	48.3	rpm	Lee et al. (2020)
d	Impeller diameter	0.139	m	Piccinno et al. (2016)
t	Time	360	s	Lee et al. (2020)
η_{stir}	Efficiency of agitator	0.9	-	Piccinno et al. (2016)
$V_{reactor}$	Reactor volume	1	m^3	Piccinno et al. (2016)
m_{dry}	Dry mass	624	kg	Piccinno et al. (2016)

*Calculated based on material ratio and material densities

Data from Table C2.1 used in the stirring energy equation resulted in the following energy requirement per 1 kg of electrolyte sheet:

$$E_{mixing} = 11200\ J/kg = 3.11\ Wh/kg\ electrolyte\ sheet$$

The coating mixture was applied on a PET film using doctor blading. When scaled up, the process was approximated with a tape-casting of thin-film solar cells from Celik et al. (2020), presented in Section C1.3.

***Table C2.2**: Coating of the mixture slurry on a PET film.*

Doctor blading (Tape casting)				
Parameter	**Description**	**Value**	**Unit**	**Reference**
E	Energy requirement	30	Wh/m^2	Celik et al. (2020)
h_{layer}	Layer thickness	0.00004	m	Lee et al. (2020)
ρ_{mix}	Density of the mixture	1250	kg/m^3	Calculated
$\%_{solv}$	Solvent fraction	0.050	kg/m^2	Calculated

Data from table C2.2 was used in the tape-casting equation, resulting in the following energy requirement:

$$E_{dryfilm} = 1200\ Wh/kg\ electrolyte\ sheet$$

The evaporation and recirculation of solvents were calculated by a distillation process presented by Capello et al. (2005), presented in Section C1.2.

***Table C2.3:** Energy for evaporation and recirculation of solvents.*

Heating (Distillation)				
Parameter	**Description**	**Value**	**Unit**	**Reference**
El	Electricity	330	Wh/kg solvent	Capello et al. (2005)
m_{steam}	Amount of steam	1.53	kg/kg solvent	Capello et al. (2005)
C_{heat}	Heat content	2800000	J/kg steam	Capello et al. (2005)
m_{solv}	Amount solvent	1	kg/kg electrolyte sheet	-

Data from Table C2.3 was used in the distillation equations, resulting in the following energy requirement:

$$E_{dist} = 330\ Wh/kg\ electrolyte\ sheet$$
$$Q_{dist} = 4280000\ J/kg\ electrolyte\ sheet$$

C2.1 Electrolyte powder

The process of producing the electrolyte powder includes initial mortar grinding, mixing, centrifugation, drying, annealing and distillation, as shown in Appendix A2.1 The energy demand was calculated based on 1 kg of electrolyte powder as output. The energy requirement of the first step, i.e. mixing in a mortar, was calculated using the grinding energy requirement from Piccinno et al. (2016), specifically the grinding energy equation below with symbols as in Table C2.4. The lower range values were selected due to the assumption that the initial grinding is not overly energy demanding.

$$E_{grind} = E^{*} m_{solids}$$

Table C2.4: *Mortar mixing of the electrolyte powder input materials.*

Mortar mixing (Grinding)				
Parameter	**Description**	**Value**	**Unit**	**Reference**
E_{high}	Upper range	16	Wh/kg	Piccinno et al. (2016)
E_{low}	Lower range	8	Wh/kg	Piccinno et al. (2016)
m_{solids}	Mass of all solid components	0.67*	kg/kg argyrodite	-

*Mass of dry powder excl. solvents

The data from Table C2.4 was used in the grinding energy equation above, calculating the following energy requirement:

$$E_{grind} = 5.36\ Wh/kg\ electrolyte\ powder$$

The energy requirement for mixing the electrolyte powder and solvent was according to Zhou et al. (2018) mixed in two steps. In this calculation, the mixing steps were calculated together, using the stirring energy as presented by Piccinno et al. (2016), shown in Section C1.1.

Table C2.5: *Data for mixing of electrolyte powder and solvents.*

Mixing (Stirring energy)				
Parameter	**Description**	**Value**	**Unit**	**Reference**
N_p	Power number of impeller	0.79	-	Piccinno et al. (2016)
ρ_{mix}	Density for the mixture	1240*	kg/m^3	-
N	Rotational speed	1.42	1/s	Piccinno et al. (2016)
d	Impeller diameter	0.373	m	Piccinno et al. (2016)
t	Time	130000	s	Zhou et al (2018)
η_{stir}	Efficiency of agitator	0.9	-	Piccinno et al. (2016)
m_{dry}	Dry mass	620**	kg	-
$V_{reactor}$	Volume of reactor	1	m^3	-

**Calculated density of the mixture*
***Mass with excluded solvents*

Using data from Table C2.5 in the stirring energy equation resulted in the following energy requirement per 1 kg of electrolyte powder:

$$E_{mixing} = 4670 = 1.30\ Wh/kg\ dry\ electrolyte\ powder$$

The evaporation and recirculation of solvents were calculated using distillation energy as recommended by Capello et al. (2005), presented in Section C1.2.

Table C2.6: *Data for evaporation and recirculation energy.*

Heating (Distillation)				
Parameter	**Description**	**Value**	**Unit**	**Reference**
El	Electricity	330	Wh/kg solvent	Capello et al. (2005)
m_{steam}	Steam amount	1.53	kg/kg solvent	Capello et al. (2005)
C_{heat}	Heat content	2800000	J/kg steam	Capello et al. (2005)
m_{solv}	Amount solvent	1	Kg/kg electrolyte sheet	-

Using data from Table C2.6 in the distillation equations resulted in the following energy requirements:

$$E_{dist} = 330\ Wh/kg\ Electrolyte\ powder$$
$$Q_{dist} = 4.28\ MJ/kg\ Electrolyte\ powder$$

The annealing was calculated based on heating energy as presented by Piccinno et al. (2016), shown in section C1.2.

Table C2.7: *Data for annealing, calculated by heating process.*

Annealing (Heating)				
Parameter	**Description**	**Value**	**Unit**	**Reference**
C_p	Specific heat capacity of mixture	1340*	J/kg·K	Cheng et al. *(2021)*
m_{mix}	Mass of reaction mixture	1480	kg	-
T_r	Reaction temp	550	°C	Zhou et al. (2018)
T_0	Starting temp	25	°C	Assumption
A	Surface area of the reactor	5.90	m^2	Piccinno et al. (2016)
ka	Thermal conductivity of insulation	0.042	W/m*K	Piccinno et al. (2016))
S	Insulation thickness	0.075	m	Piccinno et al. (2016)
t	Drying time	21600	s	Zhou et al 2018
η_{heat}	Efficiency of heating element	75%	-	-
$V_{reactor}$	Reactor volume	1	m^3	Piccinno et al. (2016)
	Reactor usage factor	90%	-	Piccinno et al. (2016)
ρ_{mix}	Density of the mixture	1640**	kg/m^3	-

**Read from figure 3 in Cheng et al. (2021)*
***Assumed same density as argyrodite*

Data from Table C2.7 was used in the heat equation, calculating the following energy requirement:

$$E_{heat} = 973000\ \text{J/kg electrolyte powder}$$

C2.2 Lithium sulfide

The synthesis of lithium sulfide was modeled based on a patent by Chu et al. (2015), where sulfur powder was dried under vacuum for 12 h at 100°C, then mixed with lithium hydride (LiH) powder in a 1:2 molar ratio in argon atmosphere, then in a sealed ball mill tank at 400 r/min for 8 h in room temperature. The resulting mixture was lithium sulfide without impurities. The energy required for the production process was modeled using Piccinno et al. (2016) calculations for drying and grinding.

The mixing process of sulfur powder with LiH was assumed with a grinding process as recommended from Piccinno et al. (2016). The energy requirements for grinding were between 8-16 kWh/ton, where 16 kWh/ton were recommended if data were lacking. Therefore, 16 kWh/ton dry product was used.

The drying process was approximated with the heating process from Piccinno et al. (2016), presented in Section C1.2.

***Table C2.8**: Energy data for drying of sulfur powder.*

Drying (heating)				
Parameter	**Description**	**Value**	**Unit**	**Reference**
C_p	Specific heat capacity of solid sulfur	741*	W/kg·K	Nehb and Vydra (2006)
ρ_{Sulfur}	Sulfur density	2070	kg/m^3	Nehb and Vydra (2006)
-	Molar mass sulfur	0.0321	kg/mol	Nehb and Vydra (2006)
m_{mix}	Mass of reaction mixture	1860**	kg	Piccinno et al. (2016)
T_r	Reaction temperature	100	-	Chu et al. (2015)
T_0	Starting temperature	25***	°C	Assumption
A	Surface area of the reactor	5.90	m^2	Piccinno et al. (2016)
ka	Thermal conductivity of insulation	0.042	W/m*K	Piccinno et al. (2016)
S	Insulation thickness	0.075	m	Piccinno et al. (2016)
t	Heated time	43200	s	Chu et al. (2015)
η_{heat}	Efficiency of heating element	75	%	Piccinno et al. (2016)
$V_{reactor}$	Reactor volume	1	m^3	-
ρ_{mix}	Mean density of mixture	2070	kg/m^3	-

*Cp = 14.989 + 0.0261 * (298 K + (100-25)/2))/(0.032065 mol/kg)
**90% of the capacity of the reactor volume. (2070 kg/m^3 *0.9)
***Assumed starting temperature to be room temperature

Data from Table C2.8 was used in the heat equation, resulting in the following energy requirement per kg of lithium sulfide:

$$E_{heat} = 81700\ J/kg$$

C2.2.1 Lithium hydride

Lithium hydride is formed by a reaction between lithium and hydrogen gas (Sato and Takeda, 2013). The reaction is heated and assumed to be self-sustaining as the reaction is exothermic. The heating energy required was calculated using Piccinno et al. (2016) energy calculations to reach reaction temperature, using the formula below with symbols as in Table C2.9:

$$E_{heat} = \frac{C_p * m_{mix} * (T_r - T_0)}{\eta_{heat}}$$

Table C2.9: *Data för lithium hydride reaction.*

Heating (heating)				
Parameter	**Description**	**Value**	**Unit**	**Reference**
C_p	specific heat capacity lithium	3550	J/kg*K	(Kamienski et al., 2004)
m_{mix}	Mixture mass	1		-
T_r	Reaction temperature	700	°C	Sato and Takeda, 2013)
T_0	starting temperature	25*	°C	-
η_{heat}	Heating efficiency	0.75	-	-

*Assumed starting temperature to be room temperature

The calculation was based on values for lithium only, as the mass of hydrogen gas compared to lithium is low and can therefore according to Piccinno et al. (2016) be neglected from the calculations. The values in Table C2.9 was used in the reaction heating equation to calculate the energy demand per kg of lithium hydride:

$$E_{heat} = 3200000\ J/kg\ LiH = 888\ Wh/kg\ LiH$$

C2.3 Phosphorus pentasulfide

The energy required to produce phosphorus pentasulfide was calculated based on a mixture of phosphorus and sulfide heated in the reaction temperature span as presented by Bettermann et al. (2000). The process was modeled using reaction heating energy as presented by Piccinno et al. (2016), shown in Section C2.2.1.

Table C2.10: *Data for the reaction to create phosphorus pentasulfide.*

Heating (Heating)				
Parameter	**Description**	**Value**	**Unit**	**Reference**
$C_{p,liq}$	specific heat capacity	727*	J/kg*K	-
m_{liq}	Mixture mass	1	kg	-
T_r	Reaction temperature	350	°C	Bettermann et al. (2000)
T0	starting temperature	25**	°C	-
η_{heat}	Heating efficiency	0.75	-	-

* $(C_{p\text{-Phosphourus}}\ (770\ J/kg*K) * m_{Phosphorus} + C_{p\text{-Sulfur}}\ (710\ J/kg*K) * m_{Sulfur}) / (m_{Phosphorus} + m_{Sulfur})$
**Assumed room temperature

The energy required was calculated with data from Table C2.10 in the reaction heating to obtain 1 kg of phosphorus pentasulfide:

$$E_{heat} = 315000\ J/\ Kg = 87.5\ Wh/kg\ phosphorus\ pentasulfide$$

C2.4 Electrolyte sheet production

The electrolyte sheet is manufactured in three main steps: mixing, doctor blading and drying. These steps were scaled and calculated using the framework by Piccinno et al. (2016). The energy requirement of all processes were calculated based on the output of 1 kg dry electrolyte sheet. The mixing energy has been modeled using a

homogenizing process, as recommended by Piccinno et al. (2016), represented by stirring energy as presented in Section C1.1.

Table: C2.11: *Data for the first production step, mixing of the input materials.*

Mixing (Stirring)				
Parameter	**Description**	**Value**	**Unit**	**Reference**
N_p	Power number of impeller	2.39*		Piccinno et al. (2016)
ρ_{mix}	Density for the mixture	1250**	kg/m^3	Lee et al. (2020)
N	Rotational speed	48.3	1/s	Piccinno et al. (2016)
d	Impeller diameter	0.139*	m	Piccinno et al. (2016)
t	Time	360	s	Lee et al. (2020)
η_{stir}	Efficiency of agitator	0.9*		Piccinno et al. (2016)
V_{react}	Reactor volume	1	m^3	Assumed from Piccinno et al. (2016)

*Assumed 1000 L reactor
**Calculated density of the mixture (%argyrodite*ρ_{LPSCL}+(1-%argyrodite)*(0.5* $\rho_{solvent1}$+0,5*$\rho_{solvent2}$))*1000

Data from Table C2.11 was used in the stirring energy equation to calculate the energy requirement:

$$E_{stir} = 11200\ J/kg = 3.11\ Wh/kg\ electrolyte\ sheet$$

The doctor blading process was not represented in the framework by Piccinno et al. (2016) and was therefore calculated using an article by Celik et al. (2020), which presents values for doctor blading for electricity demand per square meter of thin-film solar cells. The energy requirement was calculated with the following formula with symbols as in Table C2.12:

$$E_{doctorblade} = \frac{E\ /\ h_{layer} * \rho_{mix}}{Share\ argyrodite}$$

Table C2.12: *Data for the second process, doctor blading on the PET film.*

Doctor blading (Tape casting)				
Parameter	**Description**	**Value**	**Unit**	**Reference**
E	Energy requirement	30	Wh/m^2	Celik et al. (2020)
h_{layer}	Layer thickness	0.00004	m	Lee et al. (2020)
ρ_{mix}	Mix density	1250*	kg/m^3	Calculated
	Layer density (wet)	0.0499	kg/m^2	Calculated

*Calculated mixture density as in table C2.11

Data from table C2.12 was used in the doctor blading equation above, resulting in the following energy requirement:

$$E_{doctorblade} = 1\ 200\ Wh/kg\ electrolyte\ sheet$$

The last step, drying, was calculated using the process of heating from Piccinno et al. (2016), presented in section C1.2.

Table C2.13: *Data for heating the final product.*

Overnight drying (Heating)				
Parameter	**Description**	**Value**	**Unit**	**Reference**
C_p	Specific heat capacity of mixture	1600 *	J/kg·K	Cheng et al. (2021)
m_{mix}	Mass of reaction mixture	1120**	kg	Calculated
T_r	Reaction temperature	40	°C	Lee et al. (2020)
T_0	Starting temperature	25	°C	Assumption
A	Surface area of the reactor	5.90***	m^2	Piccinno et al. (2016)
k_a	Thermal conductivity of insulation	0.042***	W/m*K	Piccinno et al. (2016)
S	Insulation thickness	0.075***	m	Piccinno et al. (2016)
t	Drying time	43200	s	Lee et al. (2020)
η_{heat}	Efficiency of heating element	75%***		Piccinno et al. (2016)
ρ_{mix}	Mean mixture density	1250****	kg/m^3	Calculation
	Share of argyrodite	50%		-

*Calculated for the mixture. (2000000 J/m^3*K /ρ_{mix})
**Assumed 90% filling of the reactor
***Assumed 1000 l reactor
**** Calculated density of mixture. See table C2.11.

Using data from Table C2.13 in the heat equation, resulted in the following energy requirement:

$$E_{heat} = 69100\ J/kg = 19.2\ Wh/kg\ electrolyte\ sheet$$

C3. Ag-C separator layer

The Ag-C separator layer is produced in three main processes: mixing screen printing, and drying. The energy calculations were based on the output of 1 kg Ag-C separator layer. The mixing was scaled up and calculated based on homogenizing from Piccinno et al. (2016), calculated with stirring energy as presented in Section C1.1.

Table C3.1: *Data for the initial mixing of input materials.*

Mixing (Stirring)				
Parameter	**Description**	**Value**	**Unit**	**Reference**
N_p	Power number of impeller	2.39	-	Piccinno et al. (2016)
ρ_{mix}	Density for the mixture	3810*	kg/m^3	Calculation
N	Rotational speed	48.3	1/s	Piccinno et al. (2016)
d	Impeller diameter	0.139	m	Piccinno et al. (2016)
t	Time	3600**	s	-
η stir	Efficiency of agitator	0.9	-	Piccinno et al. (2016)
$V_{reactor}$	Volume of reactor	1	m^3	Assumed from Piccinno et al. (2016)
m_{dry}	Dry mass	3690***	kg	-

*Calculated based on input ratios and material densities
**Assumed reaction time
***Mass without solvent

Using data from Table C3.2 in the stirring energy equation resulted in the following energy requirement:

$$E_{mix} = 57800\ J/kg\ dry\ sheet = 16.1\ Wh/kg\ Ag\text{-}C\ separator\ layer$$

The screen-printing was calculated using TiO_2 layer deposition on perovskite modules described by Moni (2020) as a proxy, using the following formula with symbols as in Table C3.2:

$$E_{Printing} = \frac{E}{\varrho_{mix} * h} * share\ of\ solids$$

Table C3.2: *Data input for the screen-printing process.*

Screen printing (Screen printing)				
Parameter	**Description**	**Value**	**Unit**	**Reference**
E	Screen printing electricity	15700	J/m^2	Moni (2020)
h	Component thickness	0.00001	m	Lee et al. (2020)
ρ_{mix}	Mixture density	3810 *	kg/m^3	-
-	Share of solids	88.3	%	-

*Calculated based on material ratio and material densities

Using data from Table C3.2 in the screen-printing equation above resulted in the following energy requirement:

$$E_{Printing} = 467000\ J/kg = 129\ Wh/kg\ Ag\text{-}C\ separator\ layer$$

The evaporation and recirculation of solvents were calculated using distillation energy as recommended by Capello et al. (2005), presented in Section C1.2.

Table C3.3: *Data input for calculating the evaporating the solvents.*

Heating (distillation)				
Parameter	**Description**	**Value**	**Unit**	**Reference**
E	Electricity	330	Wh/kg	Capello et al. (2005)
m_{steam}	Steam amount	1.53	kg/kg solvent	Capello et al. (2005)
C_{heat}	Heat content	2800000	kJ/kg	Capello et al. (2005)
m_{solv}	Amount solvent	0.0399	kg/kg Ag-C	Calculation

The data from table C3.3 were used in the distillation equations, resulting in the following energy requirement:

$$E_{dist} = 13.2\ Wh/kg\ Ag\text{-}C\ separator\ layer$$
$$Q_{dist} = 171000\ J/kg\ Ag\text{-}C\ separator\ layer$$

C4. Pouch cell assembly

Details not disclosed due to confidentiality of the raw data from Chordia et al. (2021), which was used in the calculations of the energy requirement for pouch cell assembly in this study.

C5. Dry room energy

The energy for the dry rooms was approximated with data from the dry-room modeling conducted by Deng et al. (2017) combined with some assumptions on the future factory producing our battery cells. For their scale-up, Deng et al. (2017) models a dry room that covers 4000 m^2 and can maintain 21°C at 100 ppm moisture content (corresponds to a dewpoint of about -42°C).

In this study, the energy was scaled to the output of one unit process factory construction and operation (see Appendix A7), specifically 1 year of factory operations. To derive the annual energy requirement, an assumption was made on the operation time of the dry rooms. A value of 7900 hours was chosen, which corresponds to 24/7 production minus some maintenance. The same value was used for the giga-scale factory in Chordia et al (2021). A summary of the values used are given in the Table C5.1, followed by the energy requirement equation and a description on allocation between energy types.

Table C5.1: *Data parameters for dry room energy calculation.*

Dry room				
Parameter	**Description**	**Value**	**Unit**	**Reference**
W	Power demand	0.51	kW/m^2	Deng et al. (2017)
A	Factory area	150 000	m2	Assumption
f_s	Share of factory covered with dry room	75	%	Assumption
t	Annual run time	7 900	h	Assumption (similar to Chordia et al. 2021)

The formula as presented by Deng et al. (2017) to calculate the annual dry room energy was:

$$Annual\ dry\ room\ energy = W * A * f_s * t$$

Using data from Table C5.1 in the dry room energy equation above resulted in about 453 GWh. The exact energy values would, however, shift greatly depending on the temperature and humidity outside the factory. Deng et al. (2017) unfortunately do not separate the energy values into energy from electricity, heating or cooling. Based loosely on the dry-room schematics from Deng et al (2017) and the unpublished data from Chordia et al. (2021), a simplified approximation was made that heating, cooling and electricity use on third of the total energy each, i.e. about 151 GWh or 544 000 GJ.

DEPARTMENT OF TECHNOLOGY MANAGEMENT AND ECONOMICS
DIVISION OF ENVIRONMENTAL SYSTEM ANALYSIS
CHALMERS UNIVERSITY OF TECHNOLOGY
Gothenburg, Sweden
www.chalmers.se

CHALMERS
UNIVERSITY OF TECHNOLOGY